7-2021

Geological Structures and Crustal Architecture of the Cascadia Subduction Zone from the Integration of Multiple Geophysical Datasets

Asif Ashraf
University of Nebraska-Lincoln, asif@huskers.unl.edu

GEOLOGICAL STRUCTURES AND CRUSTAL ARCHITECTURE OF THE CASCADIA SUBDUCTION ZONE FROM THE INTEGRATION OF MULTIPLE GEOPHYSICAL DATASETS

By

Asif Ashraf

A THESIS

Presented to the faculty of

The Graduate College at the University of Nebraska

In Partial Fulfillment of Requirements

For the Degree of Master of Science

Major: Earth and Atmospheric Sciences

Under the Supervision of Professor Irina Filina

Lincoln, Nebraska

July, 2021

Geological structures and crustal architecture of the Cascadia Subduction zone from the integration of multiple geophysical datasets

Asif Ashraf, M.S.

University of Nebraska, 2021

Advisor: Irina Filina

The Cascadia subduction zone (CSZ) has a high potential for an inevitable and devastating megathrust earthquake. This margin is characterized by a complex seismicity pattern. Particularly in Oregon, there is a seismically quiescent zone bounded by high seismicity regions to the north and south. To comprehend these variations in seismicity, it is important to study the differences in crustal architectures and physical properties (densities and magnetic susceptibilities) along the CSZ. The primary objectives are to develop two plate-scale 2D integrated models through different seismicity zones and to map major tectonic structures from filtered potential fields.

The Juan de Fuca oceanic crust requires a number of lower density zones with respect to adjacent oceanic crust to fit gravity data. These zones correlate to previously identified propagator wakes that are formed during spreading ridge propagation and mapped from disturbances of seafloor magnetic stripes. However, this correlation disagrees with a previous study that relates propagator wakes to denser oceanic crust. To resolve this contention, two gravity models have been developed along the same modeling lines of the previous study which show propagator wakes correlate with lower density zones.

Newly mapped tectonic features termed pseudofault lineaments were traced from filtered magnetic data. These structures appear to be triggered by offsets between spreading ridge segments; they correspond to modeled lower density zones. Seamounts mapped from filtered gravity data appear to be clustered around identified pseudofault lineaments and propagator wakes, suggesting that those act as conduits for magma. This indicates that pseudofault lineaments and propagator wakes represent zones of weakened oceanic crust. Because of the oblique subduction, most of these identified features are subducting beneath Washington, resulting in greater seismicity. Furthermore, the pattern of earthquakes within the Wadati-Benioff zone is aligned with interpreted zones of crustal weakness.

Table of Contents

List of Figures iv

List of Tables vii

CHAPTER 1. Introduction 1

1.1 Study area 1

1.2 Motivation for the study 1

1.3 Objectives of this study 3

CHAPTER 2. Geological Background 7

2.1 Oceanic domain 7

2.1.1 Juan de Fuca plate 7

2.1.2 Seamounts 9

2.1.3 Propagator wakes 9

2.1.3.1 Propagating rift theory 9

2.1.3.2 Propagating wakes in other regions 18

2.1.3.3 Internal architecture and physical properties of propagator wakes within the Juan de Fuca plate 21

2.2 Continental domain 24

2.2.1 Siletz Terrane 24

2.2.2 Willamette basin 25

CHAPTER 3. Geophysical Data 26

3.1 Topography and bathymetry 26

3.2 Gravity anomaly 26

3.3 Magnetic anomaly 29

3.4 Seismic data 31

3.5 Earthquake data 40

CHAPTER 4. Methodology 41

4.1 2D integrated modeling 41

4.2 Integrated spatial analysis 46

4.3 Earthquake analysis 49

4.3.1 Selection of the Wadati-Benioff earthquakes 49

4.3.2 Least square analysis in seismicity clusters 50

CHAPTER 5. Results 53

5.1 2D integrated modeling 53

5.1.1 Physical properties of modeled geological blocks 53

5.1.2 Crustal architecture in Washington model 60

5.1.3 Crustal architecture in Oregon model 61

5.1.4 Forward gravity modeling of propagator wake zones 62

5.2 Integrated spatial analysis 71

5.2.1 Mapping of pseudofault lineaments 71

5.2.2 Correlation of mapped lineaments and low-density crustal zones 80

5.2.3 Mapping of seamounts 86

CHAPTER 6. Discussions 89

6.1 Comparison between plate-scale models 89

6.2 Association of propagator wakes with lower density crustal zones 98

6.3 Assessing the correlation between pseudofault lineaments and seamounts 102

6.4 Possible effects of identified tectonic structures on subduction mechanism 110

CHAPTER 7. Conclusions 116

References 119

Appendix-A 132

List of Figures

Figure 1.1 6

Figure 2.1 11

Figure 2.2 15

Figure 2.3 18

Figure 2.4 19

Figure 2.5 20

Figure 2.6 23

Figure 3.1 28

Figure 3.2 30

Figure 3.3 34

Figure 3.4 37

Figure 3.5 39

Figure 4.1 41

Figure 4.2 43

Figure 4.3 48

Figure 4.3 50

Figure 4.4 51

Figure 4.5 52

Figure 5.1 58

Figure 5.2 59

Figure 5.3 67

Figure 5.4 69

Figure 5.5 70

Figure 5.6 75

Figure 5.7 77

Figure 5.8 79

Figure 5.9 86

Figure 5.10 88

Figure 5.11 88

Figure 5.12 89

Figure 6.1 90

Figure 6.2 97

Figure 6.3 98

Figure 6.4 103

Figure 6.5 104

Figure 6.6 106

Figure 6.7 110

Figure 6.8 111

Figure 6.9 112

Figure 6.10 115

List of Tables

Table 4.1 45

Table 4.2 46

Table 5.1 53

Table 6.1 94

Table 6.2 96

Table 6.3 108

Table 6.4 110

Chapter 1: Introduction

1.1 Study area

This study is focused on the Cascadia Subduction Zone (CSZ) which is situated along the west coast of North America and Northeast of the Pacific ocean (Fig. 1.1). This zone extends from northern California in the south (~40°N) to British Columbia in the north (~51°N). The CSZ is comprised of three oceanic microplates, namely Juan de Fuca (JdF), Gorda, and Explorer plates. In terms of the continental area coverage, this study primarily includes Washington and Oregon states where most of the oceanic JdF plate subducts beneath the continental part of the North American plate.

1.2 Motivation for the study

The CSZ is a region prone to high seismic hazards which are associated with ongoing subduction (Heaton and Hartzell, 1987; Miller et al., 2002; Bilek and Lay, 2018). A devastating megathrust earthquake is expected to occur in this subduction zone (Wang and Tréhu, 2016) that will affect millions of people living along the western coastline of the USA and Canada. The last megathrust earthquake with a magnitude close to 9 occurred in this region in the year 1700 (Atwater et al., 1995; Satake et al., 1996; Clague, 1997) that was documented in several Native American stories (Ludwin et al., 2005) and Japanese records (Atwater, 2005). In Japan, an Orphan tsunami was observed as a by-product of this devastating megathrust earthquake. According to Atwater (1987), at least six megathrust earthquakes occurred in the past 7000 years. A typical megathrust

earthquake is capable of developing a severe rupture in the crust and can cause significant damage along the coastal regions (Bilek and Lay, 2018; Rotten et al., 2019).

Sedimentological evidence and buried soil records (Goldfinger et al., 2012) suggest around 500 years recurrence interval between past megathrust earthquakes (Atwater and Hemphill-haley, 1996; Witter et al., 2012; Goldfinger et al., 2017). However, as there is a possibility that buried soil records being incomplete (Atwater et al., 1996), the recurrence interval period for a catastrophic megathrust earthquake could be less than the estimated 500 years, making the CSZ a region of scientific interest.

Despite several hundred-year-long gaps between great earthquakes, routinely recorded smaller events along the margin reveal an intricate seismicity pattern along the margin (Fig. 1.1). While there are many earthquakes recorded in the northern part of the margin (Washington), in the south, over Oregon state, there is a significant decrease in seismicity (Fig. 1.1), which is atypical for other subduction zones in the world (Kopp, 2013). Therefore, this study is motivated by the imminent threat of a devasting earthquake in this region and a need to understand the unique seismicity zonation.

The overarching goal of the study is to understand the relationship between different tectonic features of the JdF plate and their influence on the ongoing subduction. There are two known types of tectonic structures on the JdF plate - propagator wakes and seamounts. Propagator wakes are V-shaped zones that show disturbances in the magnetic signatures of the rocks. They are initiated at the mid-ocean spreading center due to the reorganization of the ridge segments (see more details in Chapter 2).

Seamounts are underwater volcanic features that can be exposed above the sea bottom (evident in bathymetry as in Fig.1.1) or buried under the sedimentary section (seismic images described in section 3.4 are required to document those). Both propagator wakes and seamounts on the JdF plate represent local inhomogeneities in the subducting oceanic crust, thus they may impact the subduction process and influence seismicity pattern. For example, Trehu et al. (2012) proposed that the protruding part of a seamount may lock the ongoing subduction, resulting in the lack of seismicity observed in the Oregon part of the margin. In the continental domain, the structural and compositional variations in the Siletz terrane (Fig. 1.1) may also affect the observed seismicity pattern. Therefore, it is important to comprehend the tectonic features along the entire extent of the CSZ, the relationships between them, and their influence on the subduction process. To achieve this, two major objectives outlined below were set for this thesis. To help with the objectives, a literature review of the study area was performed (summarized in Chapter 2) and available public geophysical data, namely gravity, magnetic and seismic, were gathered (described in Chapter 3).

1.3 Objectives of this study

Objective 1: Develop two 2-dimensional models crossing different seismicity zones to study how geological structures and physical properties of subsurface rocks vary throughout the CSZ. The methodology for this 2D modeling is provided in Chapter 4. The models integrate public gravity, magnetic and seismic datasets to investigate various

tectonic features along the margin. In this 2D modeling, potential fields allow deriving the density and magnetic susceptibility of subsurface rocks, while seismic reflection and refraction data provide a framework for the subsurface architecture. By combining multiple geophysical datasets, more robust and confident geological models were developed. The plate-scale 2D integrated models span from the JdF spreading center to the Cascadia Arc in the continental domain (shown as orange lines in Fig. 1.1). The northern model crosses the region of high seismicity in Washington. In contrast, the southern model ends in a low seismicity zone in Central Oregon. In this study, those geophysical models are referred to as the Washington and Oregon models respectively. In addition, two additional gravity models were developed to test the previously proposed density distribution over the propagator wakes from Marjanović et al. (2011); these are shown as blue lines in Fig.1.1. According to their findings, propagator wakes are associated with a thinner and denser crust with respect to the surrounding oceanic crust. The analysis presented here concludes an opposite density distribution. Section 5.1.4 describes the details of these models, while Chapter 6 outlines the main shortcomings of the previous study, and lists the arguments toward the newly-established density distribution over the propagator wakes.

Objective 2: Map the key tectonic structures identified from Objective 1 along the 2D models throughout the entire JdF plate via spatial analysis of potential fields. This includes filtering of both gravity and magnetic grids, followed by the lineaments mapping that are then cross-referenced with available seismic reflection data. This allows tracing these structures outside of 2D models (see section 5.2 for details).

Correlation between the derived physical properties from the 2D integrated models and the mapped tectonic elements provides important insight into the character of the subducting part of the JdF plate. To understand the relationship between different tectonic features of the JdF plate, spatial correlation should be assessed via statistical analysis. To evaluate the influence of the interpreted tectonic structures on the subduction process, their alignment with the observed seismicity trends with the subducting slab is also examined in this study.

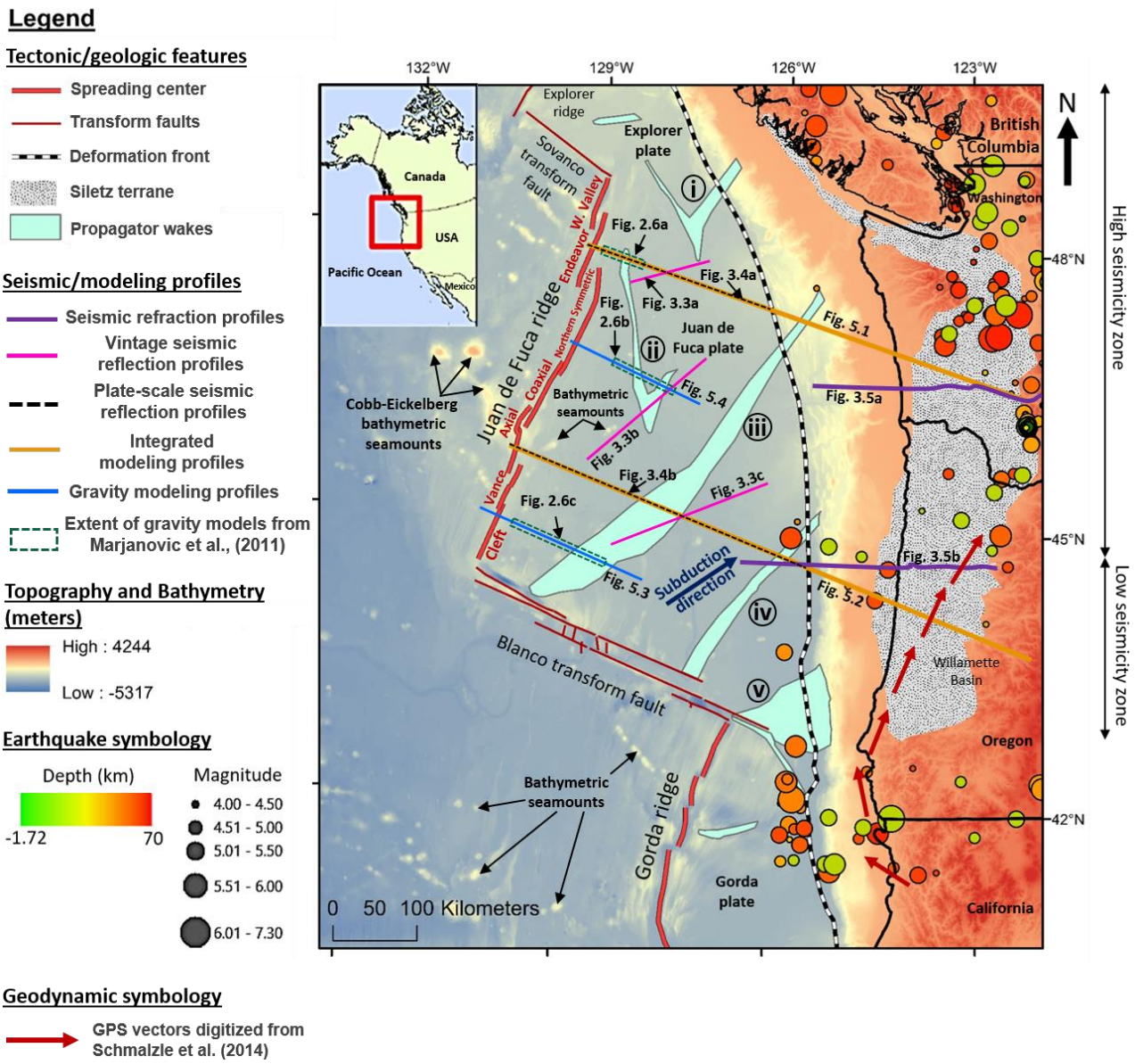

Figure 1.1: Map of the Cascadia Subduction Zone along with its tectonic elements. The 2D integrated and gravity modeling profiles of this study are shown in this map (orange and blue lines). Also, it has several public seismic profiles that are utilized in this research. The subduction direction of the JdF plate is shown with a dark blue arrow. Seismicity on the continental domain is represented by circles scattered from British Columbia in the north to Northern California in the south. The size of the circles indicates earthquake magnitudes, their color represents the focal depths. Several bathymetric seamounts are also pointed out in this map. These seamounts are more apparent on the Pacific plate, however, some are also evident on the JdF plate. Propagator wakes are numbered with roman numerals. The GPS measurements on the southern CSZ are also added to illustrate the rotational movement of a segment of the North American crustal block.

Chapter 2: Geological Background

2.1 Oceanic domain

Three oceanic microplates in Fig 1.1 (the Explorer, Juan de Fuca and Gorda plates) are remnants of the oceanic Farallon plate, although they exhibit different geodynamic characteristics (Trehu et al., 1994; Parsons et al., 1998; DeMets et al., 2010). The JdF plate has a current subduction rate of approximately 40 mm/yr in a mean direction of N68°E (DeMets et al., 1990). With the oblique subduction of the Juan de Fuca plate relative to North American margin (Wells, 1998), this region has developed one of the most complex and seismogenic convergent margins in the world. Even though the Gorda plate is subducting in an eastward direction, the rotational movement of part of the western North American crustal block in Southern Oregon and Northern California (DeMets et al., 1990, 2010; Han et al., 2017) has a profound impact on the overall stress condition of the Gorda block (Fig. 1.1).

The western edge of the accreted sedimentary prism on the ocean floor is referred to as the deformation front (Fig. 1.1). In northern California and Oregon, it is oriented in the N-S direction, while it changes to NNW-SSE in the offshore regions of northern Washington and Vancouver Island, where the accretionary prism is much wider.

2.1.1 Juan de Fuca plate

The JdF plate is the largest one of three subducting oceanic micro-plates that are forming the CSZ and is responsible for observed earthquakes in Washington and most of Oregon. The 480 km long JdF ridge (JdFR) is situated between the Blanco transform fault

zone in the south and Sovanco transform fault zone in the north (Fig. 1.1). The overall orientation of this spreading center is NE-SW. It has an intermediate spreading rate (Wilson, 1993). The JdFR is divided into seven major sections. Starting from the south they are Cleft, Vance, Axial, Coaxial, Northern Symmetric, Endeavor, and West Valley (Fig 1.1). The length of these individual spreading segments varies from 50 to 100 km. The lateral offset between them can reach 30 km (Carbotte et al., 2008). The developed southern model (i.e., Oregon model) and the northern model (i.e., Washington model) of this paper start from the Axial segment and the Endeavor segment of JdFR respectively. The Axial section of the JdF ridge is underlain by the Cobb hotspot (Chadwick et al., 2005). It was the recent (~0.5 Ma) motion of JdFR over the Cobb hotspot that resulted in the formation of the Axial seamount (Karsten and Delaney, 1989).

The first density distribution for the JdF oceanic plate was shown in Romanyuk et al. (1998). However, their distribution is questionable since some regions of the oceanic crust have density values higher than the underlying mantle which is not a likely geological scenario for this particular region. In addition, those models did not have any seismic constraints. Blakely et al. (2005) also developed a gravity model across Oregon which is more reliable because it uses more geologically valid densities for major tectonic elements. However, Blakely et al. (2005) have assigned a single density value for each tectonic element, such as oceanic crust or accretionary prism. For example, the entire JdF oceanic crust has a single density value of 2.85 g/cc, although the oceanic

crustal density should gradually increase as the crust moves away from the spreading center toward the subduction zone (Carlson and Herrick, 1990).

2.1.2 Seamounts

Seamounts are prominent tectonic features of the JdF plate that occur both in the form of isolated edifices and chains. Although more bathymetric seamounts (i.e., those that are exposed at the ocean bottom) are evident on the Pacific plate, quite a few seamounts can also be observed in the JdF plate (Fig. 1.1). The Cobb-Eickelberg volcanoes on the Pacific plate (Fig. 1.1) are an example of chain seamounts that originated at the JdFR from the Cobb hotspot (Desonie and Duncan, 1990). The most recent feature developed over the Cobb hotspot is the Axial seamount (Fig. 1.1) which is volcanically active today (Johnson and Embley, 1990, Chadwick, 2005). As a seamount moves away from the magmatic source, it subsides, gets covered by sediments and is no longer exposed in the bathymetry. To map these buried seamounts, seismic reflection data are traditionally used (more details will be discussed in Chapter 4).

2.1.3 Propagator wakes

Propagator wakes are the other important tectonic features on the JdF plate (blue polygons in Fig.1.1). They are mapped through the offsets in seafloor magnetic stripes (Fig 2.1). In the literature, the terms 'propagator wakes' and 'pseudofaults' are used interchangeably for these structures (Hey, 1977; Wilson et al., 1984; Wilson, 1988, 1993). However, to avoid confusion with the other interpreted features in this study, these structures are only referred to as 'propagator wakes' in this thesis.

2.1.3.1 Propagating rift theory

Magnetic stripes of normal and reverse polarity are an integral part of the oceanic crusts all over the world (Müller et al., 2008). The Juan de Fuca oceanic plate is no exception in this regard (Fig 2.1). However, the notable difference for the JdF plate is that the magnetic stripes representing a certain magnetic chron have offsets between them (Fig. 2.1) that are not related to established transform faults.

Wilson et al. (1984) first suggested that the tectonic evolution of the JdF ridge relates to the propagation of the individual ridge segments. Since ~ 18 million years ago, a total of nine propagation sequences are documented in this region (Johnson et al., 1983; Wilson et al., 1984; Karsten and Delaney, 1989; Wilson, 2002) that are in agreement with the large scale magnetic isochrons (Mason, 1958; Mason & Raff, 1961; Raff & Mason 1961). Blue polygons in Figs. 1.1 and 2.1 represent propagator wakes interpreted by Wilson (2002) from offsets in magnetic anomalies; this interpretation is adopted in this study.

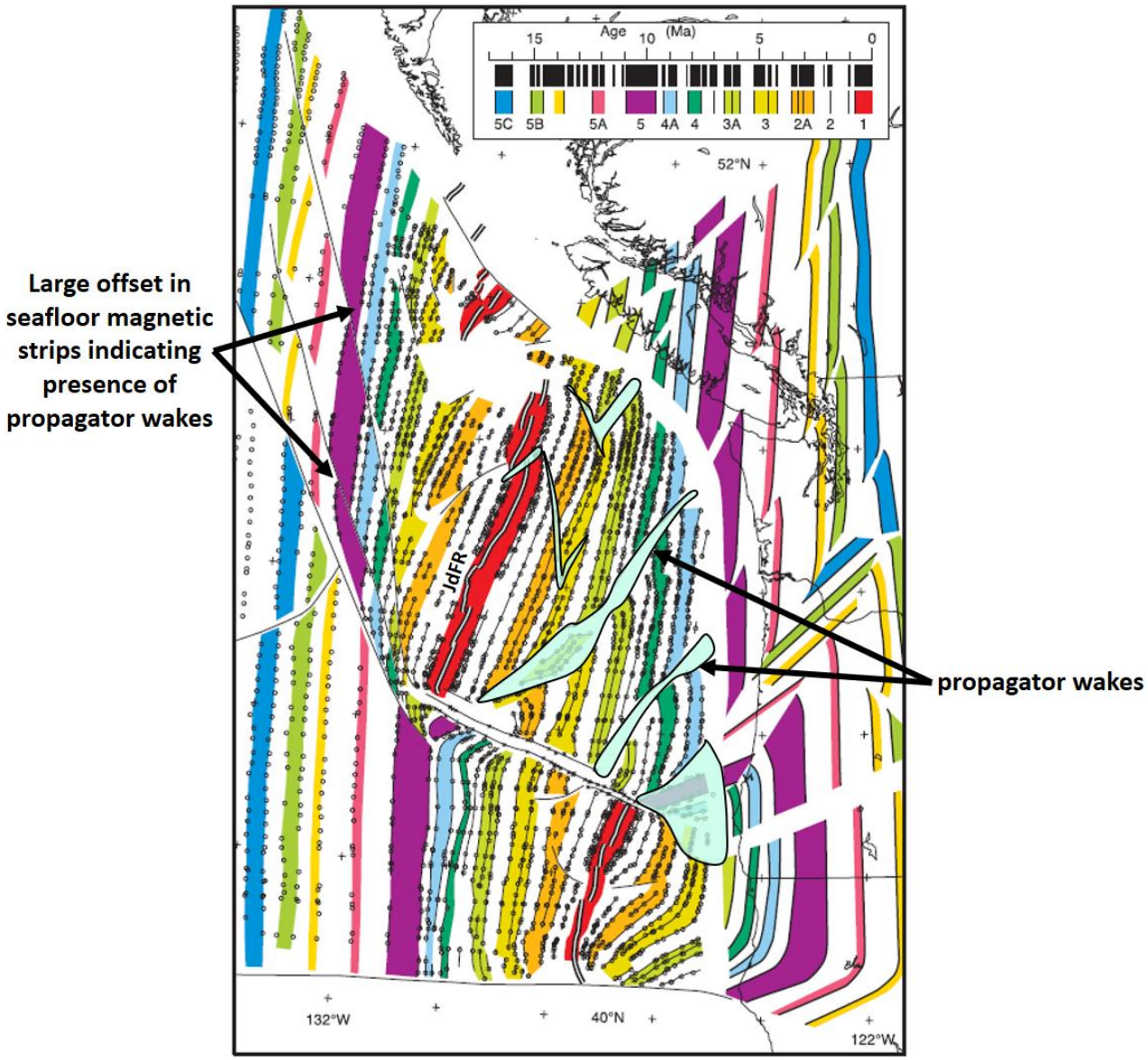

Figure 2.1: Map of seafloor age from Wilson (2002) with overlain propagator wakes shown as light green polygons (to be compared to Fig. 1.1). Seafloor ages are interpreted from magnetic isochrons. The locations of these propagator wakes were digitized from Wilson (2002).

Offsets between oceanic magnetic strips on the JdF plate are known from the marine geophysical survey off the Northwest coast of the U.S.A. (Mason, 1958; Mason & Raff, 1961; Raff & Mason 1961). The offsets found in the vintage magnetic surveys (Mason, 1958; Mason & Raff, 1961; Raff & Mason 1961) have been previously explained as faults

in the oceanic crust related to either plate non-rigidity or relative motions of several microplates (Vine, 1968; Silver, 1971, Elvers et al., 1973). However, these studies were not able to explain similar magnetic anomaly offsets of the Pacific plates, which often resemble the mirror-image pairs of the magnetic anomaly offsets observed on the Juan de Fuca plate.

Hey (1977) put forward the propagating rift model that explained the offset anomaly pattern without breaking the plate rigidity theory and also without the need to apply small microplates in the JdF crust. In brief, the proposed propagating rift model involves the lengthening of one spreading ridge at the expense of its neighboring spreading segment (Fig. 2.2a). This hypothesis relates the magnetic offsets to the structural and tectonic consequences of propagation of spreading centers (Fig. 2.2b). This propagation can be either in the form of sequential jumps (as is shown in the leftmost diagram in Fig. 2.2b) or continuous propagation (middle and rightmost diagrams in Fig. 2.2b). The transform fault, acting as an offset between propagating and retreating spreading centers, also migrates along the strike of propagating ridge. To understand this concept in simpler terms, we can consider one spreading center is propagating in a certain direction while the other spreading center is retreating in the same direction as is shown in Fig. 2.2. After each sequential or continuous jump, the old or the retreating spreading center—that is now extinct—becomes inactive alongside the old transform fault. As a result, the transform fault migrates further along the axis of the spreading center (Fig. 2.2). Theoretically, this migration distance of the transform fault is equal to the length of the old spreading ridge segment that has just become extinct. In this repetitive and

continuous process, the old spreading center dies out at the expense of the growth of the new spreading center. On the oceanic crust, propagator wakes are developed because of this overall oblique migration to the ridge axis. Since the fossil transform faults and fossil spreading centers are consistently added in an en-echelon manner, the propagator wakes represent the fracture zones within the oceanic crust.

In map view, the entire propagator wake resembles the letter 'V' (Fig. 2.2). The convergence of the two parts of the propagator wakes forming the 'V' indicates the direction of the ridge migration. By measuring the acute angle Θ between the propagating ridge and a propagator wake and knowing the half spreading rate *v* from magnetic anomalies, the propagation rate *p* can be computed ($v/p = \tan \Theta$) (Kleinrock et al., 1997).

However, this basic propagating rift model from Hey (1977) has several approximations that deviate from real geological phenomena within the oceanic crust. These assumptions are:

- Relative seafloor spreading direction and rate between different ridges remain constant
- Spreading direction is parallel to the transform fault
- Only two plates are involved, and they both behave rigidly
- Small geometrical extent, so that the model can be treated as a plane problem
- The new rift extends instantaneously for a short distance, then spreads symmetrically for a while, and then extends instantaneously for another short distance. This process repeats in a systematic fashion.

The width of the 'V' pattern should be heavily dictated by the ratio between the spreading rate to the propagation rate. Sometimes the propagation extent of a certain spreading rift can be limited in space. For example, if the propagating ridge tries to migrate through an increasingly older crust, the propagation extent may get restricted because of the azimuth of the spreading center changes (Hey, 1977). In this case, the latest transform fault gets permanently established as a plate boundary. On the other hand, this attempt of propagating through old, thick crust may produce complex fracturing and readjustment of the spreading centers. These features are formed by the lengthening of one spreading segment at the expense of an offset neighboring spreading segment. The explanation for this statement can be found in the study of Kleinrock et al. (1997) regarding the slow-spreading segments of Mid Atlantic Ridge. In that study, the observed fast propagators have been concluded as a consequence of tectonic extension migrating along the ridge segments. In this particular case, the ridge segments change from more magmatic to less magmatic periods of spreading. Offsets of magnetic isochrons and morphological patterns for individual segments of ridges are the key geometrical trait of a propagator wake.

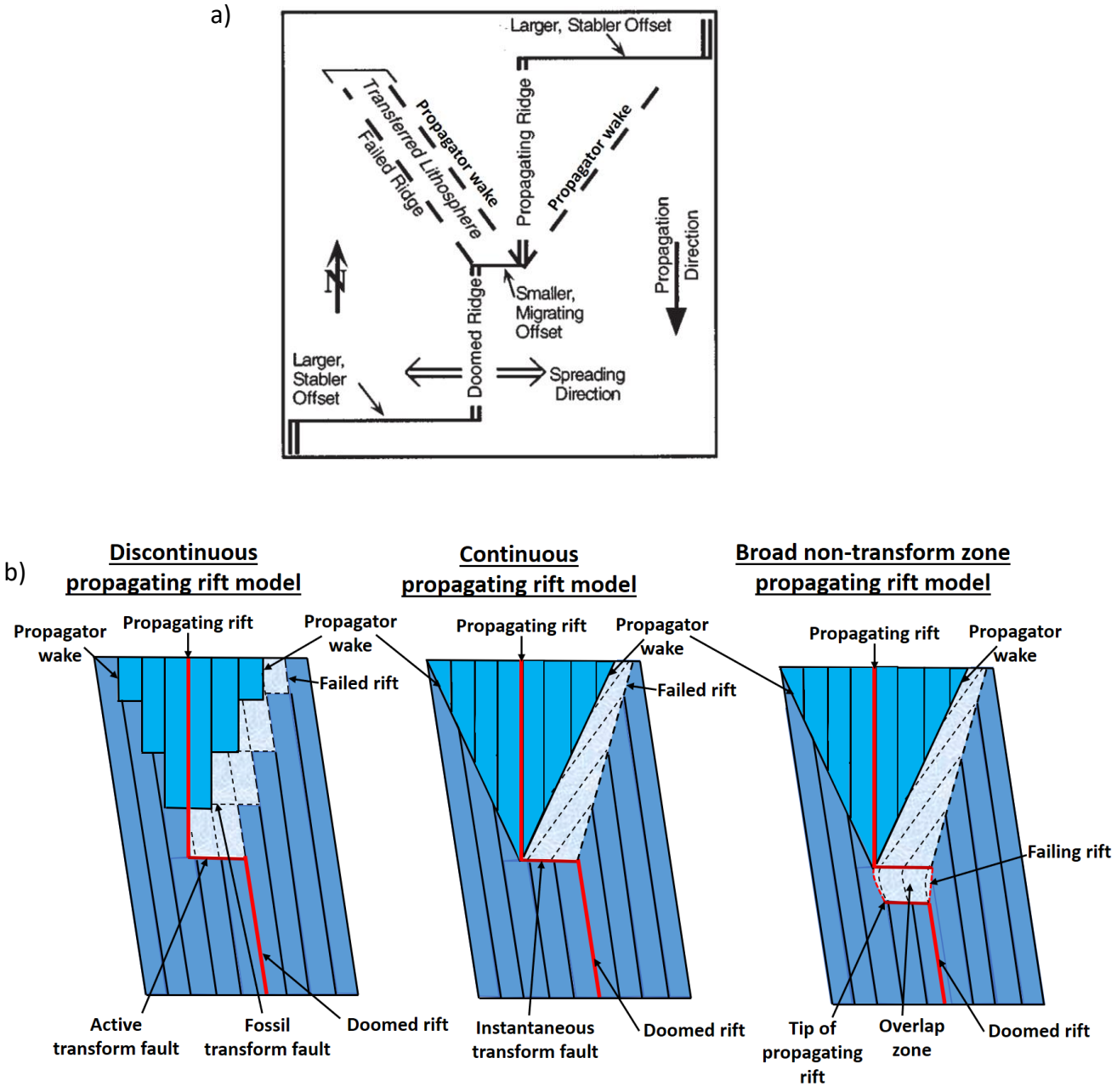

Figure 2.2: a) Schematic diagram of tectonic elements of propagating rift from Kleinrock et al. (1997) which is modified from Hey et al. (1986). b) Three different models of rift propagation were drawn after Hey et al. (1986). See text for details.

The propagating rift hypothesis established from the study of the Juan de Fuca plate (Hey, 1977) was tested on the oceanic crust near the Galapagos islands (Hey et al., 1986). This study was conducted based on the expedition to the Galapagos 95.5^{o} W propagating rift system. Sea beam or deep tow investigation from this Galapagos expedition corroborated the propagating rift as an explanation for the observed offsets in the magnetic isochrons on the oceanic crust. In Galapagos island, the Cocos-Nazca spreading center has a significantly higher amplitude magnetic anomaly to the east (between 95.5^{o} W and 85.5^{o} W) and a normal magnitude magnetic anomaly to the west. This pattern was explained via the magnetic telechemistry hypothesis as a function of rock chemistry. Magnetic telechemistry postulates that iron enrichment in mid-ocean ridge basalts is accompanied by an increased abundance of titanomagnetite, resulting in higher natural remanent magnetization and thus in enhanced magnetic anomaly amplitudes (Gee and Kent, 1998). Dredged basalts from high amplitude magnetic zones near Galapagos island with strong remanent magnetization that are rich in iron and titanium supported this hypothesis. After analyzing this geochemically interesting area from the perspective of tectonic evolution, sequential jumps of the spreading axis seemed responsible for the reorientation of the spreading center and systematic transformation of the lithosphere from the Cocos to Nazca plate (Hey et al., 1986). Three different geometries for propagating rift systems proposed by Hey et al. (1986) are shown in Fig. 2.2b. The first one (the leftmost diagram of Fig. 2.2b) is the Discontinuous Propagation Geometry. This pattern is developed from the alteration between spreading periods and instantaneous propagation periods. Characteristic

tectonic elements for this geometry include en-echelon failed rift segments and fossil transform faults that solidified into the progressively younger lithosphere. The resultant pattern of the propagator wakes seems jagged in discontinuous propagation geometry which was first hypothesized in Hey (1977). The second proposed geometry (the middle diagram of Fig. 2.2b) involves the Continuous Propagation of spreading rifts. Continuous and simultaneous lithospheric transfer dictate the overall pattern of this geometry. Velocities of rift propagation and seafloor spreading govern the overall orientation of isochrons and crustal structures in the zone of the transferred lithosphere. The third proposed geometry (the rightmost illustration in Fig. 2.2b), described in detail in Hey et al. (1986), is the most geologically valid one and is called Broad Transform Zone Geometry. The major difference between Continuous Propagation Geometry and Broad Transform Zone Geometry is the absence of continuously migrating transform fault in Broad Transform Zone Geometry. Instead, Broad Transform Zone Geometry can be classified by a shear zone between the propagating rift and the axis of the failing rift. Deformation within the overlap zone is essentially preserved in the zone of propagator wake (Hey, 2020). It is important to note that although continuous rift propagation showing Broad Transform Zone Geometry is the most plausible scenario for large-scale mapping, the rift propagation and spreading center failure still occurs in discrete segments on a very fine to fine-scale (Hey et al., 1986). Whereas standard rigid plate geometry can explain the outside area of propagator wake and zone of the transferred lithosphere, it fails to clarify the geometry of the overlapped zone between propagating and retreating ridges. This was outlined by Hey (2020) who also suggests that bookshelf

faulting is probably responsible for accommodating the shear between propagating and failing rifts in their zone of overlap which ultimately results in oblique seafloor fabric with trends considerably different from the ridge or transform parallel structures.

2.1.3.2 Propagator wakes in other regions

Propagator wakes are not exclusive to the CSZ. For example, these structures are also found in Galapagos Island (Hey et al., 1986) which has been mentioned in the previous section. Sreejith et al. (2016) have mapped several propagator wakes over the north-western part of the Indian ocean from gravity data (Fig. 2.3).

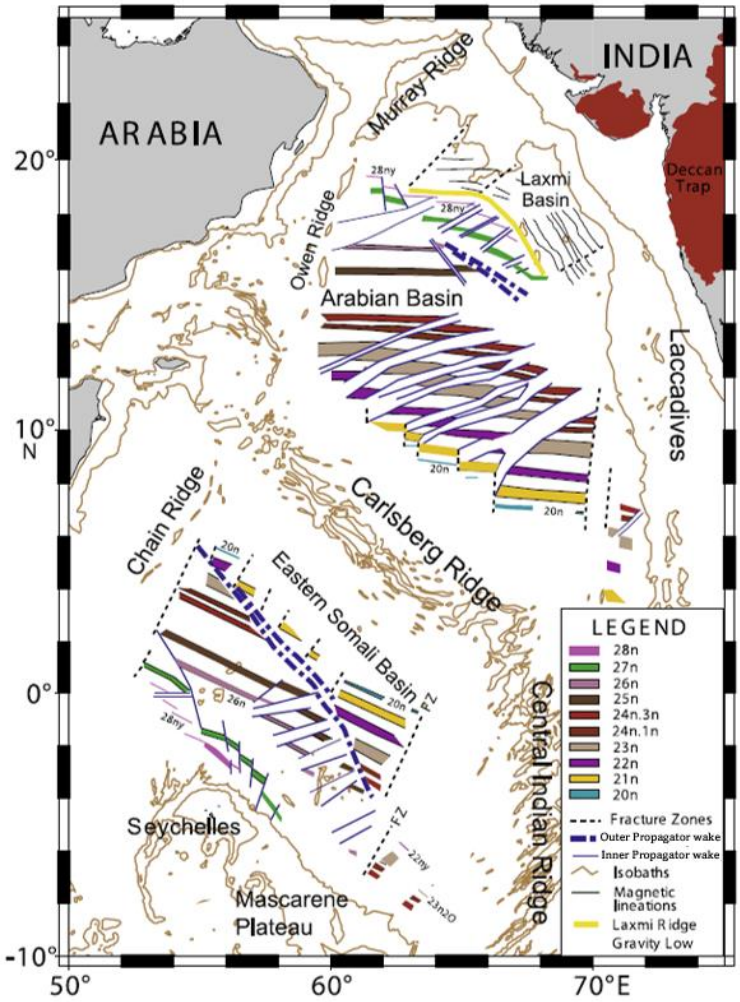

Figure 2.3: Propagator wakes in the northern Indian ocean (Sreejith et al., 2016)

Harper et al. (2021) also identified several 'W' shaped propagator wakes over the Indian ocean but on the southern part from bathymetry and vertical gravity gradient (Fig. 2.4). They have termed these features as 'seesaw propagators' because of their 'W' shape on a map, which is explained as a sudden reversal in propagation direction during the formation of the oceanic crust.

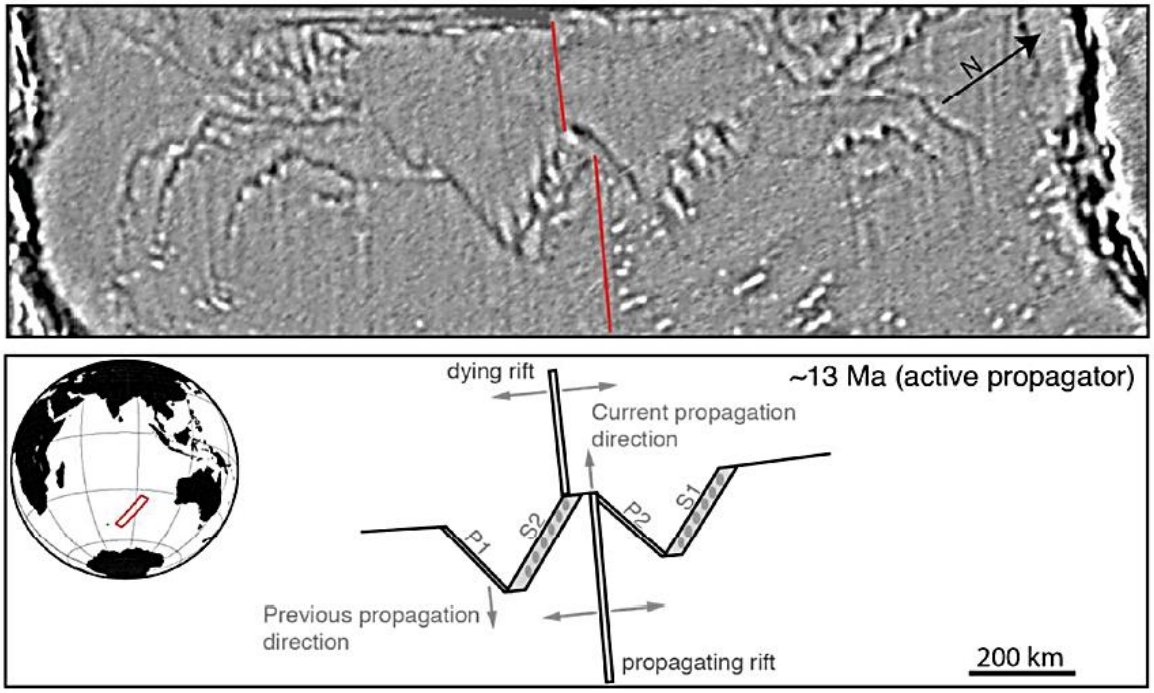

Figure 2.4: Seesaw propagator wake in the southern Indian ocean (Harper et al., 2021)

There is also recent evidence of oceanic rift propagation both north and south of Iceland mapped from gravity data (Fig. 2.5). The magnetic anomaly pattern also indicates the ongoing propagations both toward and away from Iceland (Hey, 2020).

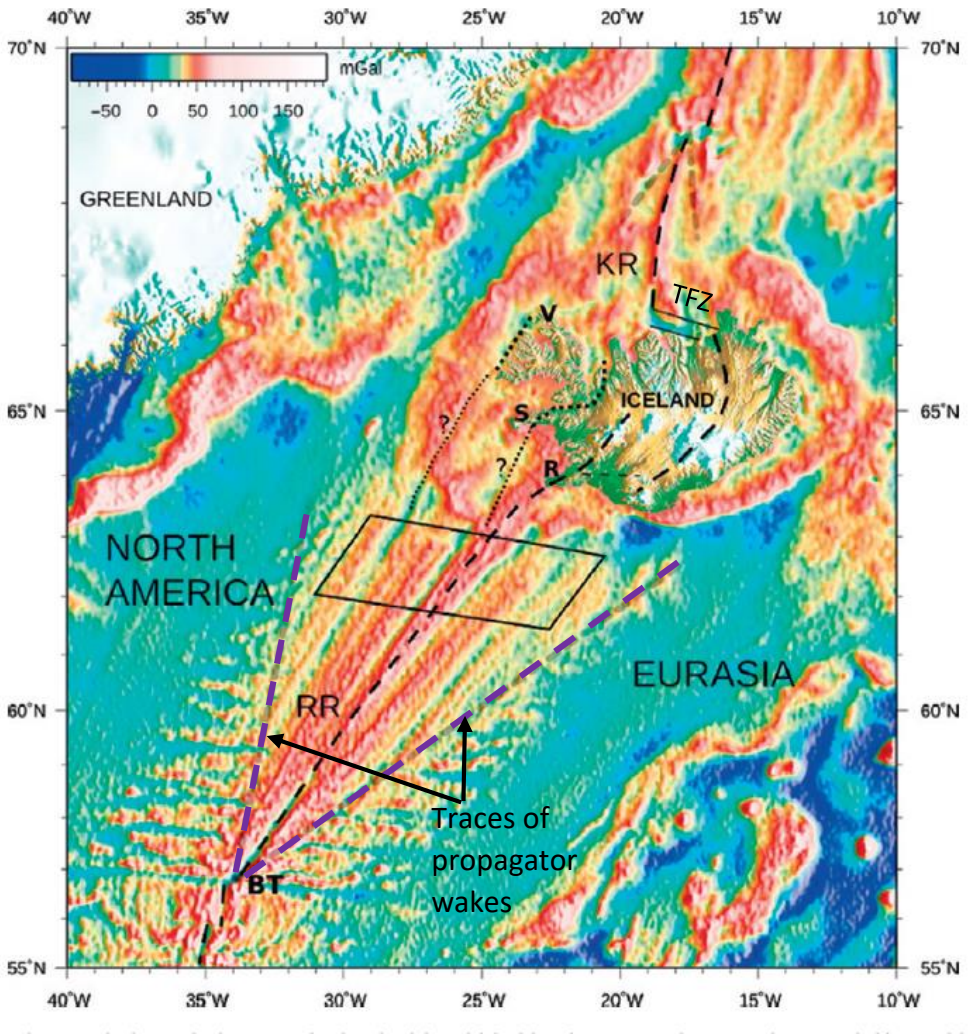

Figure 2.5: Satellite gravity map of Iceland with its tectonic boundaries (Hey, 2020). Purple dotted lines in this map show the trace of propagator wakes. Reykjanes Ridge (RR), Kolbeinsey Ridge (KR), and their extensions through Iceland are shown by dotted black lines. TFZ - Tjornes Fracture Zone; V - Vestfirdir; S - Snæfellsnes; R - Reykjanes Peninsula.

2.1.3.3 Internal architecture and physical properties of propagator wakes within the JdF plate

Hasselgren et al. (1992) first attempted to study the internal crustal architecture of these propagator wakes of the JdF using seismic reflection data. They observed subcrustal dipping reflectors for every propagator wake indicating a zone of thickened crust at the edge. According to their interpretation, this thickened crust was generated from increased magma supply toward the ridge during rift propagation. Marjanović et al. (2011) provided a study on crustal architecture and physical properties of propagator wakes of the JdF plate based on seismic reflections and gravity modeling (Fig. 2.6). According to their study, propagator wakes are associated with thinner oceanic crust in the middle (i.e., approximately 0.5 km thinner) bounded by denser and thicker crust at the edges of the structure. They correlated this thicker and denser crust of propagator wakes with iron enrichment through subcrustal magma lenses which are reported to be observed in seismic reflection images in Nedimović et al., (2005).

Marjanović et al. (2011) developed several gravity models across three different JdF ridge segments (Fig 1.1). Here only the gravity models will be discussed that are on the JdF plate. To constrain their model, they have used multichannel seismic reflection data from Cruise EW0207 (Carbotte et al., 2002). Starting from the northern part of the JdF ridge system, their first model (Fig. 2.6a) goes through the Endeavor segment (Fig. 1.1). This Endeavor model coincides with our northern 2D plate-scale geophysical model that ends in continental Washington (Fig. 1.1) and will be described in detail in Chapter 5. The Endeavour model of Marjanović et al., (2011) crosses the propagator wake segment

which is categorized as propagator wake 'ii' in our study (Fig. 1.1). Within the zone of propagator wake 'ii', the gravity model of Marjanović et al. (2011) shows an ~0.5 km thinner and 0.03 g/cc denser crust with respect to the surrounding crust (Fig. 2.6a).

Fig. 2.6b shows the gravity model of Marjanović et al., (2011) over the Northern Symmetric spreading segment of the JdF ridge system (see location in Fig. 1.1). This model crosses the propagator wake 'ii' twice (Fig 1.1). Marjanović et al. (2011) developed two different models for two zones of this propagator wake (Fig. 2.6b). One model goes through the western segment of propagator wake 'ii'. The other model passes the eastern segment of propagator wake 'ii'. Both zones of that propagator wake also show thinner and denser crust (0.02 to 0.04 g/cc) than the surroundings (Fig. 2.6b).

The most southern gravity model of Marjanović et al. (2011), shown in Fig. 2.6c, crosses the Cleft spreading ridge segment (Fig. 1.1). This model goes through one propagator wake which is categorized as propagator wake 'iii' (Fig. 1.1).

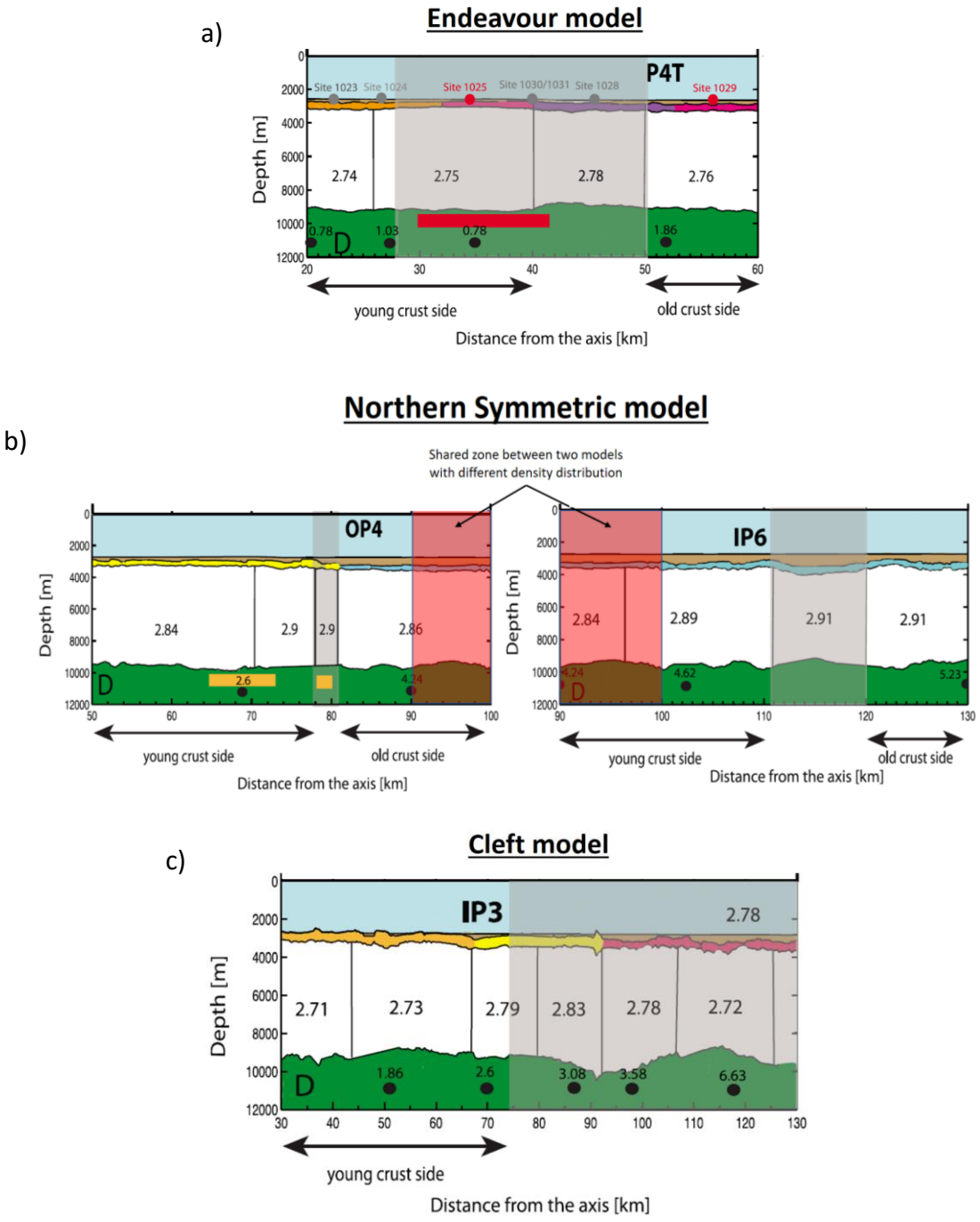

Figure 2.6: Gravity models from Marjanović et al. (2011) near three different JdF ridges namely Endeavor (a), Northern Symmetric (b) and Cleft (c). Values within the oceanic crust (white blocks) represent densities in g/cc. The black circles within the mantle (green layer) show the interpreted age of oceanic crust in million years. The grey shadow box indicates the extent of propagator wakes. The red circles in 'a' specify the ODP (i.e., Ocean Drilling Project) drilling depth at those locations. The red bar in 'a' designates the horizontal location of interpreted high FeTi basaltic rocks. Locations of these gravity models are shown in Fig. 1.1.

2.2 Continental domain

2.2.1 Siletz Terrane

In the continental portion of the CSZ, the subsurface rocks are of basaltic origin instead of granitic ones. These basaltic rocks are there because of the accretion of an island terrane called Siletzia. This Siletz terrane is primarily a large igneous province of Eocene age that is now located in the Cascadia forearc region of Vancouver Island, Oregon and Washington (Fig. 1.1). This igneous body has an approximate magmatic volume of 2.6 X 10^6 km^3 (Trehu et al., 1994). Subsurface rocks of this accreted terrane are composed of basaltic rock types such as massive flows, pillow lavas and intrusive sheets (Snavely et al., 1968; Wells et al., 2014). According to several studies, the timing of the rapid eruption and intrusion can be approximated at ~56 - 49 Ma (Duncan, 1982; Massey, 1986; Haeussler et al., 2000; Hirsch and Babcock, 2009; Wells et al., 2014). There is evidence that the Siletz terrane was rotated after its formation and during the time of accretion (McCrory and Wilson, 2013). The thickest part of this terrane is located in central Oregon where it reaches up to 35 km (Trehu et al., 1994). In offshore Vancouver Island, the thinnest part (~6 km) of the Siletz terrane occurs (Hyndman et al., 1990). The western boundary of the Siletz terrane is exposed in several places and has been mapped from seismic reflection and magnetic anomaly data. However, the eastern boundary is buried underneath sediments of Willamette and Puget Sound basins or by volcanic rocks of the Cascades. Some researches suggest a possible correlation between the accretion of the Siletz terrane and break-up of the subducting Farallon plate that resulted in three microplates we observe today (e.g., Gao et al., 2011).

2.2.2 Willamette basin

Models developed in this thesis include another important geological province of the continental domain - the Willamette basin. This Tertiary and Quaternary basin is located in northwestern Oregon. The approximately 300 km long Willamette river and its tributaries are the main sources of sediment transported into this basin. The distribution of Miocene flood basalts of the Columbia River Basalt Group suggests the possible existence of a broad lowland in the present location of the northern Willamette basin (Gannett and Caldwell, 1998). The later periods of uplift of Cascade Ranges have further delineated the basin along the north-south axis of the regional synclinorium. This also facilitated the continued sedimentary deposition within the lowlands from the nearby mountain ranges (Yeats et al., 1996). Uplands of Columbia River Basalt Group rocks formed by subbasin subsidence and faulting separate the northern Willamette basin from its southern part in terms of lithology and overall tectonics (Crenna et al., 1994). The southern Willamette valley has been suggested as a strike valley in literature which is formed by softer geologic units (Sherrod and Pickthorn, 1989), while the northern Willamette basin is primarily considered as tectonic depression (Yeats et al., 1996). The valley and basin sediments of this area consist of fine-grained fluvial-lacustrine deposits near the bottom and coarse grained fluvial accumulations near the top (Gannett and Caldwell, 1998).

Chapter 3: Geophysical data

3.1 Topography and Bathymetry

The topography/bathymetry map of the Cascadia Subduction Zone is shown in Fig. 1.1. Data for developing this topographic grid were downloaded from an online repository of Scripps Institution of Oceanography, University of California, San Diego (https://topex.ucsd.edu/cgi-bin/get_data.cgi). These data were acquired from satellite altimetry and shipborne acoustic soundings (Smith and Sandwell, 1997). In the repository, the datasets are in global 1-minute grids which are stored as ASCII-XYZ files. These data (i.e., version 19.1 from TOPEX online repository) were gridded using the kriging algorithm of the Oasis Montaj Geosoft software with a 1000 meters sampling interval.

3.2 Gravity anomaly

The free air gravity dataset from Sandwell et al. (2014) has been downloaded from the same online repository. In Sandwell et al. (2014), new radar altimeter measurements from satellites CyroSat-2 and Jason-1 have been combined with previous datasets to construct the global gravity model downward continued to the sea-level datum. The latest version of this gravity data (version 29.1) has been used in this study. Similar to the topographic data, the gravity data was also gridded in Oasis Montaj Geosoft software with a kriging algorithm and 1000 m sampling interval (Fig 3.1a). The free air anomaly does not take account of the gravity effect of the oceanic water. To account for that, Bouguer correction should be computed and applied, resulting in the Bouguer

gravity anomaly. Bouguer correction is done by approximating the topography above the sea level or the water column below the sea level with an infinite slab:

Bouguer correction (BC) = $2\pi\Delta\rho GH$……..(i)

In equation (i), Δρ is the density difference, G is the gravitational constant, and H represents the thickness of water. On land, Δρ represents the density difference between air and rock mass above the datum. Offshore, Δρ is the density contrast between water and sea-floor sediments. For this study, the assumed density contrasts of 2.67 g/cc and -0.97 g/cc have been used for the continental and oceanic domains respectively. The Bouguer gravity anomaly (Fig.3.1.b) was calculated by subtracting the Bouguer correction from the free air gravity anomaly.

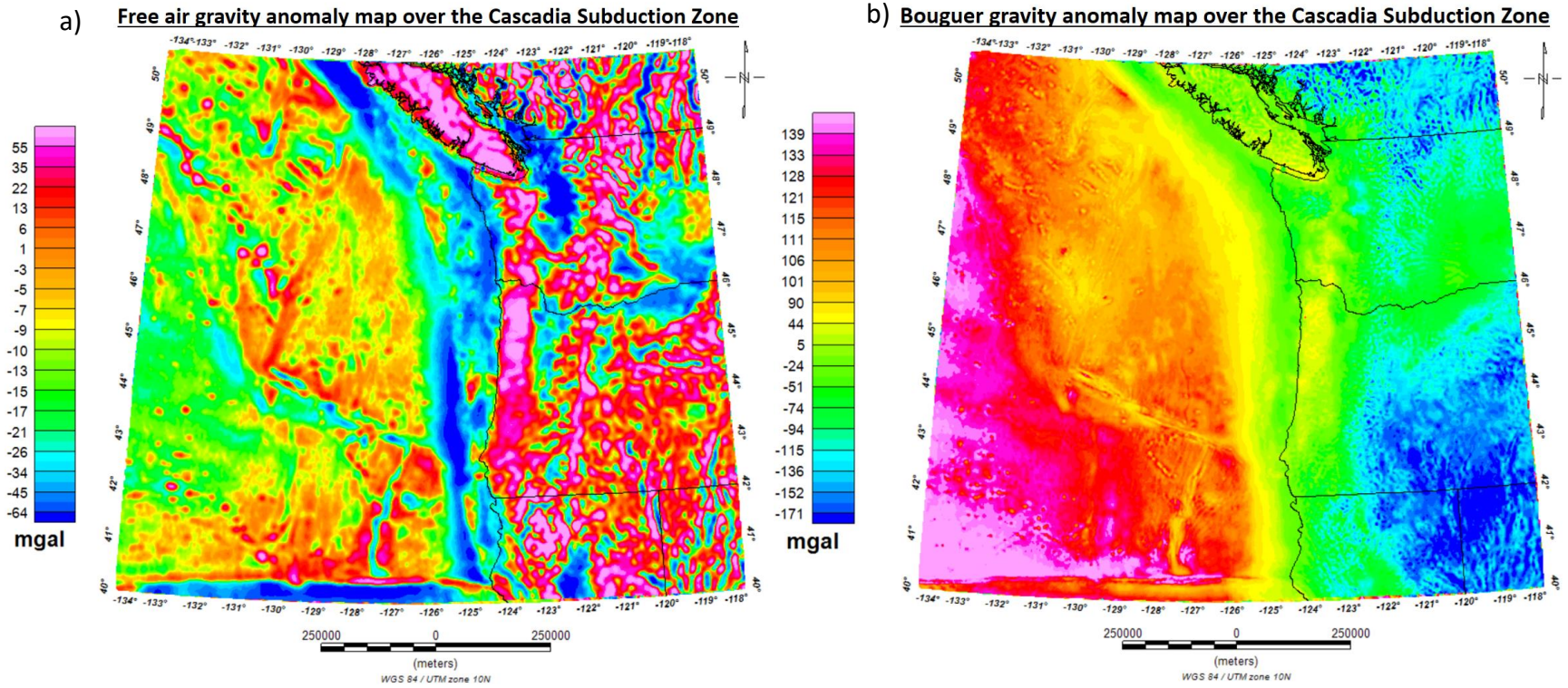

Figure 3.1: Gravity map for the entire CSZ. a) Free air gravity data from Sandwell et al. (2014) b) The Bouguer gravity anomaly.

3.3 Magnetic anomaly

The magnetic anomaly map (Fig. 3.2) from the United States Geological Survey (USGS) magnetic data repository (Bankey et al., 2002; https://mrdata.usgs.gov/magnetic/) was used in this study. The downloaded magnetic anomaly data was in a grid file format (Fig. 3.2.a) which is supported by Oasis Montaj Geosoft software with 1000 m spacing. The original DNAG projection of the grid file has been converted into WGS 1984/UTM projection 10N. The downloaded grid shows a magnetic anomaly at 305 m above the terrain as it was compiled by USGS (Bankey et al., 2002).

Based on the geographic position of the study area (i.e., Pacific Northwest of North America) the magnetic anomaly grid has been reduced to the pole (Fig. 3.2b). Generally, reduction to the pole removes anomaly's asymmetry caused by magnetic inclination and centers anomalies above the causative bodies. To convert the magnetic anomaly grid into the reduced to pole magnetic anomaly, magnetic inclination, declination, and total magnetic field values are required. These parameters were calculated using the International Geomagnetic Reference Field-13 (available at https://www.ngdc.noaa.gov/geomag/calculators/magcalc.shtml?useFullSite=true). The 2002 magnetic epoch was used: declination of 17.58°, inclination of 65.18°, and 52187.3 nT for the total intensity of the magnetic field.

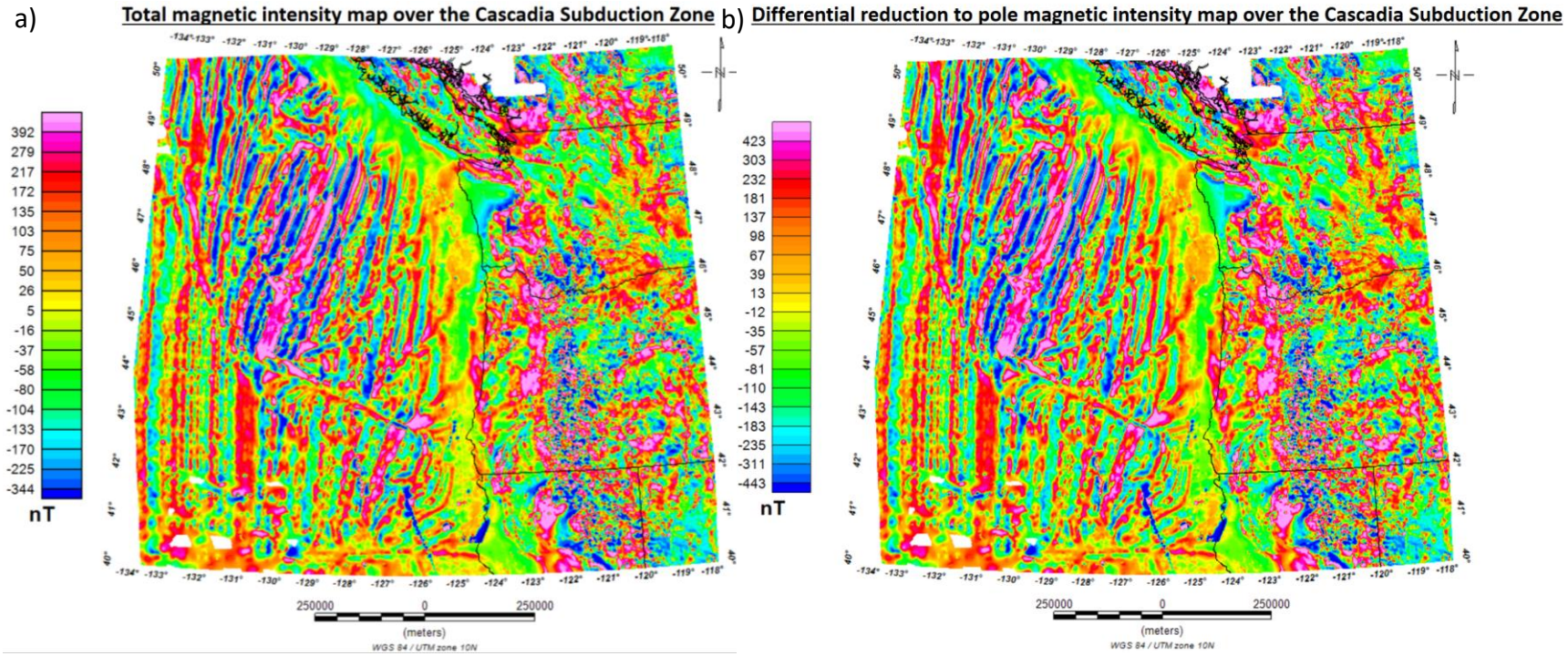

Figure 3.2: Magnetic map for the entire CSZ. a) Total magnetic intensity downloaded from https://mrdata.usgs.gov/magnetic/ b) Differential reduction to pole magnetic anomaly

3.4 Seismic data

Both seismic reflection and refraction datasets were used in this study. Seismic reflection profiles were primarily utilized to understand crustal structures of the non-subducting part of the oceanic plate. The locations of seismic reflection lines from eight surveys over the Juan de Fuca plate are shown in Fig. 1.1, including several vintage (i.e., the 1960s to 1970s) single-channel seismic reflection surveys RC1110 and RC1501 shown in Fig.3.3. These vintage seismic reflection lines do not image deep tectonic structures (such as oceanic Moho) or complex crustal features, such as crustal faults. Nevertheless, sedimentary layers and the top of the JdF oceanic crust can be interpreted confidently from these vintage seismic images, revealing several buried seamounts (Fig. 3.3).

Fig. 3.4 shows the regional or plate-scale seismic reflection lines from Han et al. (2016) extending from the JdF ridge to the deformation front that were utilized to constrain the non-subducting parts of the 2D integrated models (shown as black dashed lines in Fig. 1.1). These plate scale reflection lines (Fig. 3.4) have interpretations for almost every geological and tectonic feature of the JdF plate including the oceanic Moho. However, an analysis of original seismic reflection images of Washington (Fig. 3.4c) and Oregon (Fig. 3.4d) transects suggests that some crustal fault interpretations may relate to some artifacts, such as strong linear reflections potentially resulted from incorrect velocities used for the seismic migration process (labeled in Fig. 3.4c). For this reason, no interpretations of crustal faulting were used in this study.

a)

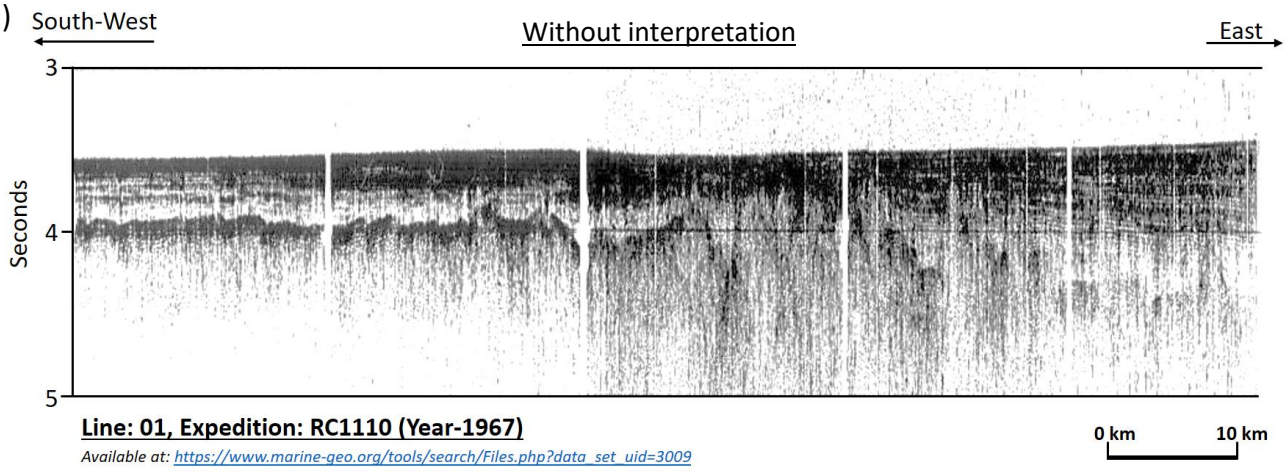
South-West
Without interpretation
East
3
4
5
Seconds
Line: 01, Expedition: RC1110 (Year-1967)
Available at: https://www.marine-geo.org/tools/search/Files.php?data_set_uid=3009
0 km
10 km

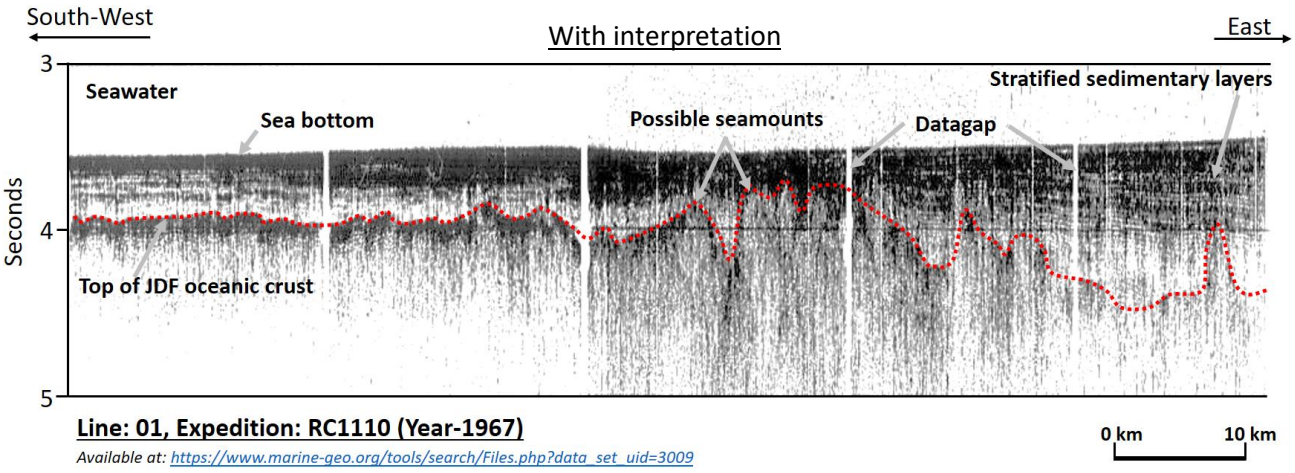
South-West
With interpretation
East
3
4
5
Seconds
Seawater
Sea bottom
Possible seamounts
Datagap
Stratified sedimentary layers
Top of JDF oceanic crust
Line: 01, Expedition: RC1110 (Year-1967)
Available at: https://www.marine-geo.org/tools/search/Files.php?data_set_uid=3009
0 km
10 km

b)

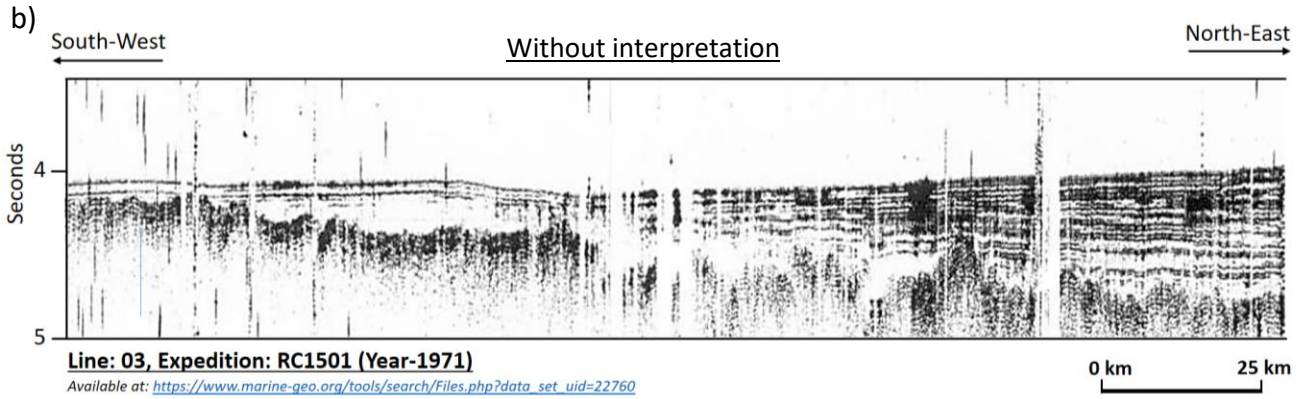
South-West
Without interpretation
North-East
Seconds
4
5
Line: 03, Expedition: RC1501 (Year-1971)
Available at: https://www.marine-geo.org/tools/search/Files.php?data_set_uid=22760
0 km
25 km

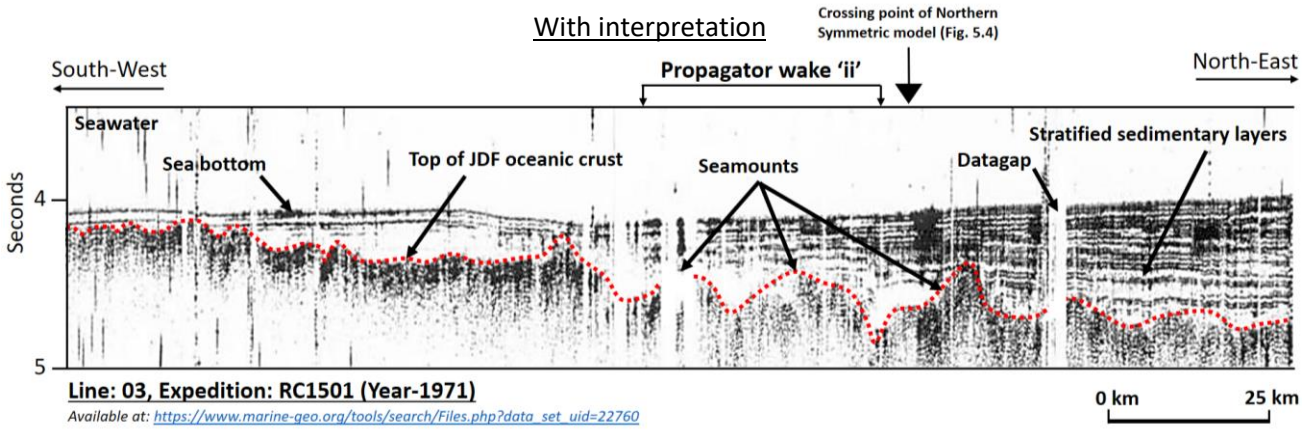
With interpretation
Crossing point of Northern Symmetric model (Fig. 5.4)
South-West
Propagator wake 'ii'
North-East
Seawater
Sea bottom
Top of JDF oceanic crust
Seamounts
Datagap
Stratified sedimentary layers
Seconds
4
5
Line: 03, Expedition: RC1501 (Year-1971)
Available at: https://www.marine-geo.org/tools/search/Files.php?data_set_uid=22760
0 km
25 km

c)

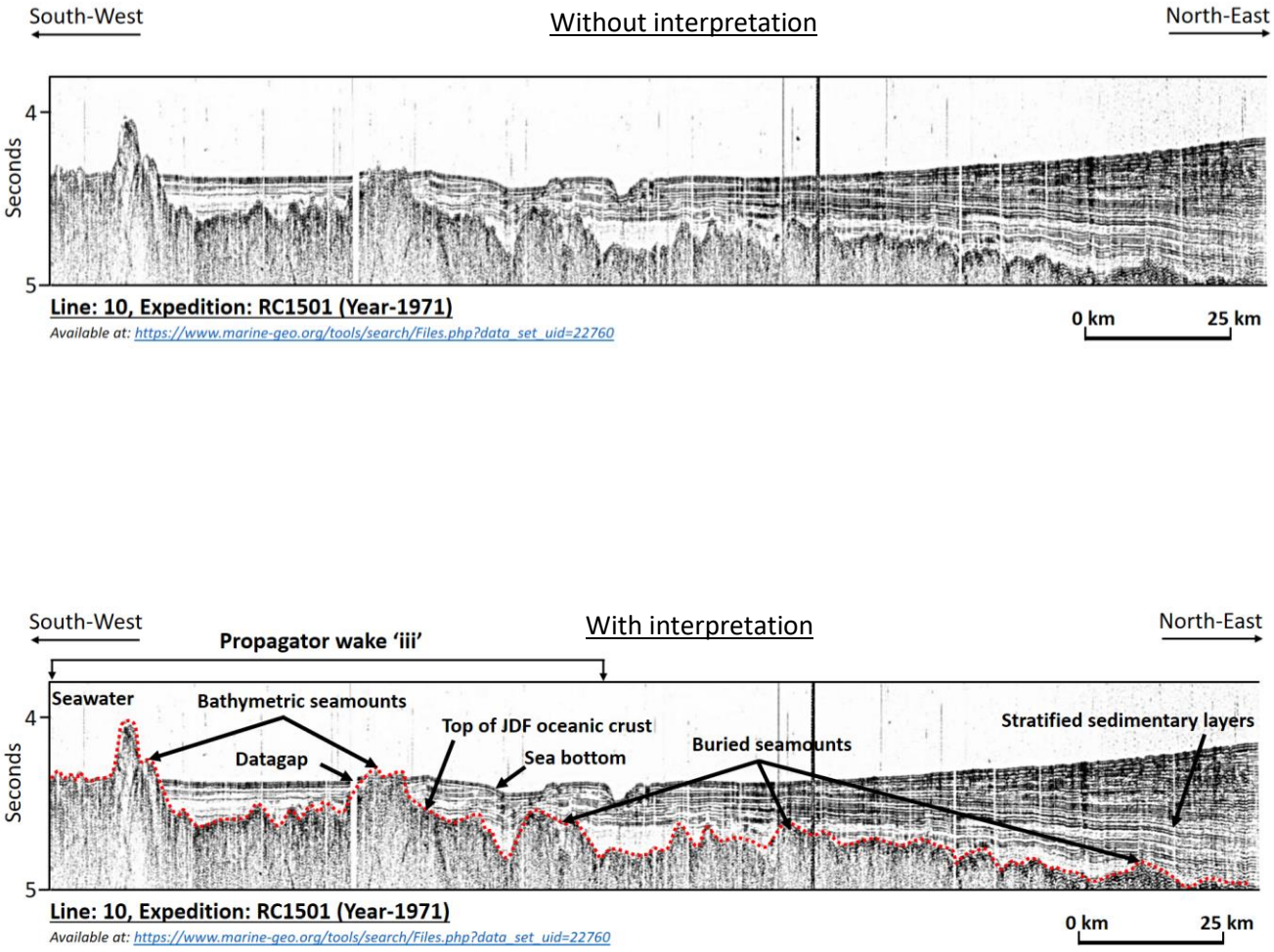

Figure 3.3: Three different vintage seismic reflection images from cruise expeditions RC1110 (a) and RC1501 (b and c) with possible interpretations. The geographic locations of these seismic lines are shown in Fig. 1.1

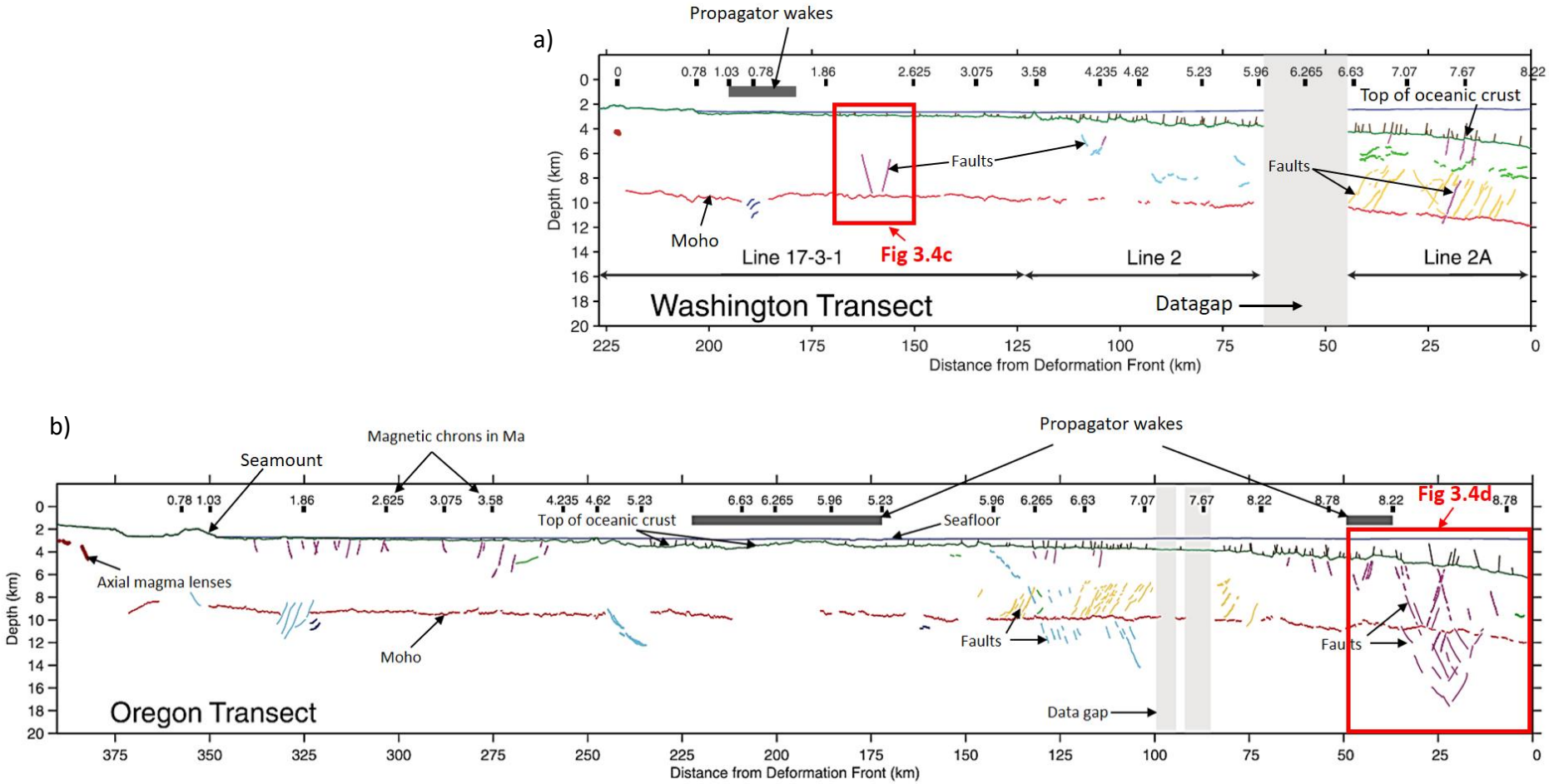
a)
Propagator wakes
Top of oceanic crust
Faults
Faults
Moho
Fig 3.4c
Line 17-3-1
Line 2
Line 2A
Washington Transect
Datagap
Depth (km)
Distance from Deformation Front (km)
b)
Magnetic chrons in Ma
Seamount
Propagator wakes
Fig 3.4d
Top of oceanic crust
Seafloor
Axial magma lenses
Moho
Faults
Faults
Oregon Transect
Data gap
Depth (km)
Distance from Deformation Front (km)

c)

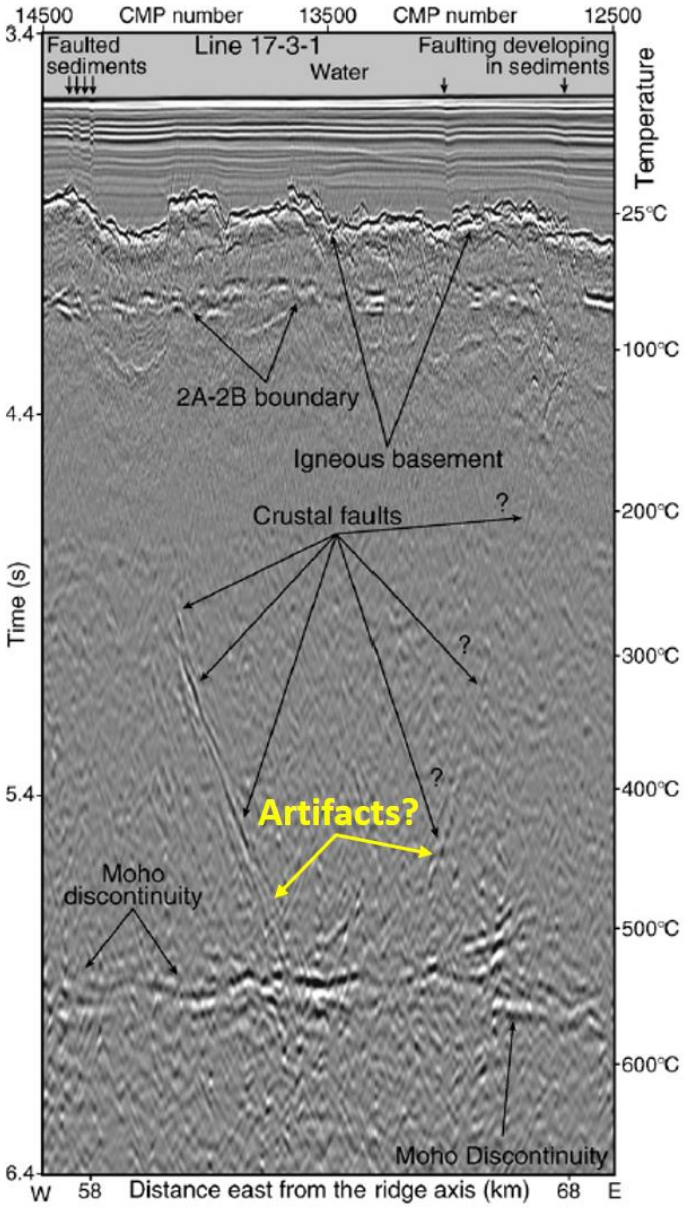
14500
CMP number
13500
CMP number
12500
3.4
Faulted sediments
Line 17-3-1
Water
Faulting developing in sediments
Temperature
25°C
100°C
2A-2B boundary
4.4
Igneous basement
Crustal faults
?
200°C
Time (s)
?
300°C
?
5.4
Artifacts?
400°C
Moho discontinuity
500°C
600°C
Moho Discontinuity
6.4
W
58
Distance east from the ridge axis (km)
68
E

d)

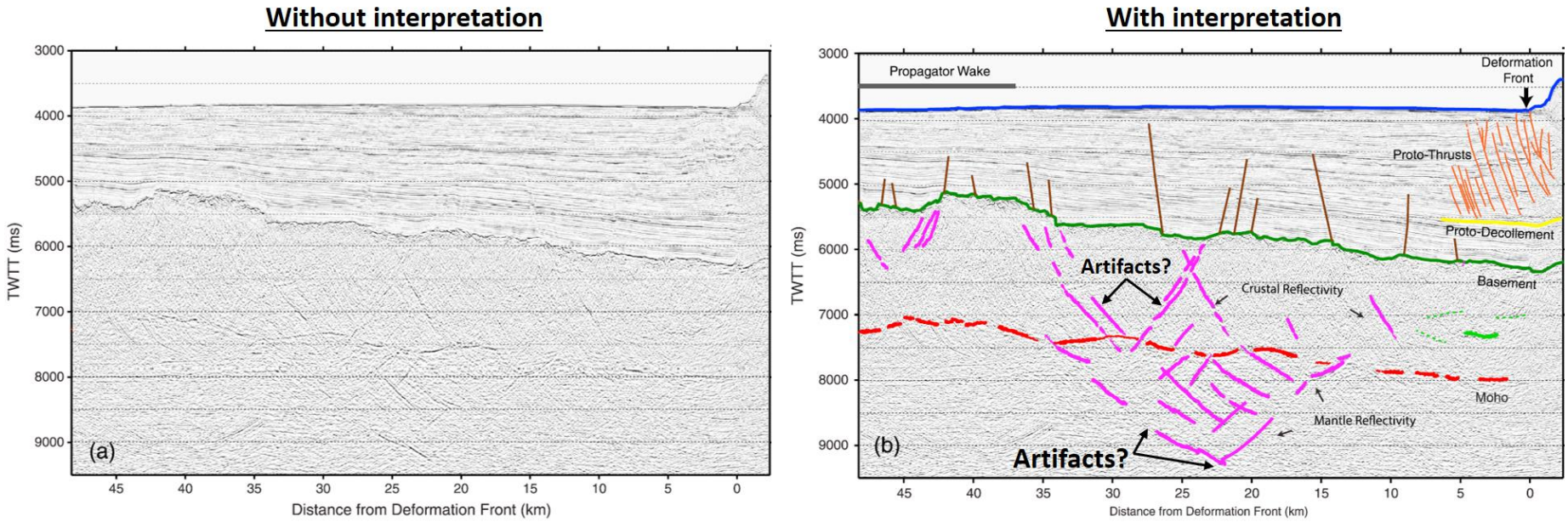

Figure 3.4: Plate-scale seismic reflection images from Han et al. (2016). a) A combined interpretation of seismic reflection lines from several surveys throughout the northern JdF plate (see Fig. 1.1 for location) offshore Washington. b) Seismic reflection line over the southern JdF plate offshore Oregon. c) A portion of Seismic reflection image from Washington transect from Nedimovic et al., (2009). The location of this image is shown in the Washington transect (a) with a red rectangle d) Seismic reflection image from a part of the Oregon transect (Han et al., 2016). The location of this image is also shown in the Oregon transect (b) with a red rectangle

Seismic refraction data are also a vital part of this study (see locations in Fig.1.1). They have been used mostly for constraining near offshore, offshore and continental regions of the integrated 2D models. Primarily, velocity models from two seismic refraction experiments over Washington (Fig. 3.5a; Parsons et al., 2006) and Oregon (Fig 3.5b; Trehu et al., 1994; Parsons et al., 2006) were utilized. These experiments provide seismic P-wave velocities for subsurface geological layers that were used to guide the density distribution over and close to the continental domain in the integrated 2D models (to be described in Chapter 5).

a)

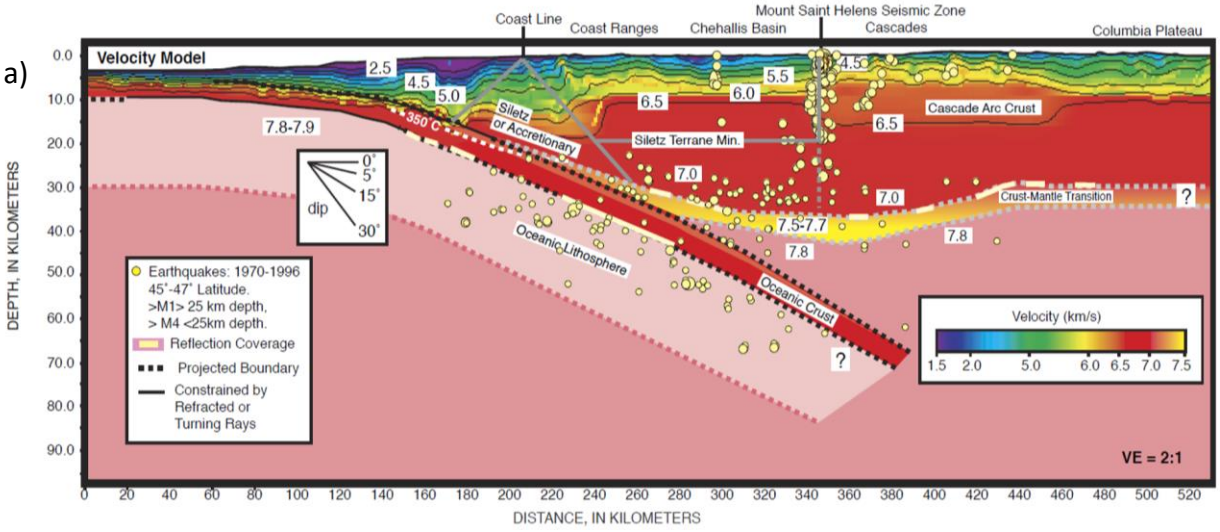

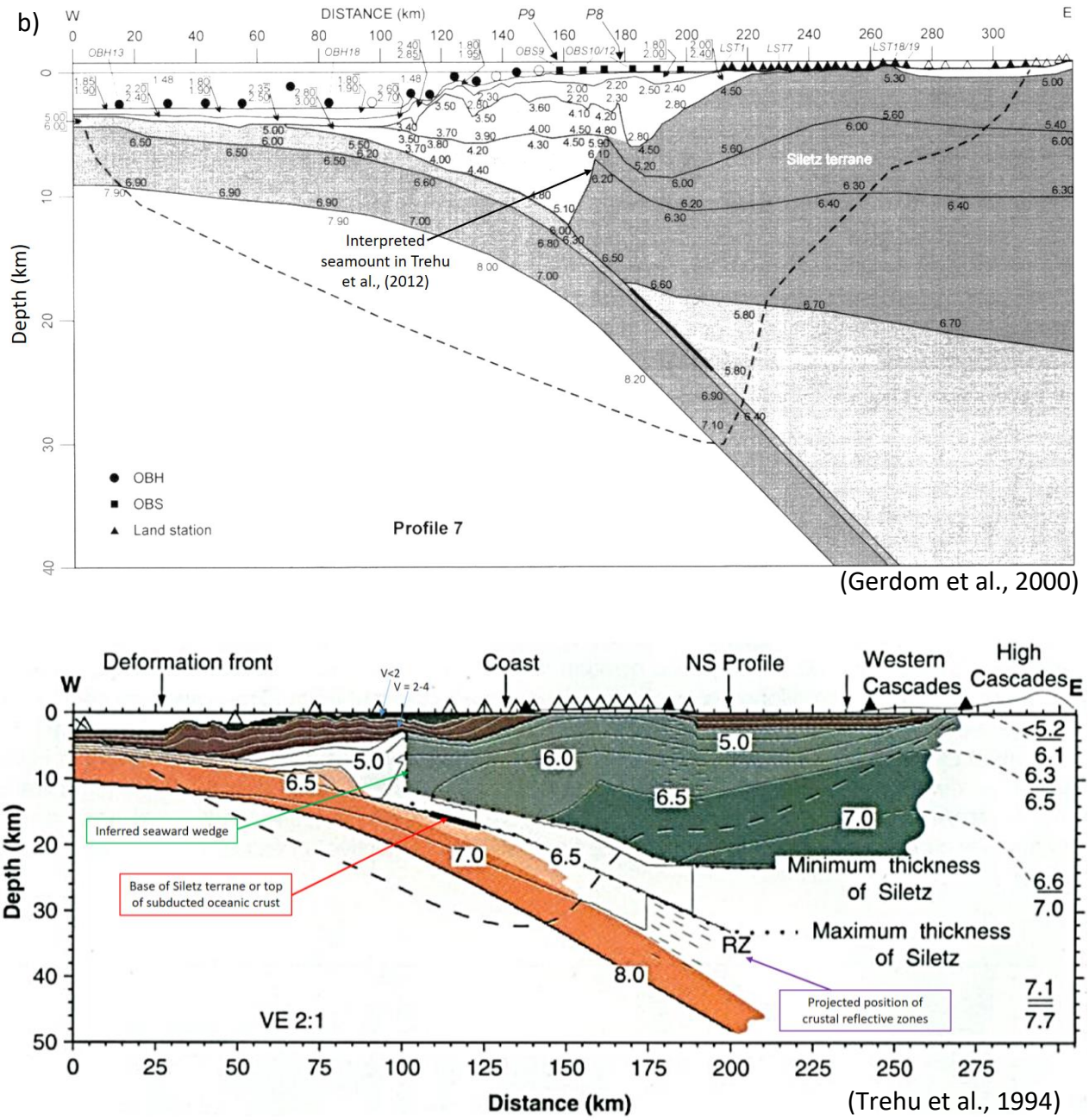

Figure 3.5: Velocity models developed from seismic refraction experiments for constraining the integrated 2D models of this study. Values noted in the geologic and tectonic features represent seismic P-wave velocity in km/s. a) Seismic reflection velocity model in Washington from Parsons et al. (2006) (see Fig. 1.1 for location). b) Velocity models from the same seismic refraction experiment in Oregon. The top velocity model is from Gerdom et al. (2000) and the bottom one is from Trehu et al. (1994). The western edge of the Siletz terrane in these velocity models is interpreted to have a seamount (Trehu et al., 2012)

3.5 Earthquake data

In this thesis, earthquake data have been utilized to understand the correlation between seismicity and tectonic features. The data have been collected from the online earthquake catalog of the United States Geological Survey (USGS) (https://earthquake.usgs.gov/earthquakes/search/). However, only the earthquakes from the continental domain and near shore region are used in this study. The epicenters of the offshore earthquakes have significant errors because all of the seismometers are located on land. Only the earthquakes with magnitude 4 and above are shown in Fig. 1.1.

Chapter 4: Methodology

Two major methods have been adopted to investigate the geology and tectonics of the CSZ. The first methodology is the two-dimensional (2D) integrated geophysical modeling and the second one is the spatial geophysical analysis (Fig 4.1). The detailed workflow involving these two methods is shown in Fig. 4.1

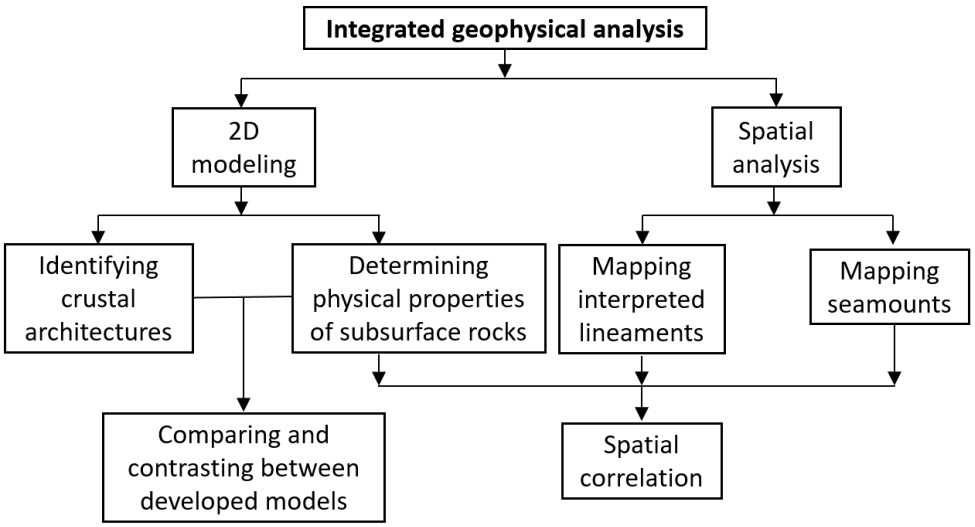

Figure 4.1: Simplified workflow illustrating integrated geophysical investigation adopted in this study.

4.1 2D integrated modeling

The primary objectives of two-dimensional integrated geophysical models are to investigate the physical properties (i.e., density and magnetic susceptibility) of subsurface rocks and to comprehend the variations in the crustal architecture in two regions of the study area. The developed regional or plate-scale models extend from JdF oceanic spreading center in the west to continental regions of North America in the east

(Fig. 1.1). Both potential field (i.e., gravity and magnetic) (Fig. 3.1 and 3.2) and seismic (i.e., reflection and refraction) data (Fig. 3.4 and 3.5) have been utilized to build these plate-scale models. While seismic data provides structural constraints, potential field data govern the physical property distribution of subsurface rocks.

Each model includes several geological layers, which are water, sediments, oceanic crust, mantle, accreted oceanic terrane on the continental domain and continental crust that contains arc volcanoes. The models are developed in the GM-SYS module of the Geosoft software. Each model has been extended to ±30000 km (i.e., infinity) in the horizontal axis to avoid regional edge effects. In the vertical axis, each model extends up to 90 km of depth from the mean sea level.

At the initial stage, the entire subsurface has been divided into a number of blocks. However, blocks within the same layer (e.g., JdF oceanic crust) may have different physical properties. For example, magnetic susceptibilities of the JdF oceanic crust have been distributed according to the positive and negative magnetic anomalies. Density values are assigned considering the values are close to the global average (Carlson and Herrick, 1990). These density values are then changed within a certain limit until a reasonable match between observed and calculated gravity anomaly was achieved. There is no single value that quantifies the reasonable matching between observed and calculated gravity anomalies. That value varies along the profile and strongly depends on the availability of constraints. For example, in the oceanic domain, the reasonable match between observed and calculated gravity anomalies is expected to be within 2 - 3 mGal because of the confident constraints from seismic reflection data (see section 5.1

for details). In contrast, in the continental domain only low resolution of seismic refraction data are available. Moreover, these constraints are located away from the modeled profiles. Therefore, the match between observed and calculated gravity anomaly in the continental domain was allowed to vary in greater amount to avoid overfitting. The detailed workflow regarding this development of 2D models are is shown in Fig. 4.2.

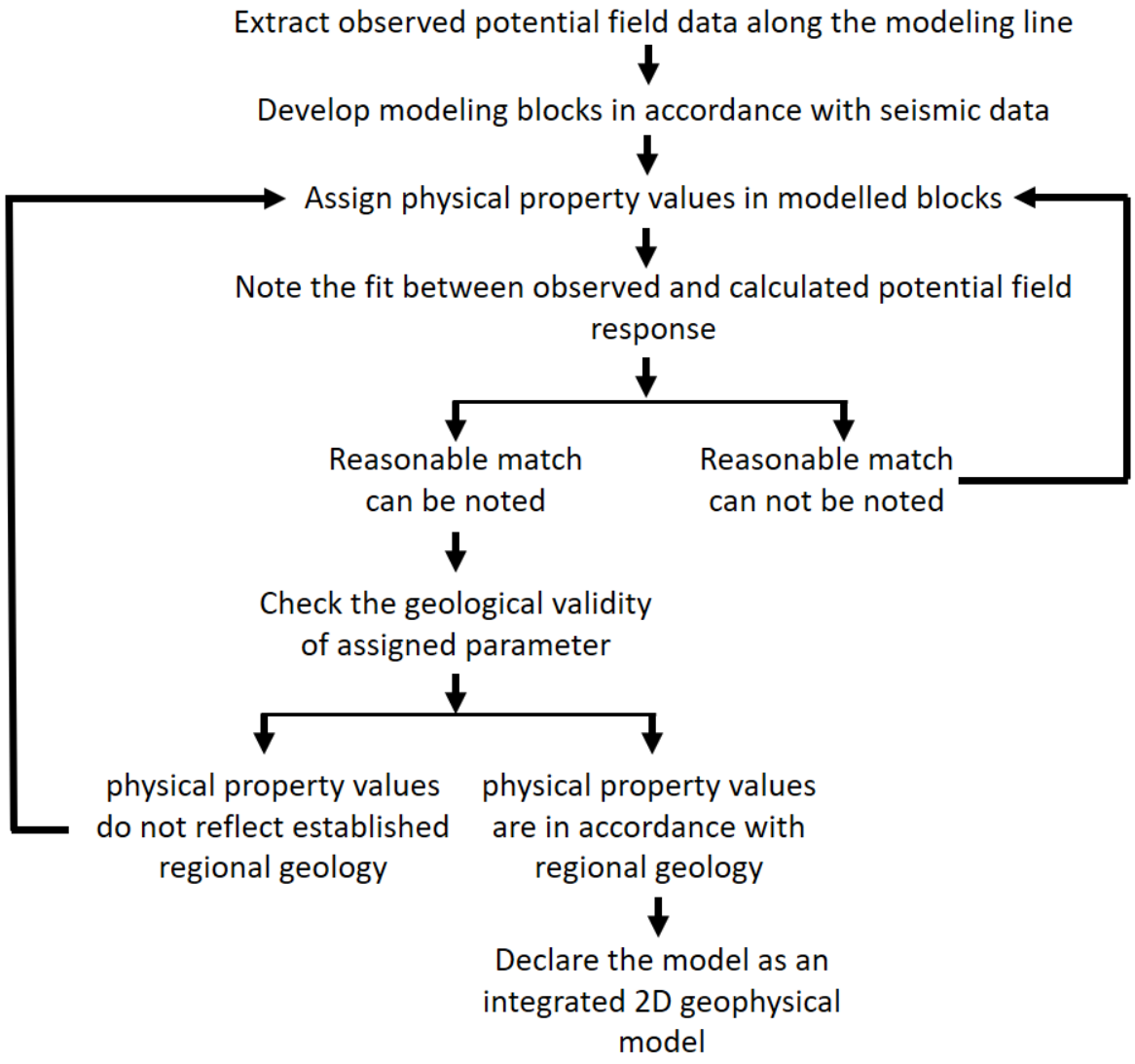

Figure 4.2: General workflow for developing an integrated 2D model

To match the observed potential field data with the calculated ones, one tie point is designated per anomaly profile based on the following criteria:

- Tie point must be placed over the location with the most confident subsurface structures where seismic interpretation is available for every layer in the model.
- In the location of the tie point, layers of the developed models (e.g., top sediment, crust and mantle) should be as flat as possible, so that their calculated response lacks high frequency variations.
- In this study, tie points are not located over the regions of anomalous crustal density (i.e., zones with densities that do not correspond to the established geological pattern).
- If magnetic data is involved in the 2D modeling, a tie point for the magnetic profile is placed at the same location as the tie point of the gravity profile.

Since the modeling lines and seismic refraction lines are not on top of each other (Fig. 1.1), the crustal architectures of the continental domain and near offshore were extrapolated (up to 30 km). The geometrical constraints on the modeling derived from seismic data (i.e., depth, thickness and width of individual layers) are listed in Tables 4.1 and 4.2.

Table 4.1: Constraints from seismic refraction data for Oregon model

Constrained parameters	**Source**	**Published Value**	**Input Value**
Depth of Willamette Basin	Trehu et al. (1994)	2.3 km	Max 2.3 km
	Gerdom et al. (2000)	0.74 km	
Top depth of less dense Siletz terrane (Westernmost point)	Trehu et al. (1994)	4.3 (meets at the eastern end of Seamount)	4.5 km
	Gerdom et al. (2000)	5.9 (meets at the eastern end of Seamount)	
Bottom depth of less dense Siletz terrane	Trehu et al. (1994)	3.7 km (with no sediment cover)	3.7 km (no sediment cover on top and western edge of Willamette basin) Max 5 km (beneath Willamette Basin) The western end ends up at the bottom of sed. basin
		6.1 km (under Willamette Basin)	
	Gerdom et al. (2000)	3.7 km (where no sediment cover)	
		4.7 (under Willamette Basin)	
Depth to the top of the densest sedimentary layer	Gerdom et al. (2000)	10 km (western end)	10.3 km (where the top meets the oceanic plate)
		5.1 km (eastern end)	5.6 km (where the top meets the Siletz terrane)
Top of oceanic crust (at the coastline)	Trehu et al. (1994)	23 km	23.3 km
	Gerdom et al. (2000)	24 km	
Top of oceanic crust (beneath accretionary prism)	Trehu et al. (1994)	9 km	9 km
	Gerdom et al. (2000)	10 km	
Oceanic Moho (at the coastline)	Trehu et al. (1994)	29 km	29.3 km
	Gerdom et al. (2000)	30 km	
Oceanic Moho (beneath accretionary prism)	Trehu et al. (1994)	14.8 km	14.9 km
	Gerdom et al. (2000)	14.9 km	

Table 4.2: Constraints from seismic refraction data for Washington model

Constrained parameters	**Source**	**Published Value**	**Input Value**
Depth of Willamette Basin	Parsons et al. (2006)	Maximum depth of 4.7 km	Maximum depth of 4.7 km
Top depth of Siletz terrane (Westernmost point)		2.7 km (Shallowest depth at the western edge)	2.8 km
		15 km (where it meets the oceanic plate)	15 km
Bottom depth of Siletz terrane		21.6 km (where it meets oceanic plate)	21.6 km
		35 km (at the westernmost edge)	35.5
Top of oceanic crust (at the coastline)		~21-22 km (meets the bottom of Siletz terrane)	~21-22 km
		15 km (meets the top of Siletz terrane)	15 km
Top of oceanic crust (beneath accretionary prism)		7.9 km (at the middle of the entire extent of the accretionary prism)	7.9 km
Oceanic Moho (at the coastline)		~28 km	~28 km
Oceanic moho (beneath accretionary prism)		23 km	21.5 km

4.2 Integrated spatial analysis

Gravity and magnetic grids were utilized for spatial analysis. A generalized workflow for filtering potential field data is shown in Fig. 4.3.

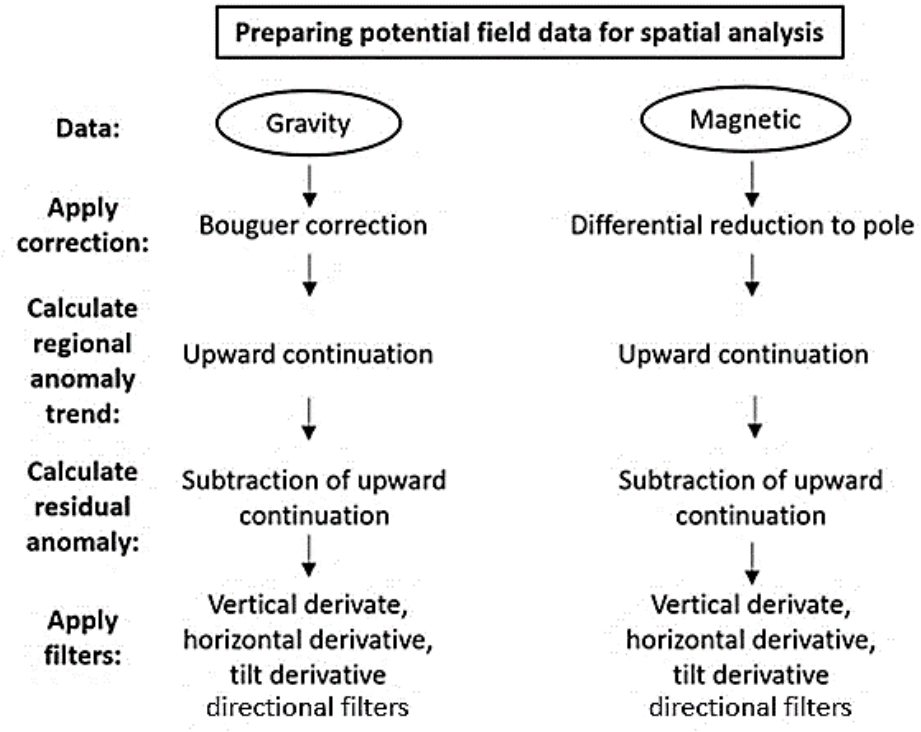

Figure 4.3: Diagram illustrating required steps to prepare potential field datasets for spatial geophysical analysis

The regional trend of the Bouguer gravity anomaly was computed by upward continuing the data to 8 km. This value was chosen based on trial and error from several elevation values (i.e., 10 km to 1.5 km) as it removes most of the high-frequency components resulting from shallow subsurface structures. This broad and smooth signal from deep regional sources was then subtracted from Bouguer gravity data to generate a residual anomaly that highlights shallow subsurface features.

For magnetics, differential reduction to the pole was calculated to correct for the skewness of observed anomalies caused by the non-vertical ambient field. A regional magnetic trend was then calculated via upward continuation to an elevation of 3 km.

Similar to gravity data, the trial and error process was also involved in choosing this elevation value. However, the lower elevation value of upward continuation for magnetics (i.e., 3km) than gravity (i.e., 8 km) is justified because the magnetic field decreases faster with distance than gravity (Telford et al., 1990). The regional magnetic trend was then subtracted from differential reduction to pole magnetics to produce the residual anomaly where signals from shallow subsurface structures are profound.

Several types of filters have been applied to the residual potential fields to highlight the tectonic structures of interest. The two most useful filters applied to the data are the first vertical derivative and tilt derivative. Additional filters, such as horizontal derivatives and directional filters (not shown) were also applied to the residual potential field data to aid in mapping the key tectonic features. Since all of the lineaments have been mapped from magnetic anomaly data, the disturbances in the sea-floor magnetic stripes were the primary control for picking a tectonic lineament. The identified lineaments must also agree with the locations of the structures derived in the 2D models. More details regarding lineament mapping will be discussed in section 5.2.1. The interpreted geologic structures from potential field data (e.g., buried seamounts) were cross-checked with seismic reflection data (Figs. 3.3 and 3.4).

4.3 Earthquake analysis

4.3.1 Selection of Wadati-Benioff earthquakes

Earthquake data from the USGS catalog range longitudinally from near offshore to the middle of British Columbia, Washington, Oregon and some parts of Northern California (Fig. 1.1). The hypocenters of these earthquakes extend from the top of the Siletz terrane to the Moho of the subducting JdF oceanic plate. However, the objectives of this study require investigating the earthquakes that occurred only within the subducting oceanic crust (i.e., Wadati-Benioff zone). Any discernable pattern within the earthquakes from the Wadati-Benioff zone will allow us to correlate mapped structures on the oceanic plate to generated seismicity.

The top surface of the JdF subducting slab from McCrory et al. (2012) (Fig. 4.4) has been utilized to select the earthquakes within the Wadati-Benioff zone. First, a surface for the bottom of the subducting JdF plate was developed in ArcGIS by adding 7 km to each point of the top of the subducting slab surface. The assumed crustal thickness of 7 km is constrained by seismic refraction data (see Fig. 3.5). 3D rasters have then been developed using the Triangular Irregular Networks (TIN) tool in ArcGIS for both the top and bottom of the JdF plate. After importing these 3D surfaces into ArcScene (i.e., a module of ArcGIS that uses a 3D environment), the earthquakes that are between these two layers are selected. From these selected earthquakes (Appendix A) only the ones with magnitudes greater than 3 were analyzed. One earthquake with a significant error

(value = 99 km) in horizontal location (i.e., error in epicenter) was excluded from the analysis.

4.3.2 Least square analysis in seismicity clusters

The methodology of analyzing the seismicity within the JdF plate has the primary goal of determining a discernable pattern (especially lineaments) within an earthquake cluster. Keeping this in mind, all of the selected earthquakes have been divided into several clusters that are oriented somewhat parallel to the subduction direction of the JdF plate. One such cluster is shown in Fig. 4.4 with a purple rectangle.

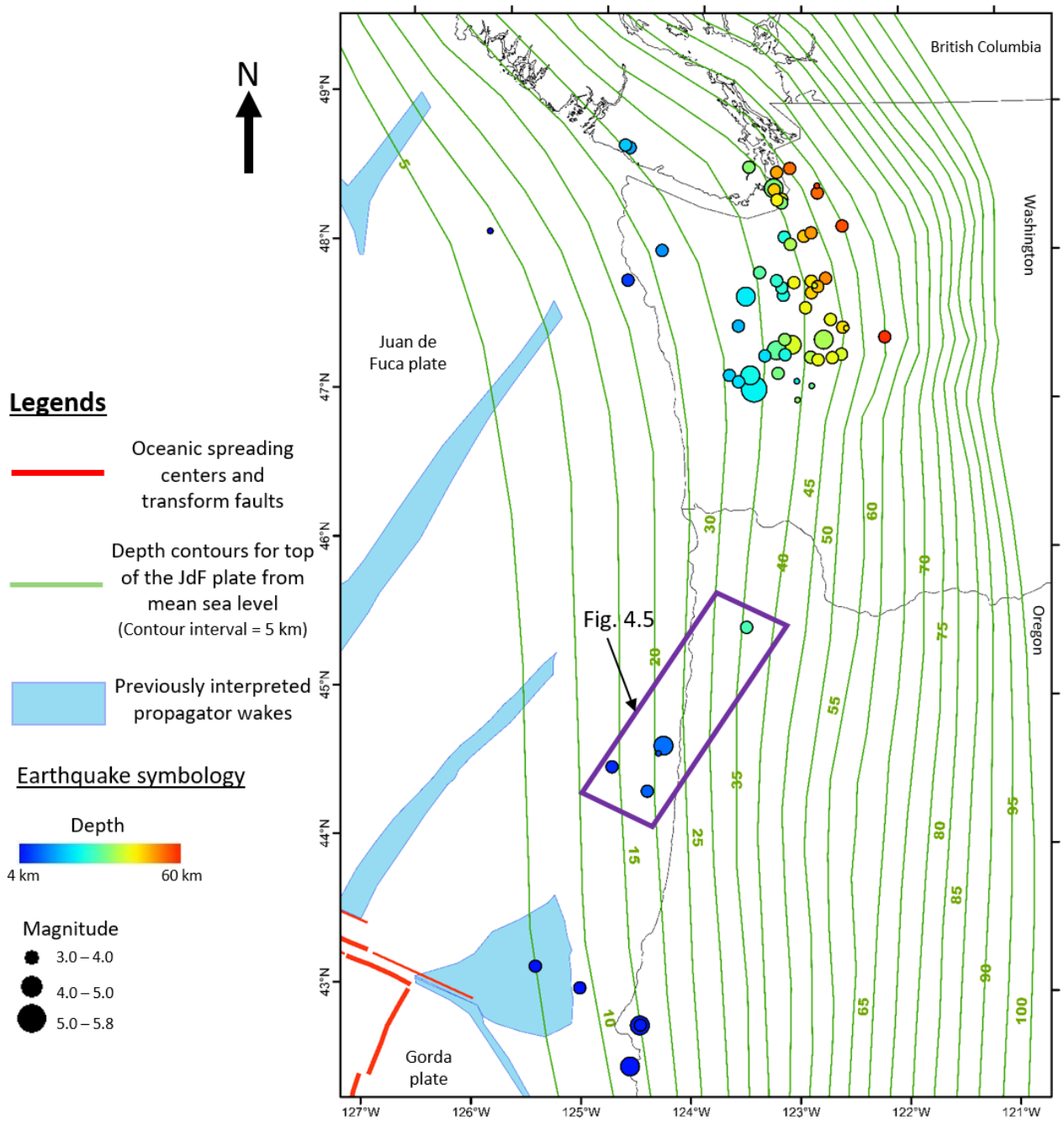

Figure 4.4: Depth to the top of JdF plate along the CSZ digitized from McCrory et al. (2012) (light green contour lines). The earthquakes shown in this map are within the Wadati-Benioff zone. The least square analysis for events within the purple rectangle is illustrated in Fig. 4.5.

After, dividing the earthquake dataset into several clusters, the Ordinary Least Squares (OLS) tool of ArcGIS has been utilized to perform linear regression analysis on each cluster. Then 'Points to Line' tool was used to draw a line through the least deviated points from the mean (i.e., points with standard deviation between - 0.5 and 0.5). This line represents the statistical best fit line through an earthquake cluster. This entire process of statistical analysis is illustrated in Fig. 4.5.

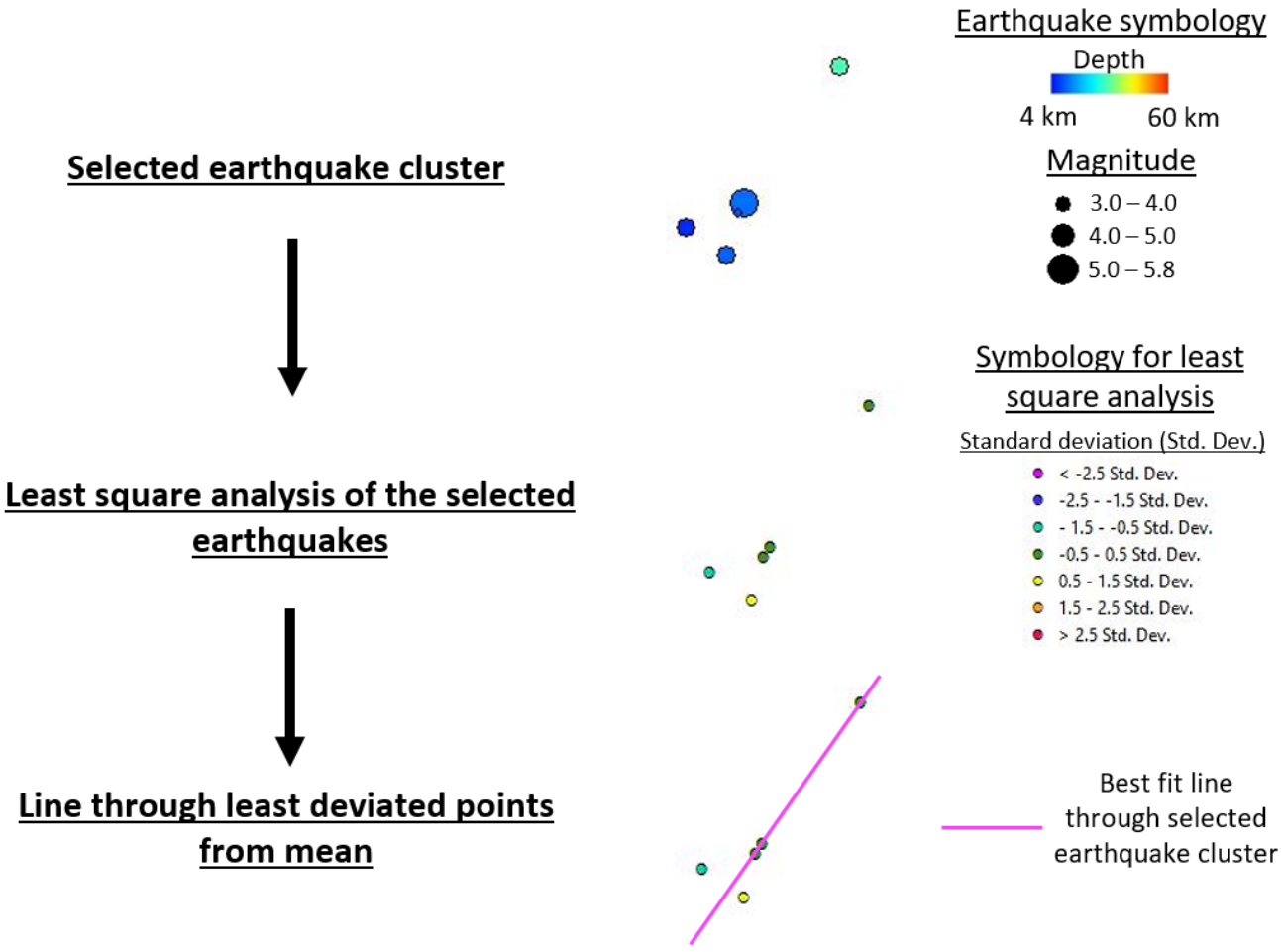

Figure 4.5: Workflow for determining a least square best fit line through a selected cluster of earthquakes. The location of the earthquake cluster is shown in Fig. 4.4 with a purple rectangle.

Chapter 5: Results

5.1 2D integrated modeling

5.1.1 Physical properties of modeled geological blocks

Density and magnetic susceptibility values of modeled blocks provide insight into the lithologies of different subsurface rocks (Table 5.1). Variations in these physical properties allow mapping different tectonic elements (e.g., accreted terrane, accretionary prism, etc.) within the Cascadia Subduction Zone (Fig. 5.1 and 5.2).

Table 5.1: Summary of the derived physical properties of subsurface rocks and seawater in the 2D integrated models

Model Blocks		**Density (g/cc)**		**Magnetic Susceptibility (cgs)**	
		Washington Model	Oregon Model	Washington Model	Oregon Model
Seawater		1.03	1.03	0.00	0.00
Undeformed oceanic sedimentary rocks on Juan de Fuca plate		1.90 – 2.40	2.10 – 2.40	0.00	0.00
Deformed oceanic sedimentary rocks in accretionary prism		2.45 – 2.75	2.45 – 2.75	0.00	0.00
Continental sedimentary basin		2.65	2.65	+0.003	0.00
Juan de Fuca oceanic crust		2.80 – 2.90	2.80 – 2.90	±0.002	±0.002
Siletz terrane	Upper	3.09	2.85	+0.005	+0.005
	Lower		3.085		+0.002
Cascadia arc		3.00	2.96	+0.002	+0.005
Mantle		3.30	3.30	0	0
Lower density zone in mantle (below the spreading center)		3.235	3.23	0	0

The top layer in both models is seawater with known physical properties (i.e., 1.03 g/cc density and zero magnetic susceptibility, Telford et al., 1990). The mantle also has a constant assumed density (i.e., 3.3 g/cc) and no magnetic susceptibility (i.e., 0 cgs) values for both models (Telford et al., 1990). However, a lower density of mantle rocks is required beneath the spreading centers in both models to comply with the observed gravity anomaly. From a geological standpoint, this zone is consistent with upwelling magma under the active seafloor spreading center. The density value of this zone is very similar in both models (Table 5.1). In the Washington model, this lower density mantle rock zone has 3.235 g/cc density and in the Oregon model, this zone needs a density value of 3.23 g/cc to satisfy gravity.

At the JdF spreading ridge, both in Washington (Fig. 5.1) and Oregon (Fig. 5.2) models, the derived crustal density is 2.8 g/cc and magnetic susceptibility is 0.002 cgs. In the Oregon model (Fig. 5.1), however, there is an active volcanic feature located at the spreading center which is called Axial Seamount (Chadwick et al., 2005). The seismic reflection profile of Han et al. (2016) (Fig. 3.4) provides a partial image of the magma chamber at the spreading center. Therefore, most of the geometry of the conical shaped oceanic block under the spreading ridge (i.e., also a part of Axial Seamount) has been determined by observing calculated gravity and magnetic response through the forward modeling. Since the physical properties of crustal rocks at the spreading center in both Washington and Oregon models are assumed to be the same, the derived crustal density (i.e., 2.8 g/cc) and magnetic susceptibility (i.e., 0.002 cgs) fit both observed potential field data at this location. This crustal density of the JdF oceanic crust

increases towards the subduction zone in both models. It reaches 2.9 g/cc under the Siletz terrane (Fig. 5.1 and 5.2). Gradual increment of this crustal density in the oceanic domain is geologically sound since JdF oceanic crust becomes older and denser as it heads over to the subduction zone (Carlson and Herrick, 1990). However, this increase of oceanic crustal density toward the coastline has few aberrations guided by the gravity data that requires several blocks of lower density with respect to surrounding crust in both Washington and Oregon models.

In the Washington model, a total of seven lower density oceanic crustal zones are interpreted (they are shown with grey and orange zones in Fig 5.1). In each case, the density values of these zones are lower than the immediately adjacent crustal blocks (numbered as 1, 2, 3..... in Fig. 5.1). For example, the first lower density zone—near the spreading ridge—has a density of 2.76 g/cc which is surrounded by crustal blocks with densities of 2.80 g/cc and 2.83 g/cc respectively. For all the lower density zones the density contrasts with the adjacent crustal blocks from 0.02 g/cc to 0.04 g/cc.

In the Oregon model, the first lower density zone is interpreted about 78 km west of the JdF spreading ridge. To satisfy observed gravity data, this zone requires a density value of 2.76 g/cc which is lower than the surrounding oceanic crust density (i.e., 2.80 g/cc). There are a total of five lower density crustal blocks in the Oregon model showing 0.03 g/cc to 0.06 g/cc lower density than the surrounding crust (numbered as 8, 9, 10..... in Fig. 5.2).

Unlike the density value, the magnetic susceptibility of the rocks in the JdF slab has been made constant (i.e., 0.002 cgs) throughout the oceanic crust to maintain the geological validity of the integrated model. Because of the magnetic reversals in the oceanic crust, corresponding positive or negative signs have been assigned with the magnetic susceptibility values.

The density of the undeformed sedimentary sections in the Pacific Ocean on the top of the JdF oceanic plate ranges from 1.90 g/cc to 2.40 g/cc (corresponds to the P-wave velocity of 2.5 - 5 km/s) in both models. Assuming a general compaction trend for these sediments, guided by P-wave velocity values from seismic refraction experiments, the density for the shallowest layer has been estimated as 1.90 g/cc. These sedimentary layers get denser with depth. On top of the non-subducting part of the oceanic crust, away from the deformation front, the Oregon model has a very thin layer of nonmagnetic sediments with a density of 2.1 g/cc. Toward the accretionary prism, the density of the undeformed sedimentary section becomes 2.4 g/cc because of the increasing tectonic force associated with subduction. In the accretionary prism, the density values have a range from 2.45 g/cc for the shallowest layer to 2.75 g/cc for the deepest layer which is required for matching the observed gravity data. This high density value (i.e., 2.75 g/cc) for the deepest sedimentary layer is related to metamorphic changes at 10 to 15 km depth within the accretionary prism (Hyndman, 1988; Lewis et al., 1988; Nedimović et al., 2003). This density range is true for both the Washington and Oregon models. However, on top of the accretionary prism, close to

the shoreline, the Washington model has a very thin sediment layer with a very low density (i.e., 1.90 g/cc) of unconsolidated oceanic sediments.

The sedimentary section over the Siletz terrane in the Washington model has a density of 2.65 g/cc and magnetic susceptibility of 0.003 cgs. Because of the presence of volcaniclastic rocks associated with the active volcanic arc to the east, a small magnetic anomaly is expected in the continental sedimentary section in Washington. The Siletz terrane in this model has a density of 3.09 g/cc with a magnetic susceptibility value of 0.005 cgs. These high values are required to fit observed potential fields and are consistent with lithology of the accreted terrane (Parsons et al., 1999; Phillips et al., 2017) and observed P-wave velocities from seismic refraction data (i.e., 6 to 7 km/s) (Fig. 3.5; Parsons et al., 2006). The Cascadia arc area of the Washington line is modeled with a density of 3.00 g/cc and magnetic susceptibility of 0.002 cgs. Based on the seismic velocity values from Gerdom et al. (2000), shown in Fig. 3.6 b, the Siletz terrane in the Oregon model has been divided into shallower Upper Siletz Terrane (2.85 g/cc and 0.005 cgs) and deeper Lower Siletz Terrane (3.085 g/cc and 0.002 cgs). The Cascadia arc region just east of the Siletz terrane in the Oregon model requires a density of 2.96 g/cc and magnetic susceptibility of 0.005 cgs to explain observed potential fields.

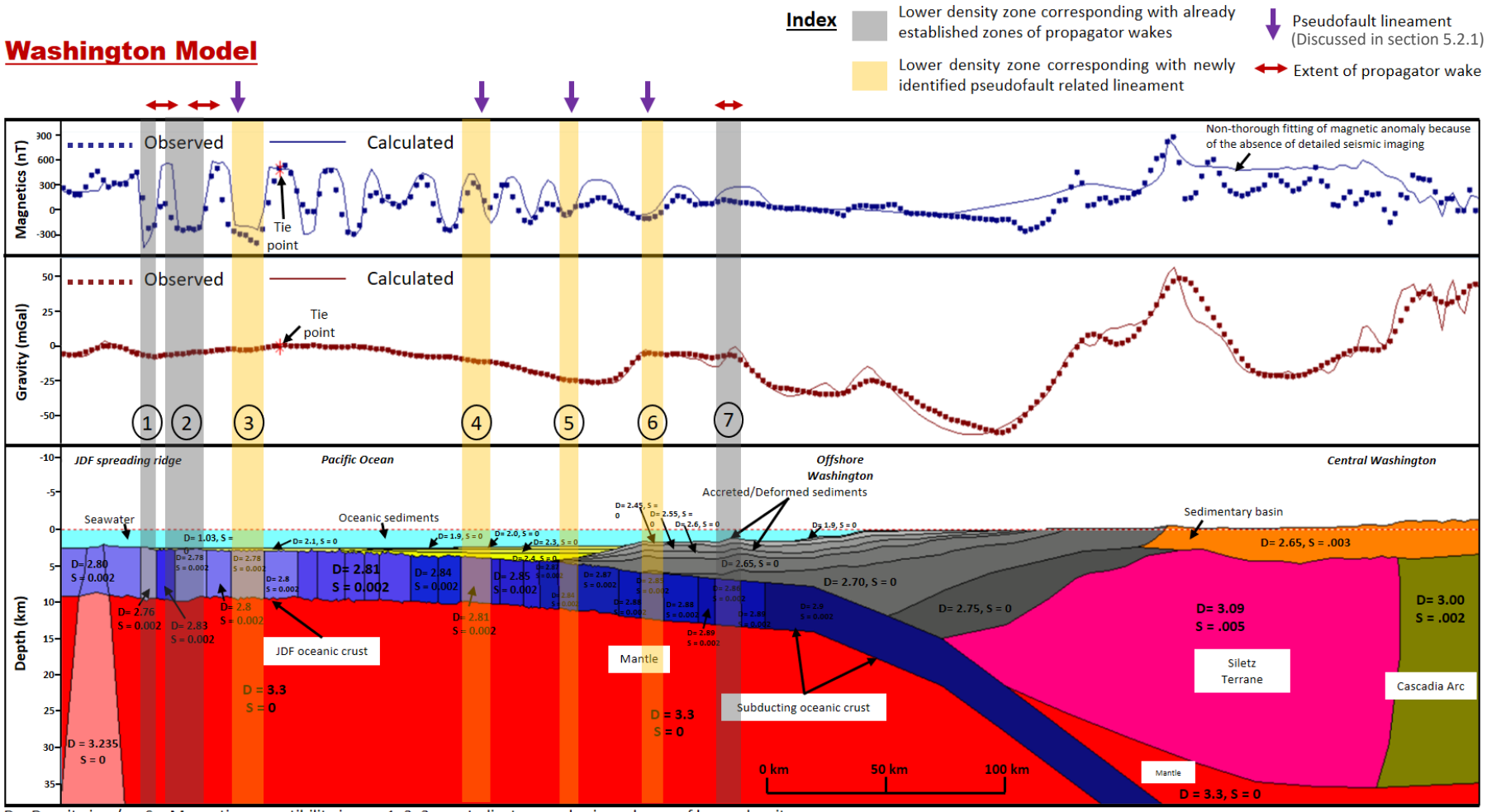

Figure 5.1: Integrated geophysical model in the northern part of the study area (Washington model). See location in Fig. 1.1. Please see section 5.2.1 for the spatial correlation between interpreted lower density zones (i.e., mapping of Pseudofault Lineaments).

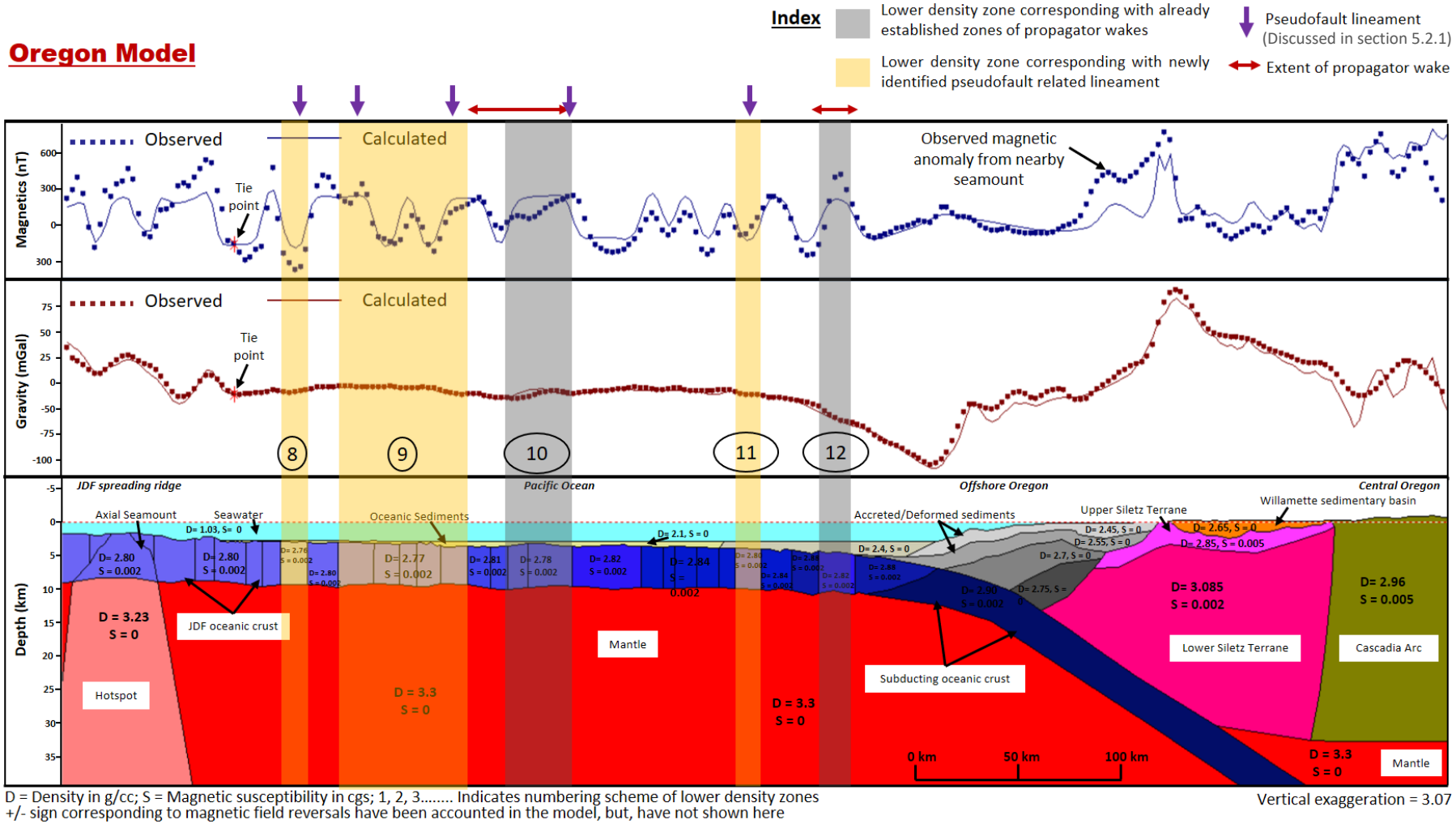

Figure 5.2: Integrated geophysical model for the southern transect (Oregon model). See location in Fig. 1.1. Please see section 5.2.1 for the spatial correlation between interpreted lower density zones (i.e., mapping of Pseudofault Lineaments).

5.1.2 Crustal Architecture in Washington model

The crustal architecture of this study area was constrained by both seismic reflection (Han et al., 2017) and seismic refraction data (Parsons et al., 2006). In the Washington model, the thickness of the JdF crust ranges between 6.5 km to 6.9 km. Only the oceanic spreading center requires a thinner crust (i.e., ~6 km) to fit observed gravity and magnetic anomaly. Although the density is similar for zones of low-density upwelling mantle rocks between the Oregon and Washington models, the spatial extent is different. In the Washington model, this lower density mantle zone starts beneath the oceanic Moho with a width of about 13 km; at 90 km of depth, the width of this zone reaches up to about 55 km. In contrast, this lower density mantle zone in the Oregon model has a width of about 40 km close to the oceanic Moho, while at 90 km depth the width of this zone increases up to 110 km. Therefore, the zone of the upwelling mantle rocks is much narrower in the Washington model, which relates to the presence of the Cobb hotspot in the Oregon model (Fig 1.1.).

Under the accretionary prism, the JdF crust dips at an angle of 7^{o} in the Washington model. This dipping angle reaches 14^{o} when the oceanic crust meets the Siletz terrane in the continental portion of the model. About 165 km of JdF oceanic crust is dragging itself beneath the accretionary prism near southern Washington. The length of the portion of the JdF crust that is in contact with the overlying Siletz terrane is about 28 km.

In the Washington model, the sedimentary deposits are much thicker than the Oregon model. Close to the accretionary prism, approximately 3 km of sediments can be observed in the oceanic domain. Further east at the subduction zone, the sedimentary thickness increases to 15 km. The width of these piled up accreted sediments in the Washington model is approximately 215 km. On the continental domain, the Siletz terrane is about 32 km thick and 192 km wide, which is 87 km wider than the Siletz terrane of the Oregon model. The continental Moho beneath the Siletz terrane is located at a depth of 35.5 km in the Washington model.

5.1.3 Crustal Architecture in Oregon model

The thickness of the JdF oceanic crust ranges from 6.0 km to 6.5 km in the Oregon model. Similar to the Washington model, most of the geometry of the conical shaped oceanic block under the spreading ridge has been developed from gravity and magnetic data because the seismic image from Han et al., 2015 provides a very limited reflection of the magma chamber. As already been mentioned, one notable difference between the spreading center geometries in Oregon and Washington models Is the presence of Axial seamount in the Oregon model. Because of this, the oceanic crustal block at the spreading center of the Oregon model is much wider than the one in the Washington model.

The dipping portion of the subducting oceanic slab in the Oregon model is very similar to the one of the Washington model. Under the accretionary prism, the dip of oceanic crust is 6^{o}, however, when it reaches the Siletz terrane over the continental domain, the

JdF oceanic slab subducts at about 13^{o}. In this region, a 67 km wide segment of the subducting JdF crust is in frictional condition with the accretionary prism. Beneath the Siletz terrane, about 88 km of JdF crust is in contact with it.

The sedimentary section in the accretionary prism is up to 13 km thick. The width of this accretionary prism in the Oregon model is approximately 105 km. The continental Willamette sedimentary basin, on top of the Siletz terrane, is about 3 km thick (Table 4.2). The entire Siletz Terrane in the Oregon model has a maximum thickness of 32 km while the deepest point of continental Moho beneath the terrane is at a depth of 33 km. In terms of extent, this terrane has a maximum width of 140 km.

5.1.4 Forward gravity modeling of propagator wake zones

As described in section 2.4.3, the gravity modeling of Marjanović et al. (2011) suggests that propagator wakes are associated with thinner and denser crust. However, in the developed 2D plate-scale models of this study (Fig. 5.1 and 5.2), the propagator wakes seem to correlate with lower density zones (i.e., grey shaded areas in Fig. 5.1 and 5.2). To overcome this contention, gravity models for the Marjanović et al., (2011) lines (Fig.2.6) on the JdF plate have been reconstructed with our gravity data (Fig. 3.1). The Endeavor gravity model from Marjanović et al., (2011) (Fig. 2.6a) already coincides with the Washington model of this study (Fig. 5.1). Therefore, only two other models, namely the Northern Symmetric and Cleft models from Fig. 2.6b and 2.6c (see Figs. 1.1 and 5.3 for their geographic positions), have been tested with the forward gravity modeling (see

the modeling work workflow in Fig. 4.2). In order to avoid the edge effect, the gravity models have been extended beyond the region constrained with seismic reflection (Fig. 5.4 and 5.5). For each of the developed gravity models, at first, the densities of different modeled blocks are assigned exactly the same as the density values from Marjanović et al. (2011). Please note the unrealistically low densities of the basaltic layer (1.9 to 2.4 g/cc, Fig. 5.4a).

Fig. 5.4 shows the gravity model across the Cleft spreading ridge segment (Fig. 1.1). At the western end of the Cleft model, it crosses the propagator wake 'iii' (Fig. 1.1). After assigning the gravity values from Marjanović et al. (2011), several apparent mismatches were observed (Fig 5.4a). Their highest density crustal block with a density of 2.83 g/cc is generating a higher calculated gravity response than the observed one. Moreover, according to our analysis, the block with 2.83 g/cc crustal density sits outside of the propagator wake zone (compare Figs. 5.4a and 5.4b). There is also another significant out of phase mismatch between observed and calculated free air gravity anomalies within the constrained model (Fig. 5.4a).

After observing the match between observed and calculated free-air gravity responses, densities were adjusted to improve the fit (Fig. 5.4b). First of all, density values for the basaltic layer have been changed from ones of Marjanović et al. (2011) to be consistent with the models shown in Figs. 5.1 and 5.2. In the revised Cleft model (Fig. 5.4b), densities of the basaltic layer range from 2.65 g/cc to 2.66 g/cc which is in agreement with the global average (Carlson and Herrick, 1990). The densities of the deeper or gabbroic oceanic crust have also been redistributed to reflect the general age-related

increase in the density of oceanic crust toward the subduction zone. At the spreading center, the gabbroic oceanic crust has a density of 2.8 g/cc, while at the eastern end of the model it reaches 2.84 g/cc. Within the constrained region of the Cleft model (Fig. 5.4b), two lower density zones have been identified through our gravity modeling. In this study, these two zones have been named as eastern and western lower density zone of the Cleft model (Fig 5.4b). In the middle of the western low-density zone, the model requires crustal blocks with a very low density value (i.e., 2.72 g/cc) which is 0.9 g/cc lower than the normal oceanic crustal density in that area (i.e., 2.8 g/cc). The density of this zone is 0.4 g/cc lower than the surrounding oceanic crustal density (i.e., 2.83 g/cc). Crustal blocks at the periphery of the propagator wake 'iii' have normal oceanic crustal density (i.e., it matches with the general increasing trend of oceanic crustal density). However, observed gravity suggests an apparent higher density for the oceanic crustal blocks at the western edge of the propagator wake 'iii'. This apparent free-air gravity high is the basis of the hypothesis proposed by Marjanović et al. (2011) that states propagator wakes represent higher density crust with the oceanic plate. However, this apparent gravity high relates to the bathymetric seamount located nearby the modeling line (see location in Figure 5.3), so the 3D gravity effect of this seamount must be taken into account. In essence, our hypothesis regarding propagator wakes are zones with lower density than the surrounding crust is supported by the revised Cleft model.

The gravity model over the Northern Symmetric spreading segment of the JdF ridge system is shown in Fig. 5.5. The seismic reflection data from cruise EW0207 (Carbotte et

al., 2002) used by Marjanović et al., (2011) to constrain the Northern Symmetric model (Fig. 2.6b) crosses the propagator wake 'iii' twice (see location in Figs 1.1 and 5.3). Marjanović et al. (2011) developed two different models for two zones of the same propagator wake (Fig. 2.6b). In this study's forward gravity modeling, those two models are combined into one (Fig 5.5).

The developed Northern Symmetric model of this study (Fig. 5.5b) has a density distribution that is consistent with plate scale 2D models (Fig 5.1 & 5.2) and also the Cleft model (Fig 5.4b). For the sedimentary section, one deeper layer (i.e., with 2.2 g/cc density) has been introduced in the Northern Symmetric model because of the presence of ~ 0.5 km thicker sediments. However, the basaltic layer density is similar to the Cleft model (i.e., 2.65 - 2.66 g/cc). The density of gabbroic oceanic crust (i.e., 2.8 - 2.86 g/cc) is also consistent with all the plate-scale models in this study (Fig. 5.1 and 5.2).

Similar to the Cleft model (Fig 5.4b), the Northern Symmetric model also requires lower density zones within the oceanic crust. There are three lower density zones namely western, middle and eastern lower density zones in the Northern Symmetric model (Fig. 5.5b). The middle (i.e., with 2.8 g/cc density) and eastern (i.e., with 2.82 g/cc density) lower density zones coincide with the two segments of propagator wake 'ii' on the JdF plate (Figs 1.1 and 5.3). According to the gravity modeling of Marjanović et al. (2011), the density of the middle zone in the Northern Symmetric model (Fig 5.5a) is 2.9 g/cc. However, this density value does not provide the best fit in our forward modeling. The eastern lower density zone (Fig 5.5b) requires 2.82 g/cc density, which is 0.02 g/cc lower than the surrounding crust and coincides with part of the eastern segment of

propagator wake 'ii' on the JdF plate (Fig. 5.3 and 5.5b). However, this eastern lower density zone can also be correlated with one of the higher density zone (i.e., with 2.91 g/cc density) proposed by Marjanović et al., (2011) (Fig. 5.5). Our forward gravity modeling also suggests higher density for this zone to achieve the best fit matching with the observed gravity data. Nonetheless, spatial analysis around the Northern Symmetric modeling line suggests that higher observed gravity reading in this zone is generated from two nearby seamounts which are mapped from seismic reflection line 03 from cruise RC1501 (Fig. 3.3b). As these two nearby seamounts are masking the observed gravity anomaly, we favor the presence of normal oceanic crust (i.e., with 2.84 g/cc density) in this zone.

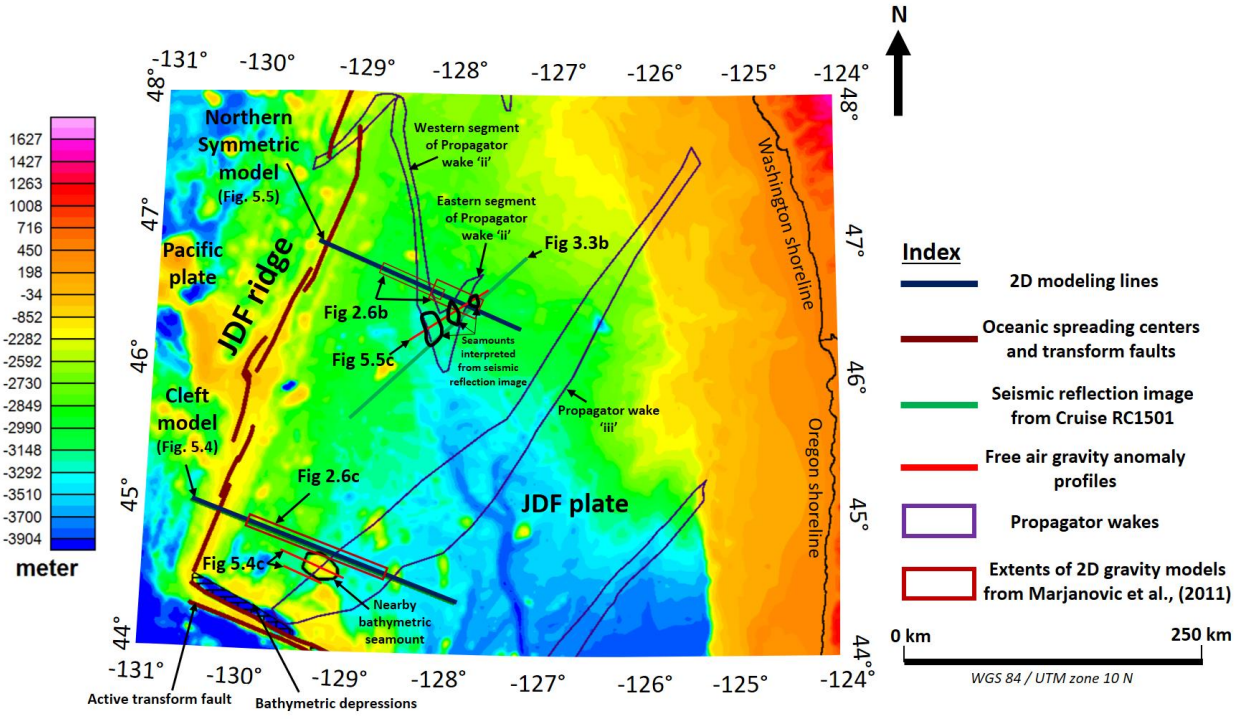

Figure 5.3: Bathymetry map with the modeled gravity lines of this study and also from Marjanović et al., (2011). Seamounts that are affecting the observed gravity data of the modeling lines (Fig. 5.4c and 5.5c) are outlined.

a)

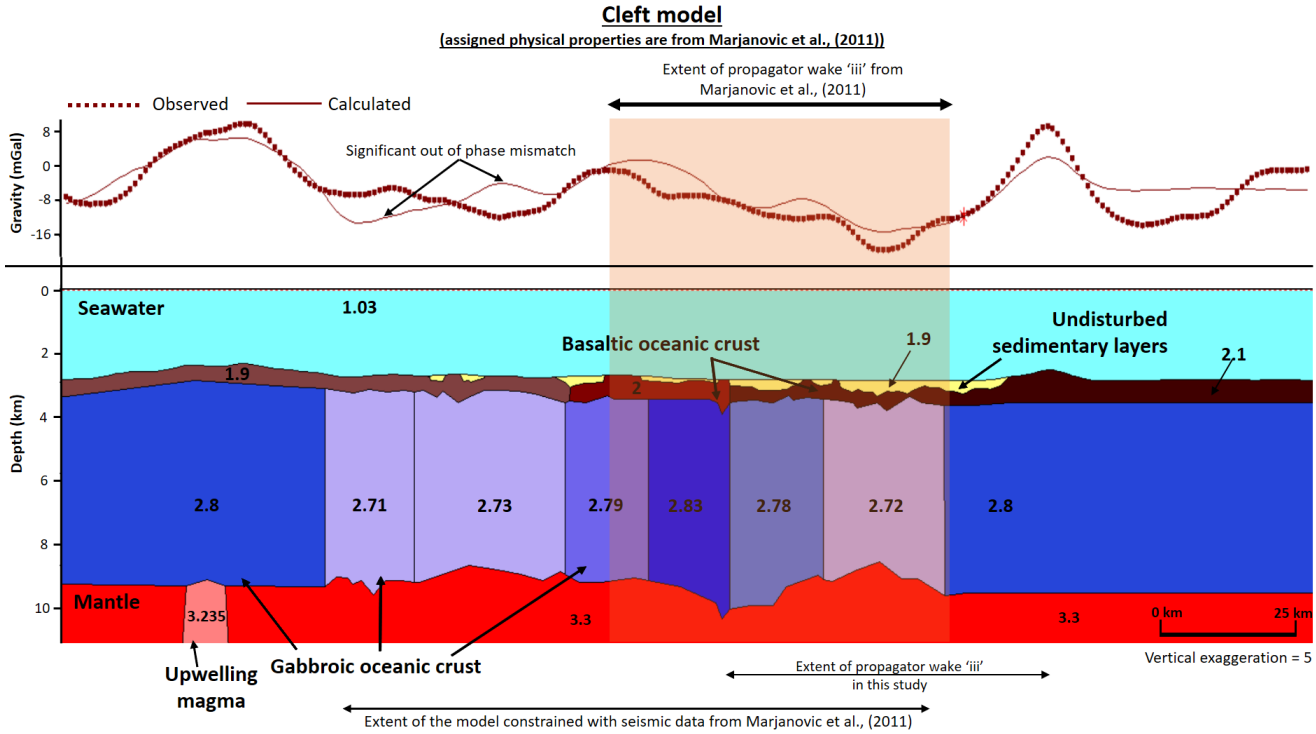
Cleft model
(assigned physical properties are from Marjanovic et al., (2011))
Extent of propagator wake 'iii' from Marjanovic et al., (2011)
Observed
Calculated
Significant out of phase mismatch
Gravity (mGal)
Depth (km)
Seawater
1.03
Basaltic oceanic crust
Undisturbed sedimentary layers
2.1
1.9
2.8
2.71
2.73
2.79
2.83
2.78
2.72
Mantle
3.235
3.3
0 km
25 km
Vertical exaggeration = 5
Upwelling magma
Gabbroic oceanic crust
Extent of propagator wake 'iii' in this study
Extent of the model constrained with seismic data from Marjanovic et al., (2011)

b)

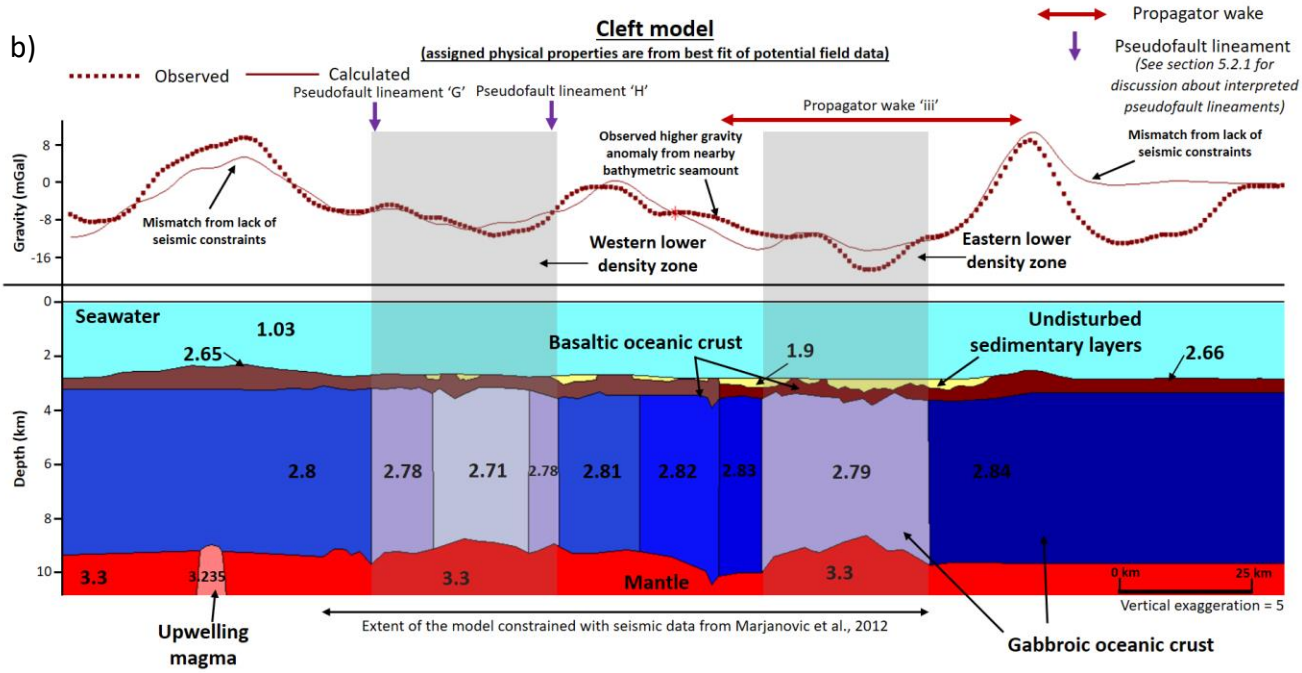
Cleft model
(assigned physical properties are from best fit of potential field data)
Propagator wake
Pseudofault lineament
(See section 5.2.1 for discussion about interpreted pseudofault lineaments)
Observed
Calculated
Pseudofault lineament 'G'
Pseudofault lineament 'H'
Propagator wake 'iii'
Mismatch from lack of seismic constraints
Observed higher gravity anomaly from nearby bathymetric seamount
Western lower density zone
Eastern lower density zone
Gravity (mGal)
Depth (km)
Seawater
1.03
2.65
Basaltic oceanic crust
1.9
Undisturbed sedimentary layers
2.66
2.8
2.78
2.71
2.81
2.82
2.79
2.84
Mantle
3.3
3.235
0 km
25 km
Vertical exaggeration = 5
Upwelling magma
Extent of the model constrained with seismic data from Marjanovic et al., 2012
Gabbroic oceanic crust

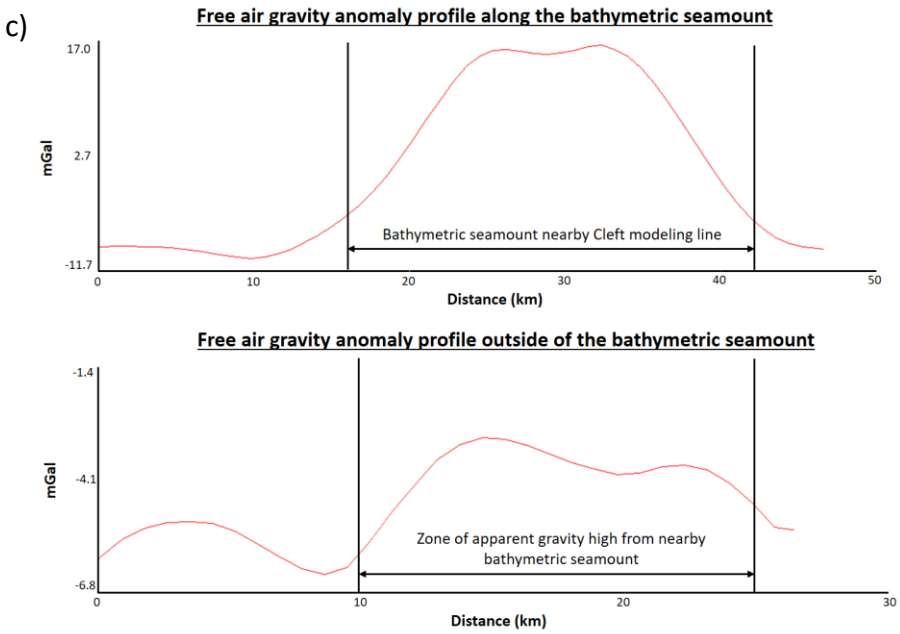

Figure 5.4: Cleft model a) properties are from Marjanovic b) properties are assigned based on modeling in this study. c) Two free air gravity anomaly profiles across and near the bathymetric seamount which is affecting the observed gravity of the Cleft model (b).

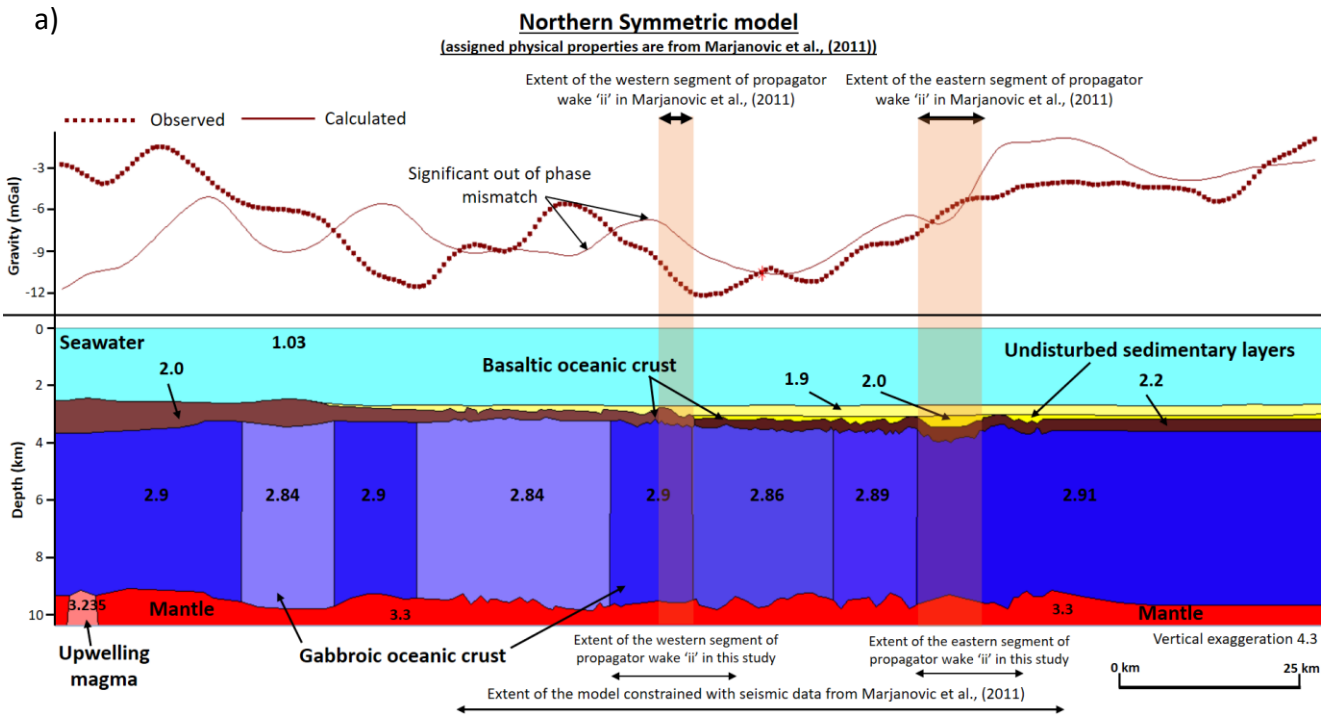

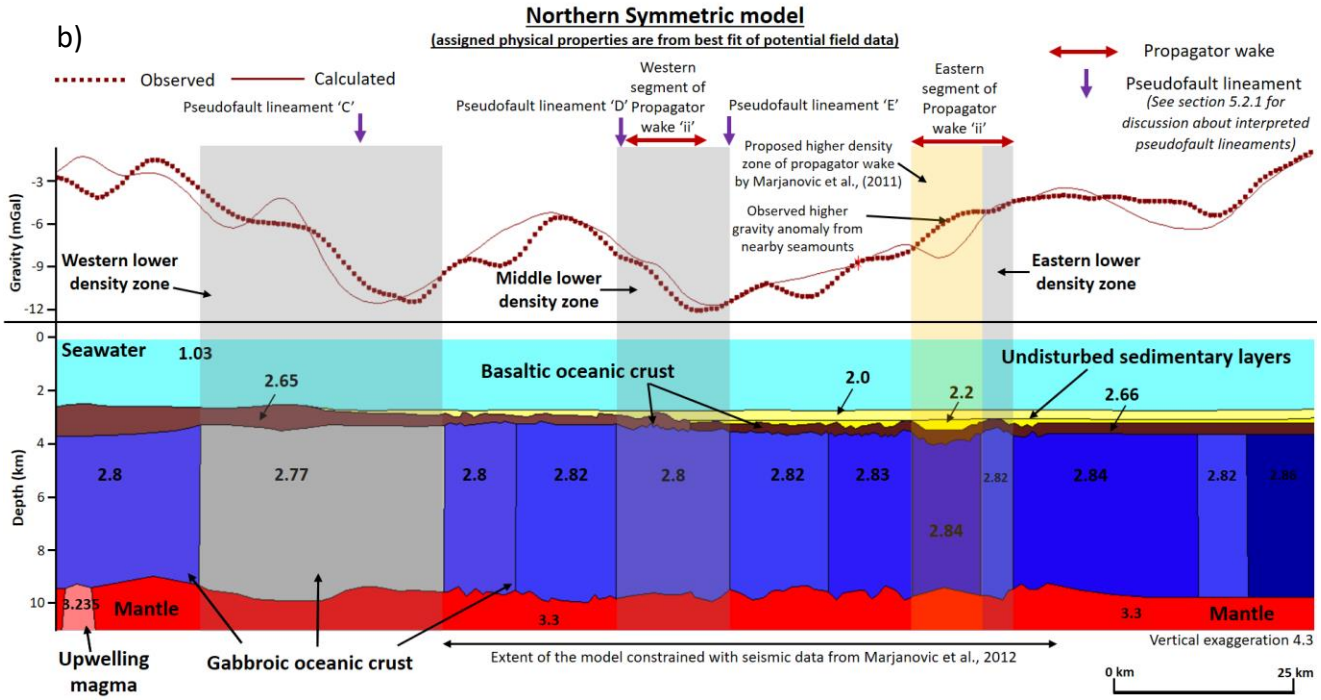

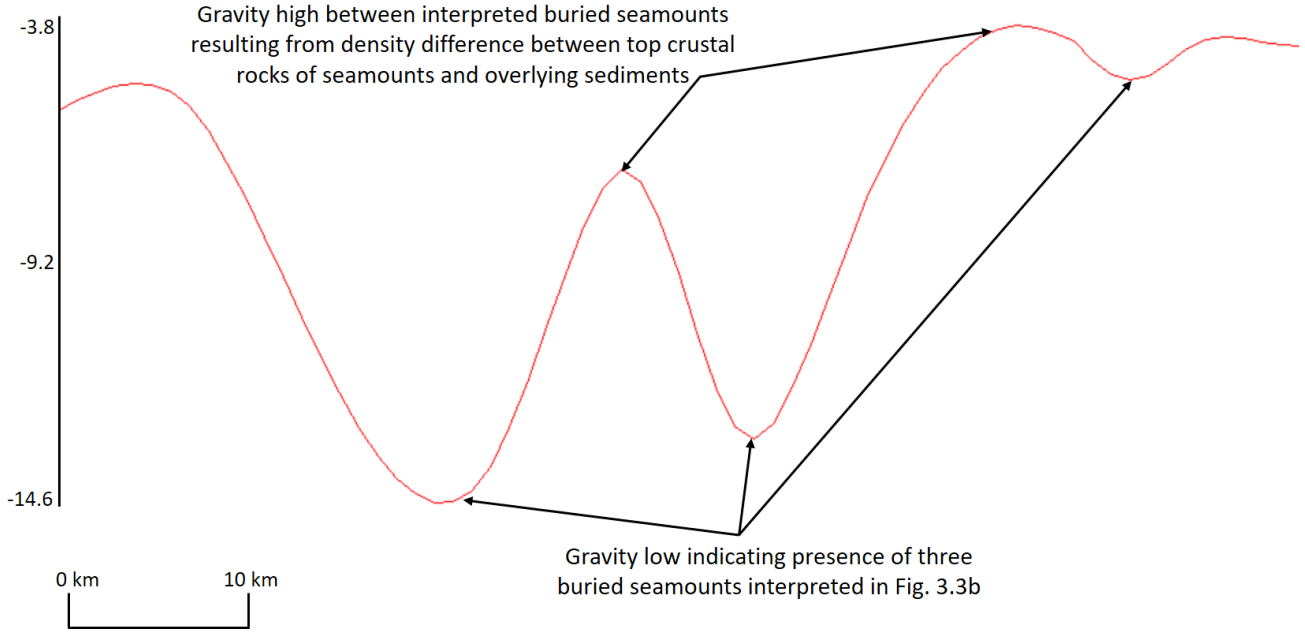

Figure 5.5: Northern Symmetric model a) properties are from Marjanovic b) properties are assigned based on our modeling c) Free air gravity anomaly profile across the buried seamounts interpreted in Fig. 3.3b which are affecting the observed gravity of the Northern Symmetric model (b).

5.2 Integrated spatial analysis

The workflow for executing spatial analysis is shown in Fig. 4.1. The primary objective is to utilize potential fields (i.e., gravity and magnetic) to extrapolate the structures interpreted from 2D models in order to map key tectonic features on the entite JdF plate. By clearly studying the tectonic or geological features of the non-subducting part of the JdF plate, I hope to estimate the structural and compositional variations of the subducted JdF oceanic crust. Understanding the geology and structures of the subducted slab is essential to comprehend the generated seismicity patterns in the subduction zone.

5.2.1 Mapping of pseudofault lineaments

This section discusses mapping a newly identified lineament type from magnetic data. The primary criterion of mapping these lineaments is following discontinuities in the sea-floor magnetic stripes. While propagator wakes are mapped from large-scale offsets in sea-floor magnetic stripes, these newly identified lineaments are associated with shorter offsets and smaller disturbances. In this study, these newly identified lineaments are referred to as pseudofault (PSF) lineaments, while the previously established ones as propagator wakes. Figs. 5.6 and 5.7 illustrate how disturbances and offsets in sea-floor magnetic stripes combined with constraints from 2D modeling (i.e., white bars in Figs. 5.6 and 5.7) lead to mapping of these PSF lineaments respectively in the northern and southern part of the JdF plate. The types of disturbances in sea floor magnetic stripes that were considered during picking up these lineaments are gaps in the stripes, change in the stripe orientation from ~North-South to ~East-West, and considerable reduction

of the stripe's width. Several types of filters applied to residual magnetic anomaly also helped to highlight these lineaments. However, only the tilt derivative maps are shown in this thesis (Fig. 5.6b and 5.7b) where the PSF lineaments are most apparent.

In this thesis, the mapped PSF lineaments are hypothesized to be triggered from the offsets between the JdF spreading ridge segments. The details regarding the origin of PSF lineaments are further discussed in section 6.3.

The following assumptions were utilized in interpreting the pseudofault lineaments:

- The western end of a picked-up pseudofault lineament should originate at the offset between two adjacent spreading ridge segments. The breaks in spreading ridges may be related to differences in the spreading rate, variations in magmatic supply or result from the accommodation of shear stress. No matter what the leading process responsible for initiating the PSF lineaments is, they should originate at those offsets. In some cases, they can also originate at the edges of a transform fault (Fig 5.7).
- The interpreted lineaments should cross the zones of lower densities determined during 2D modeling (shown as white bars in Figs. 5.6 and 5.7). This is because the lineaments are interpreted to trace the zones of crustal weakness (see section 6.3 for details).
- Interpreted pseudofault lineaments are aligned with the subduction direction of the JdF plate which is again in agreement with their inferred origin mentioned above.

- Interpreted pseudofault lineaments should not cross one another.
- These newly interpreted tectonic structures are interpreted as line features. In reality, they represent zones with a certain width (i.e., smaller than the width of propagator wakes). However, the data used in this study do not have the resolution to map them as zones, so they have been approximated as line features.

a)

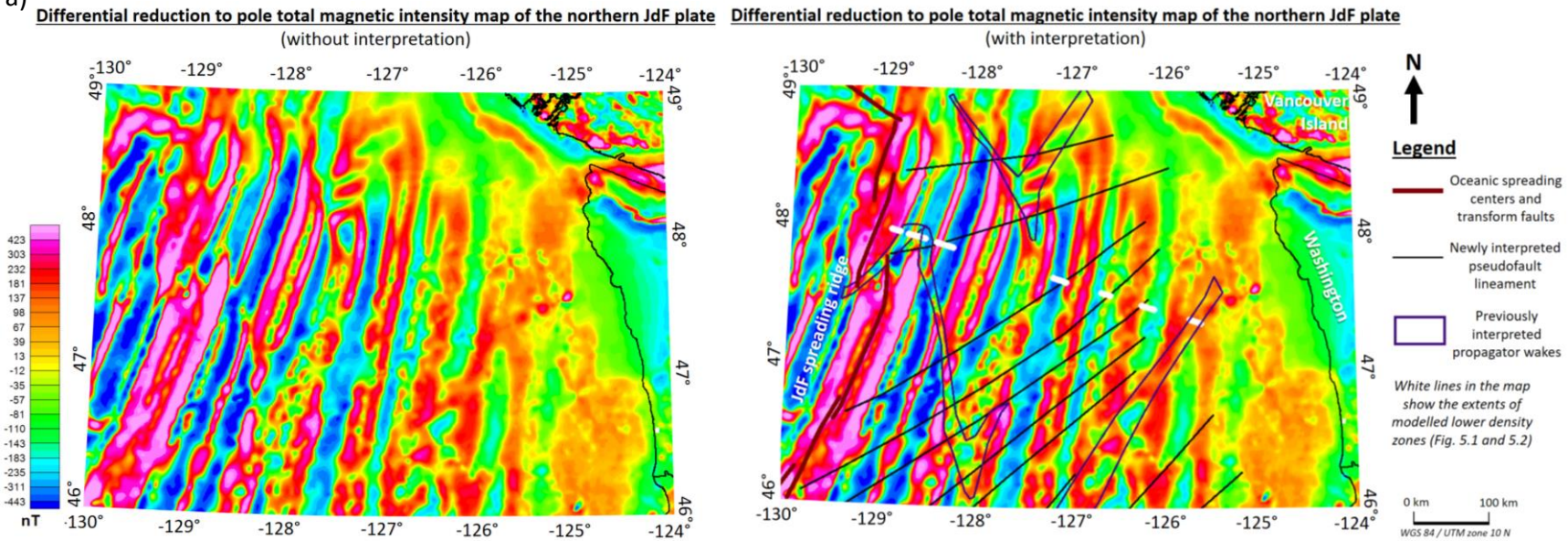
Differential reduction to pole total magnetic intensity map of the northern JdF plate
(without interpretation)
Differential reduction to pole total magnetic intensity map of the northern JdF plate
(with interpretation)
-130°
-129°
-128°
-127°
-126°
-125°
-124°
49°
48°
47°
46°
423
303
232
181
137
98
67
39
13
-12
-35
-57
-81
-110
-143
-183
-235
-311
-443
nT
Vancouver Island
JdF spreading ridge
Washington
N
Legend
Oceanic spreading centers and transform faults
Newly interpreted pseudofault lineament
Previously interpreted propagator wakes
White lines in the map show the extents of modelled lower density zones (Fig. 5.1 and 5.2)
0 km
100 km
WGS 84 / UTM zone 10 N

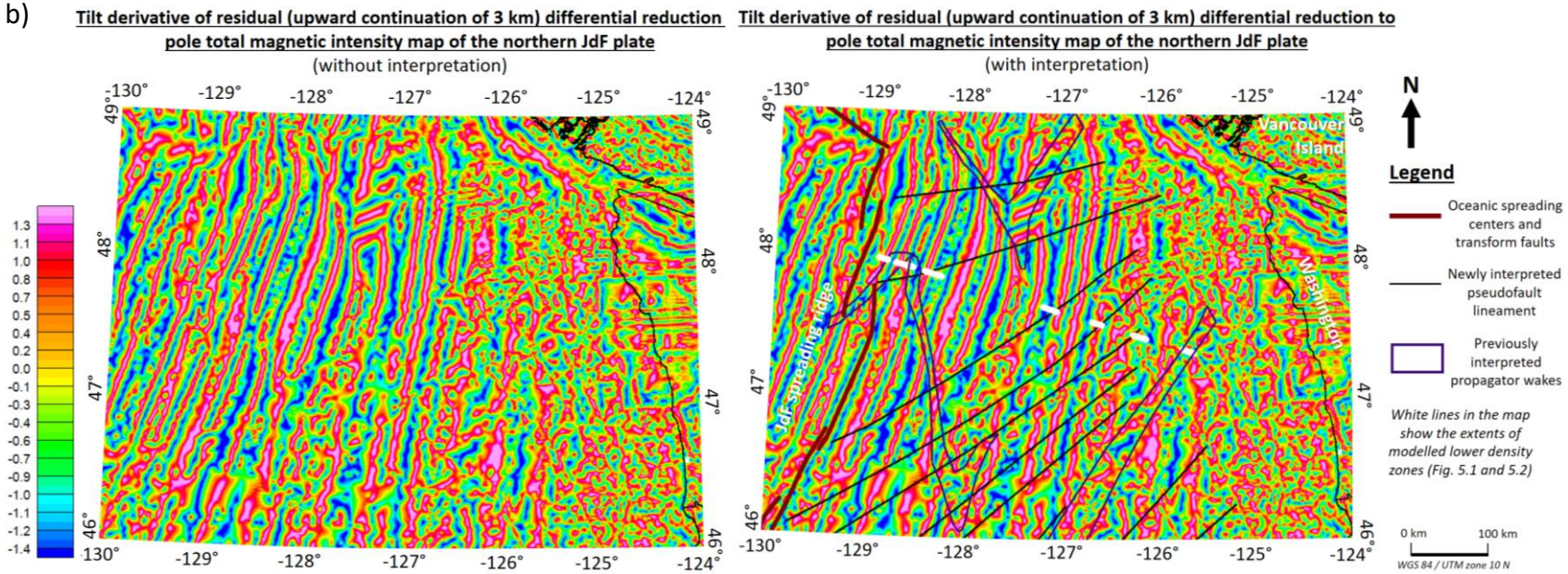

Figure 5.6: Interpretation of pseudofault lineaments in Northern JdF plate from disturbances of sea-floor magnetic stripes. Figures show newly interpreted pseudofault lineaments in the differential reduction to pole total magnetic intensity map (a) and in its residual tilt derivative (b). The modeled lower density zones are from plate-scale integrated 2D models through Washington (Fig. 5.1) and Oregon (Fig. 5.2).

a)

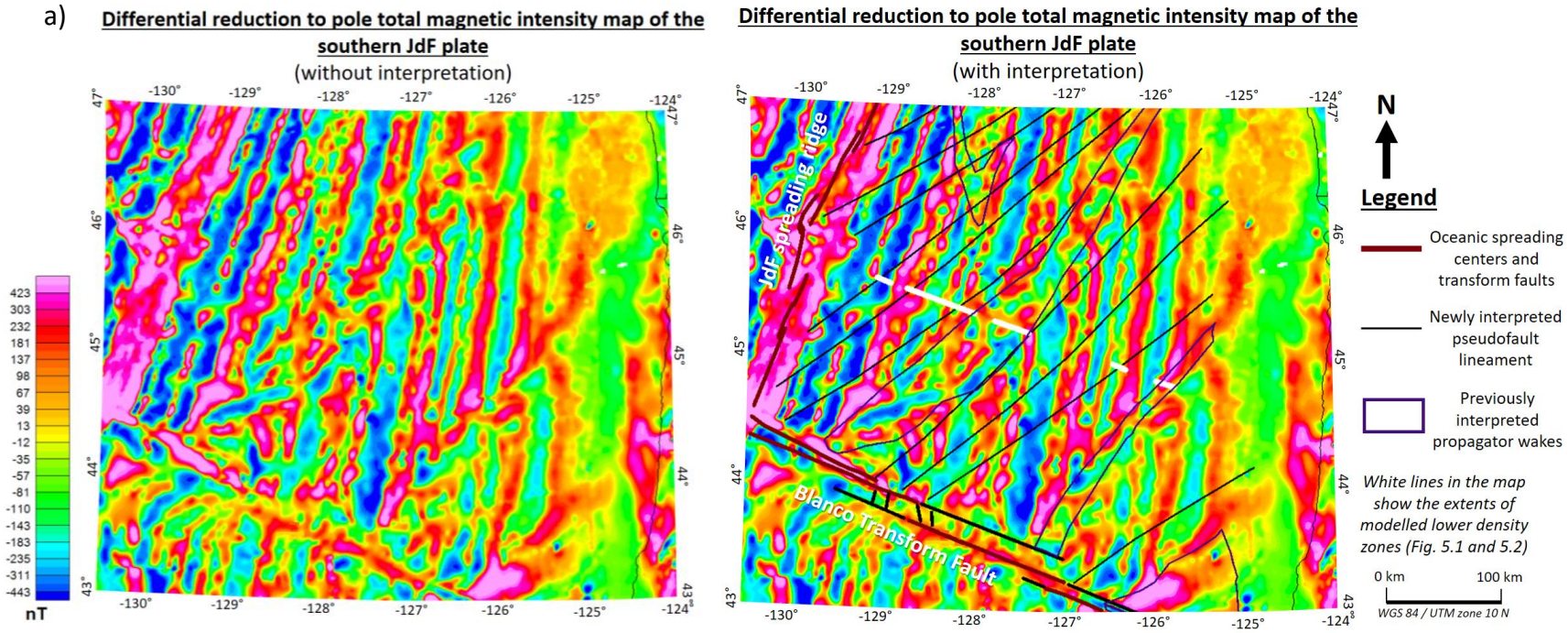
Differential reduction to pole total magnetic intensity map of the southern JdF plate
(without interpretation)
Differential reduction to pole total magnetic intensity map of the southern JdF plate
(with interpretation)
423
303
232
181
137
98
67
39
13
-12
-35
-57
-81
-110
-143
-183
-235
-311
-443
nT
-130°
-129°
-128°
-127°
-126°
-125°
-124°
47°
46°
45°
44°
43°
JdF spreading ridge
Blanco Transform Fault
N
Legend
Oceanic spreading centers and transform faults
Newly interpreted pseudofault lineament
Previously interpreted propagator wakes
White lines in the map show the extents of modelled lower density zones (Fig. 5.1 and 5.2)
0 km
100 km
WGS 84 / UTM zone 10 N

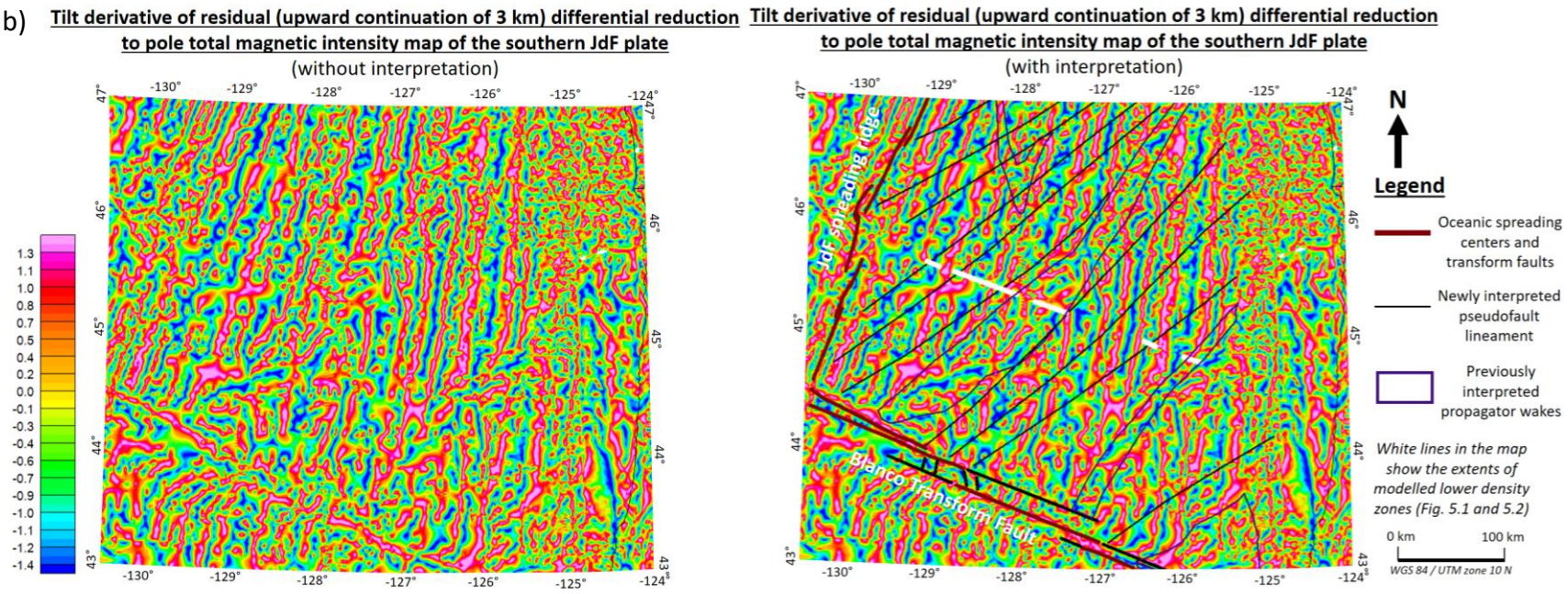

Figure 5.7: Interpretation of PSF lineaments in Southern JdF plate from disturbances of sea-floor magnetic stripes. Figures show newly interpreted PSF lineaments in the differential reduction to pole total magnetic intensity map (a) and in its residual tilt derivative (b). The modeled lower density zones are from plate-scale integrated 2D models through Washington (Fig. 5.1) and Oregon (Fig. 5.2).

For effective categorization, each newly identified PSF lineament is named with a letter from A to L starting from the north (Fig. 5.8). Previously interpreted propagator wakes are categorized with roman numerals with the most northern one numbered as 'i' to the 'vi' for the most southern one (Fig. 5.8). Two of the interpreted lineaments do not cross the plate scale models (i.e.., PSF lineament 'A', 'J') and one of the lineament crosses the Oregon model, but, cannot be correlated with any modeled lower density zones (i.e., PSF lineament 'L'). Interpretation of these lineaments is categorized with medium confidence. Overall, obliquity to the E-W direction of these lineaments decreases northward. The trend of these lineaments changes from ~ N60°E in the southern JdF plate to ~ N80°E in the northern JdF plate (Fig. 5.8).

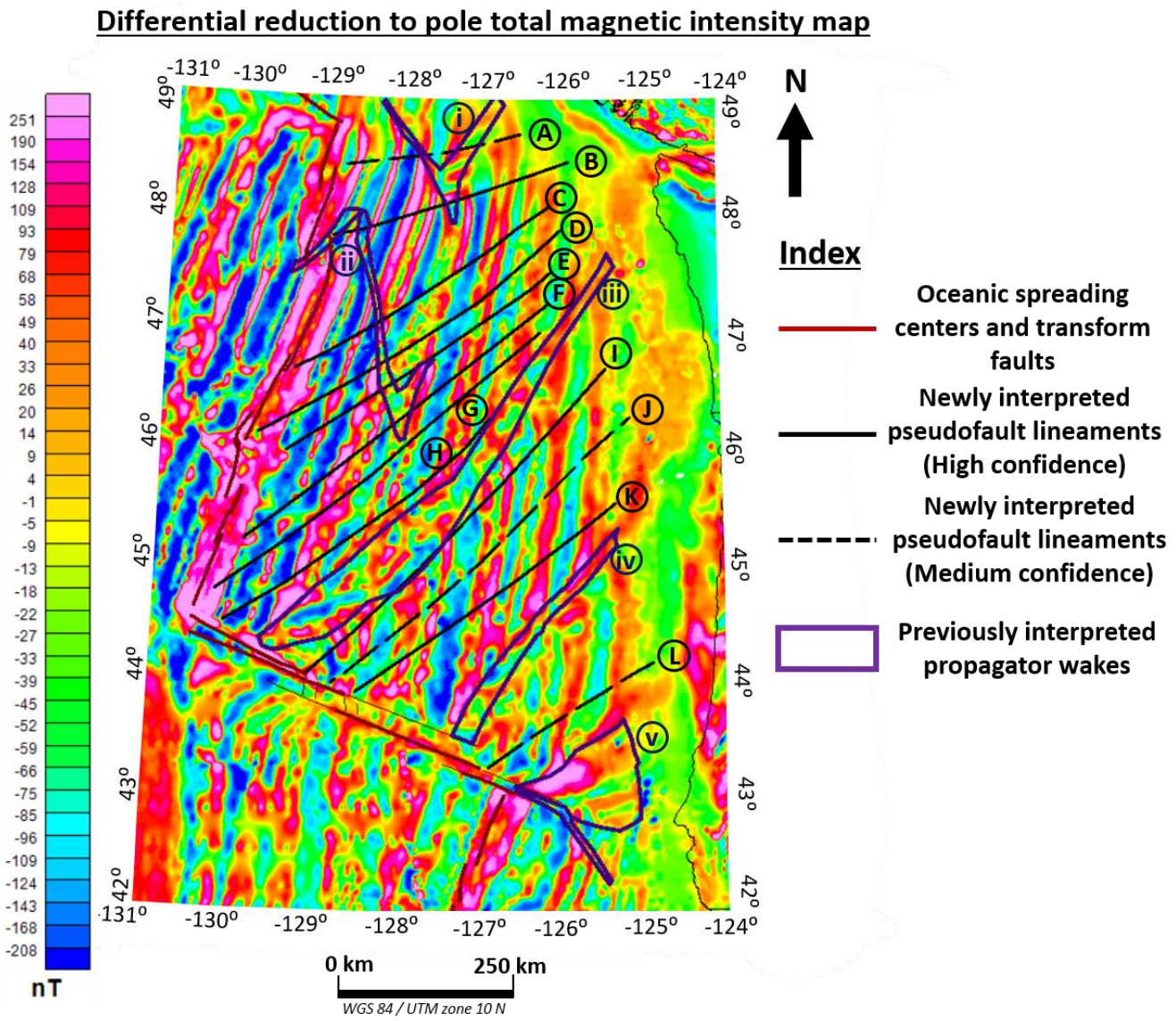

Figure 5.8: All of the newly mapped PSF lineaments and previously interpreted propagator wakes on the JdF plate. A, B, C…… show the numbers of the mapped PSF lineaments. i, ii, iii….. represent the numbering scheme of the propagator wakes.

5.2.2 Correlation of mapped lineaments and low-density crustal zones

To investigate the identified low-density zones (i.e., grey and orange shaded regions in Fig. 5.1 and 5.2) further, the residual Bouguer gravity (detrended values from Fig. 3.1b) and crustal thickness from seismic data were analyzed (Fig. 5.9). The former illustrates the correlation between identified lower density regions and observed gravity lows, while the latter shows the crustal architectures (the top and bottom of the oceanic crust) within the modeled lower density zones. The purpose of these graphs is to examine the thickening or thinning of the oceanic crust within the lower density zones and propagator wake regions. For crustal architectural graphs that have no observed undulations for the crustal boundaries, the data is coming from seismic refraction experiments instead of seismic reflections.

The first observation regarding these graphs of lower density zones (Fig. 5.9) is that all of the previously identified propagator wakes (Fig. 5.8) are correlating with the lower density zones. Also, the PSF lineaments—picked up from magnetic anomaly—are assumed to have lower density to maintain their tectonic origin. The graphs of residual Bouguer gravity anomalies suggest that pseudofault lineaments are aligned with gravity lows, although they are not always exactly positioned over the gravity minima. The interpreted pseudofault lineaments are approximated as line features, while in reality, they represent zones (smaller than propagator wakes) within the oceanic crust. The resolution of potential field data used in the analysis does not allow for more detailed mapping of pseudofault lineament zones. As the lineaments (interpreted from magnetic data) approximate the zones of weakened crust, their general alignment with gravity lows

strengthens the derived interpretation, although no exact match is expected due to a lack of potential fields data resolution.

All the lower density zones can be associated with entirely or in part of the lower residual Bouguer gravity anomalies. In some cases, a component of significant Bouguer gravity high can be observed within these lower density zones (e.g., lower density zones 6 and 7 in Fig. 5.9) which potentially relates to one or several buried seamounts nearby. However, it is not possible to evaluate this claim in this study because the lower density zones 6 and 7 are located beneath a thick pile of sediments and is only constrained by broad-scale features from seismic refraction experiments (Fig. 3.5a and 3.5b), that can only show large buried seamounts, such as the one in Fig. 3.5b. Assessment of potential field maps in that region is further complicated by significant N-S oriented folds within the accretionary prism that mask the finer scale signals from buried seamounts. From a crustal architectural viewpoint, no significant thickening or thinning of oceanic crust can be observed for lower density zones related to newly identified PF lineaments. In contrast, the propagator wake regions show a crustal thinning of approximately 0.5 km which is consistent with all the previous studies (Nedimović et al., 2005; Marjanović et al., 2011).

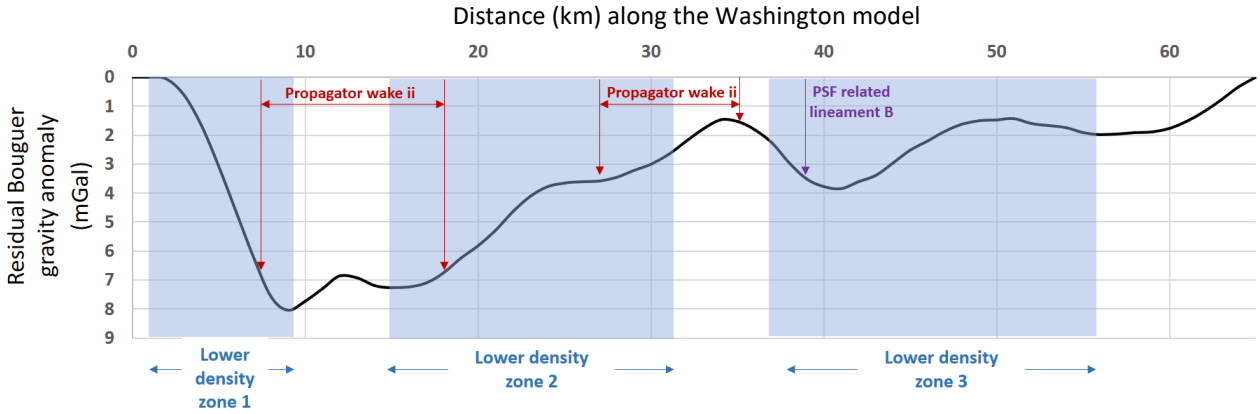
Distance (km) along the Washington model
0
10
20
30
40
50
60
Residual Bouguer gravity anomaly (mGal)
0
1
2
3
4
5
6
7
8
9
Propagator wake ii
Propagator wake ii
PSF related lineament B
Lower density zone 1
Lower density zone 2
Lower density zone 3

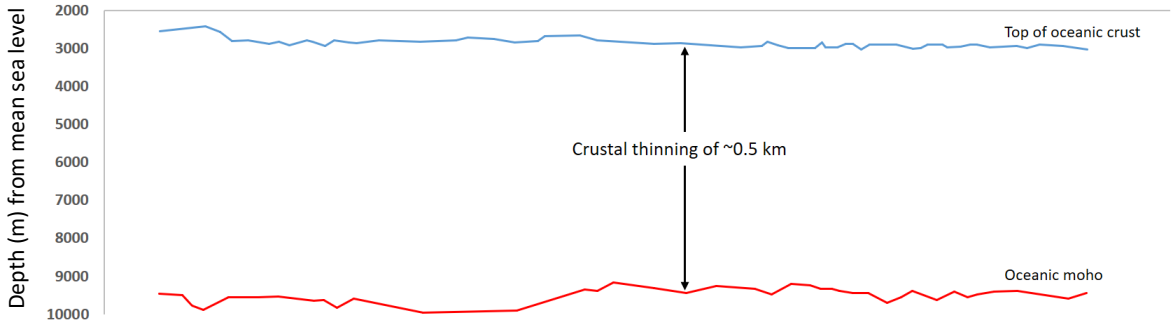
Depth (m) from mean sea level
2000
3000
4000
5000
6000
7000
8000
9000
10000
Top of oceanic crust
Crustal thinning of ~0.5 km
Oceanic moho

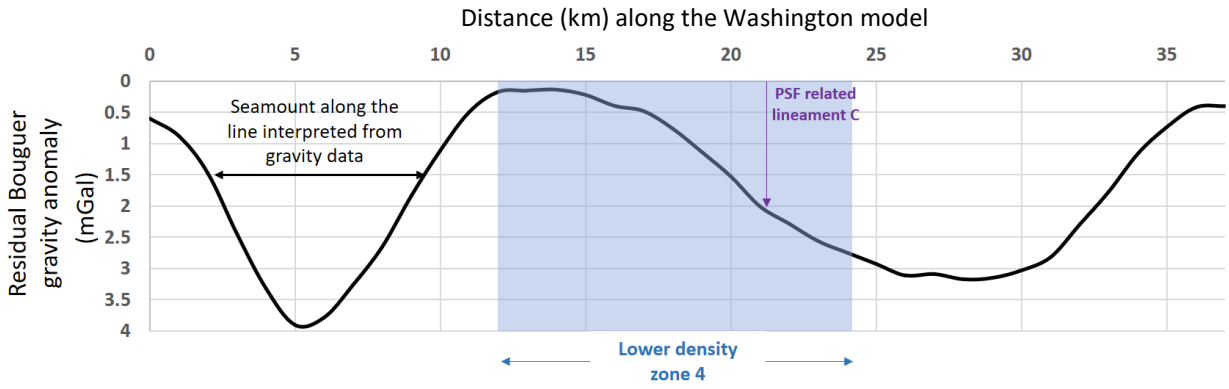
Distance (km) along the Washington model
0
5
10
15
20
25
30
35
Residual Bouguer gravity anomaly (mGal)
0
0.5
1
1.5
2
2.5
3
3.5
4
Seamount along the line interpreted from gravity data
PSF related lineament C
Lower density zone 4

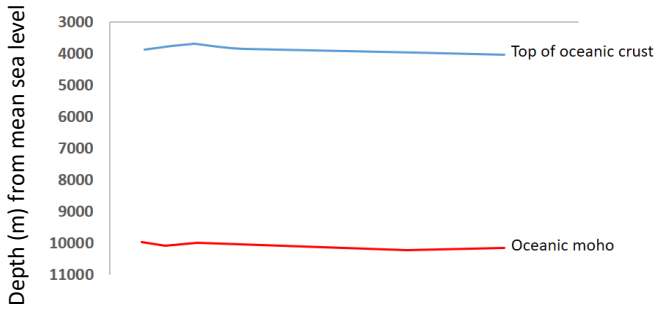
Depth (m) from mean sea level
3000
4000
5000
6000
7000
8000
9000
10000
11000
Top of oceanic crust
Oceanic moho

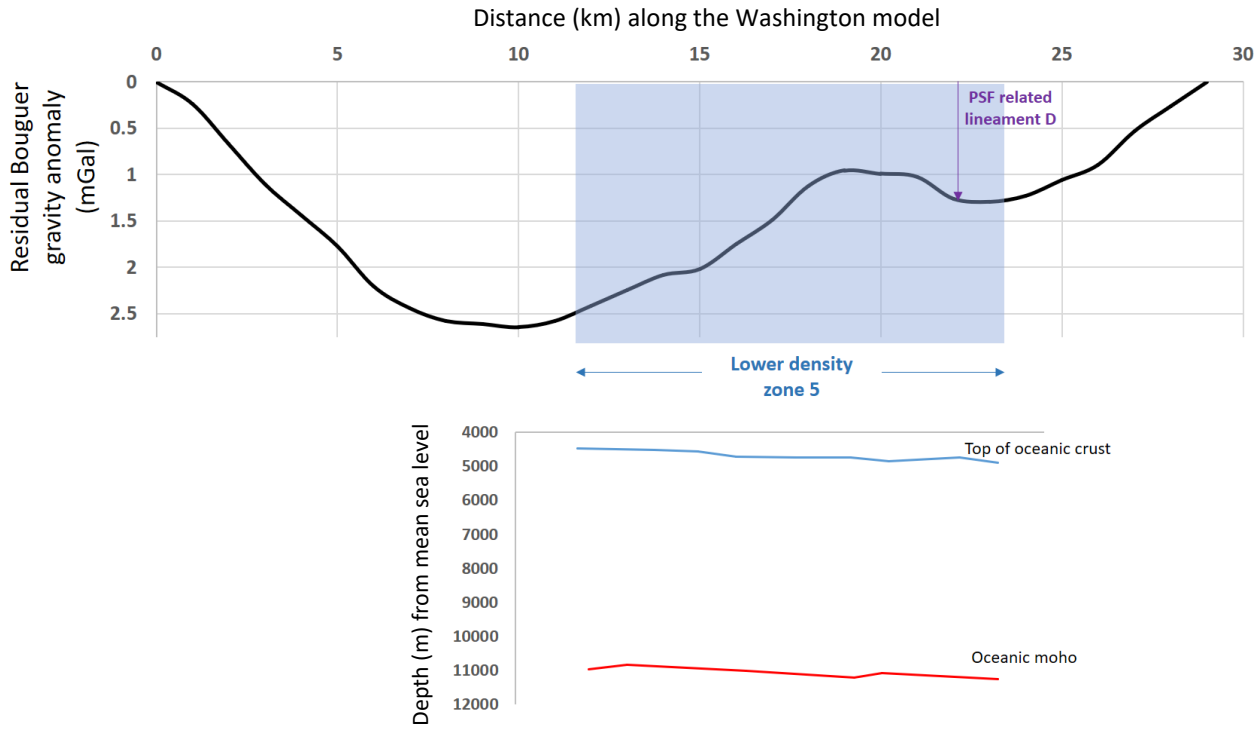
Distance (km) along the Washington model
0
5
10
15
20
25
30
Residual Bouguer gravity anomaly (mGal)
0
0.5
1
1.5
2
2.5
PSF related lineament D
Lower density zone 5
Depth (m) from mean sea level
4000
5000
6000
7000
8000
9000
10000
11000
12000
Top of oceanic crust
Oceanic moho

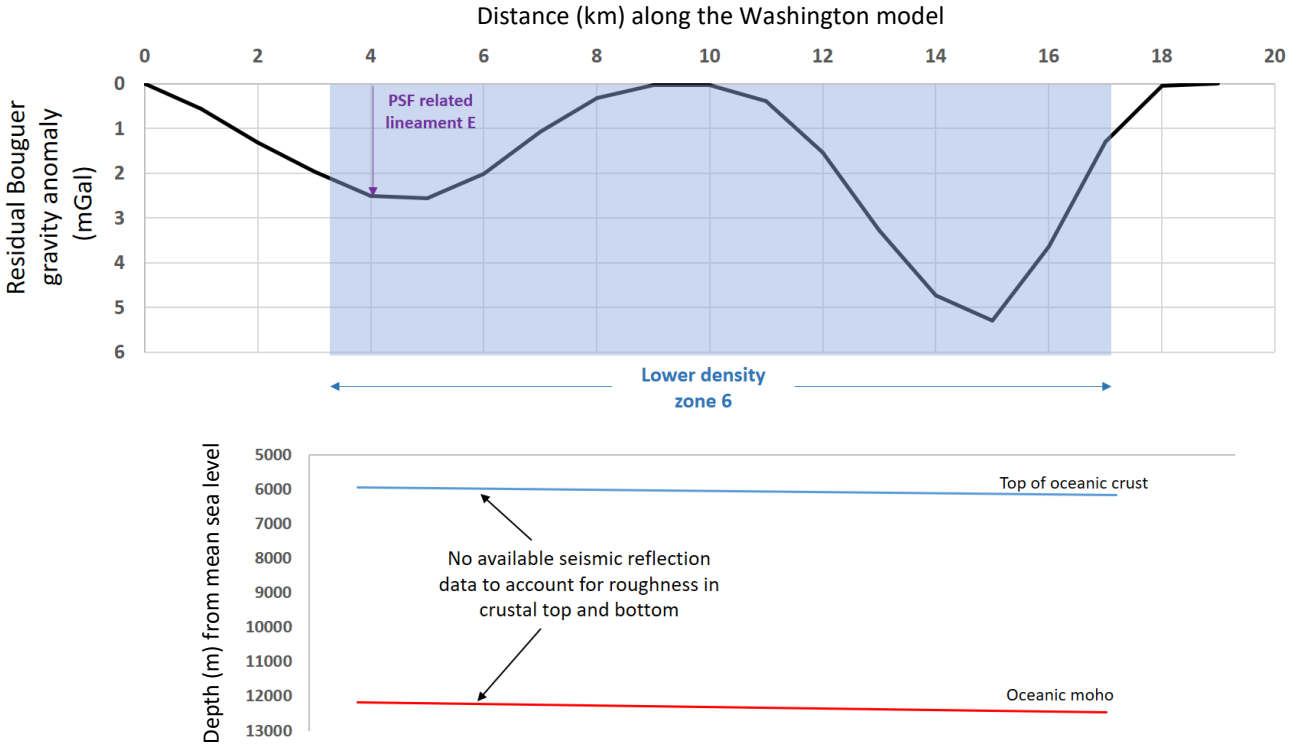
Distance (km) along the Washington model
0
2
4
6
8
10
12
14
16
18
20
Residual Bouguer gravity anomaly (mGal)
0
1
2
3
4
5
6
PSF related lineament E
Lower density zone 6
Depth (m) from mean sea level
5000
6000
7000
8000
9000
10000
11000
12000
13000
Top of oceanic crust
No available seismic reflection data to account for roughness in crustal top and bottom
Oceanic moho

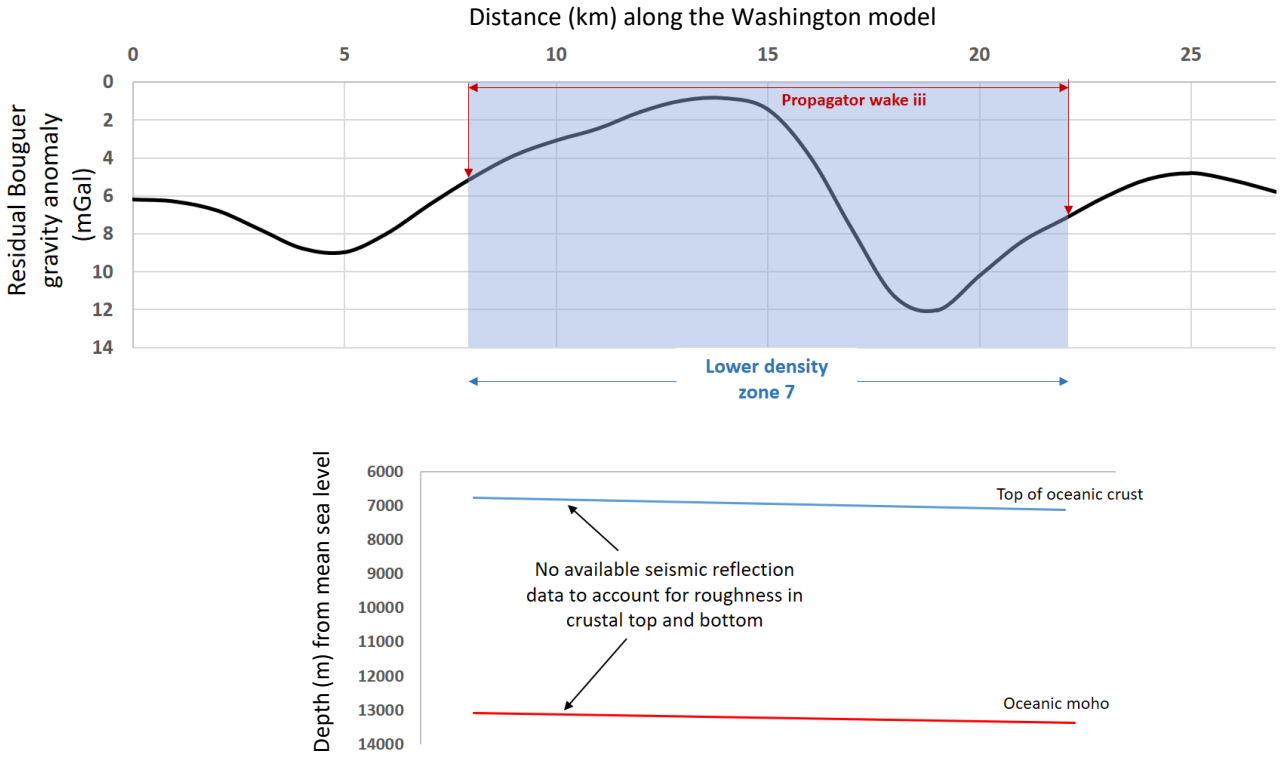
Distance (km) along the Washington model
Residual Bouguer gravity anomaly (mGal)
Propagator wake iii
Lower density zone 7
Depth (m) from mean sea level
Top of oceanic crust
No available seismic reflection data to account for roughness in crustal top and bottom
Oceanic moho

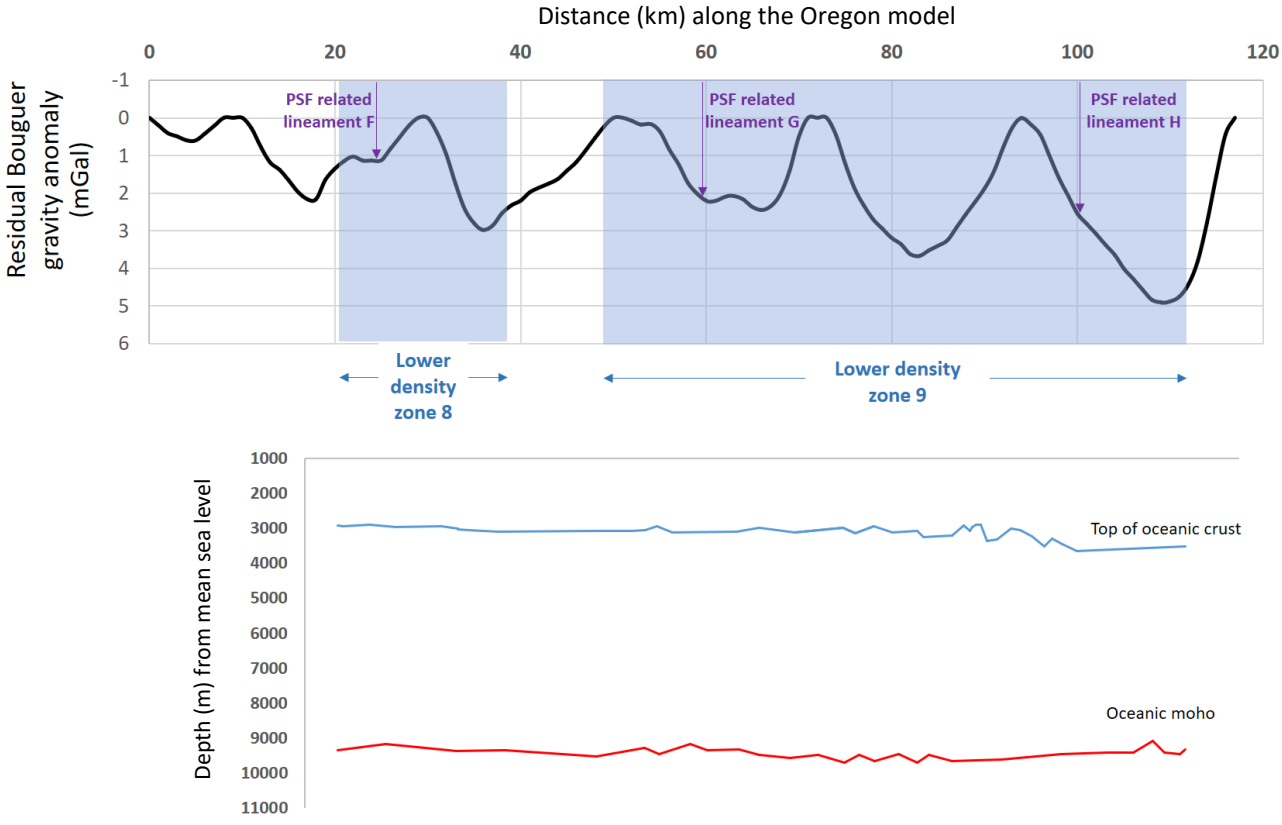
Distance (km) along the Oregon model
Residual Bouguer gravity anomaly (mGal)
PSF related lineament F
PSF related lineament G
PSF related lineament H
Lower density zone 8
Lower density zone 9
Depth (m) from mean sea level
Top of oceanic crust
Oceanic moho

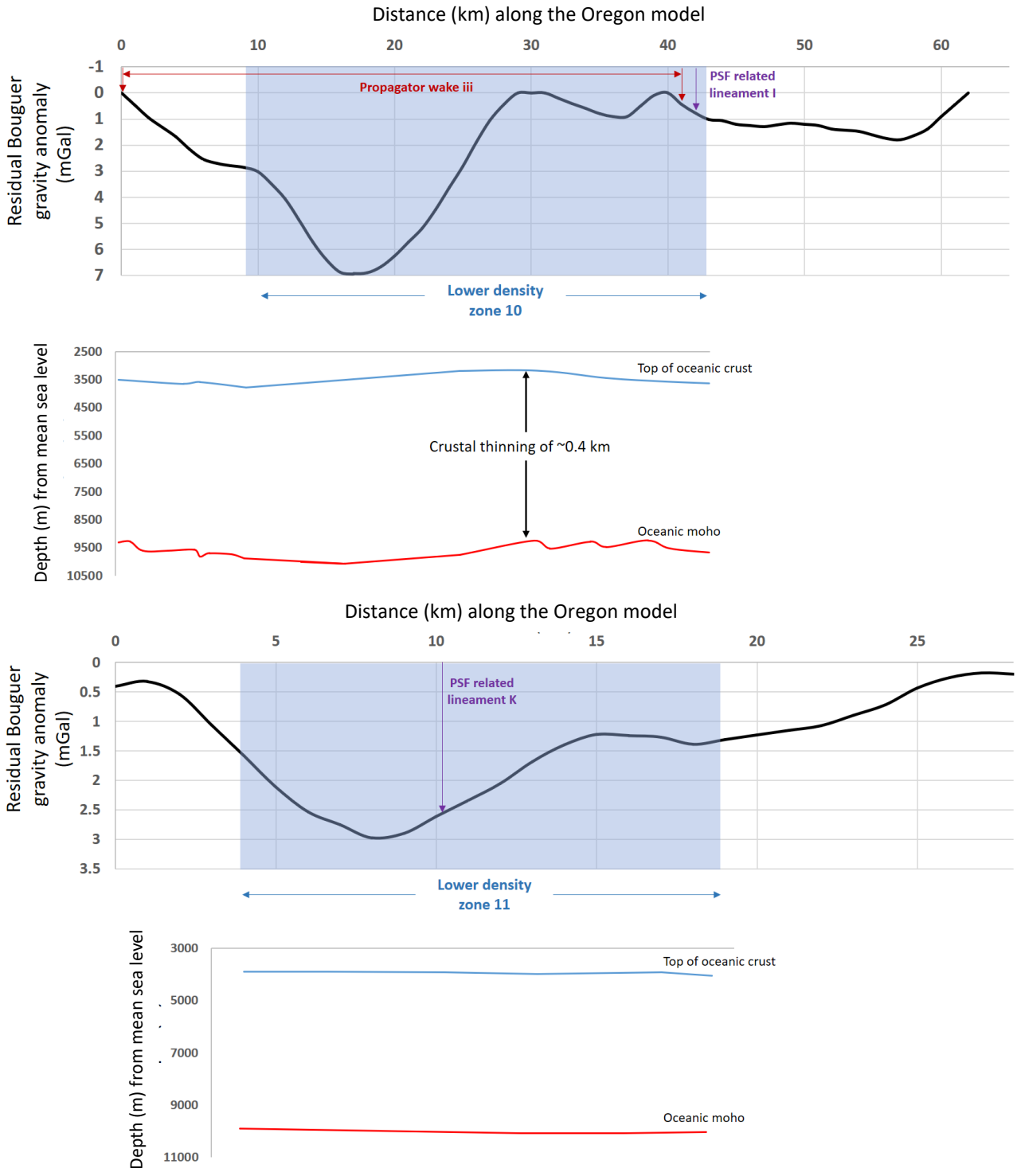
Distance (km) along the Oregon model
Residual Bouguer gravity anomaly (mGal)
Propagator wake iii
PSF related lineament I
Lower density zone 10
Depth (m) from mean sea level
Top of oceanic crust
Crustal thinning of ~0.4 km
Oceanic moho
Distance (km) along the Oregon model
Residual Bouguer gravity anomaly (mGal)
PSF related lineament K
Lower density zone 11
Depth (m) from mean sea level
Top of oceanic crust
Oceanic moho

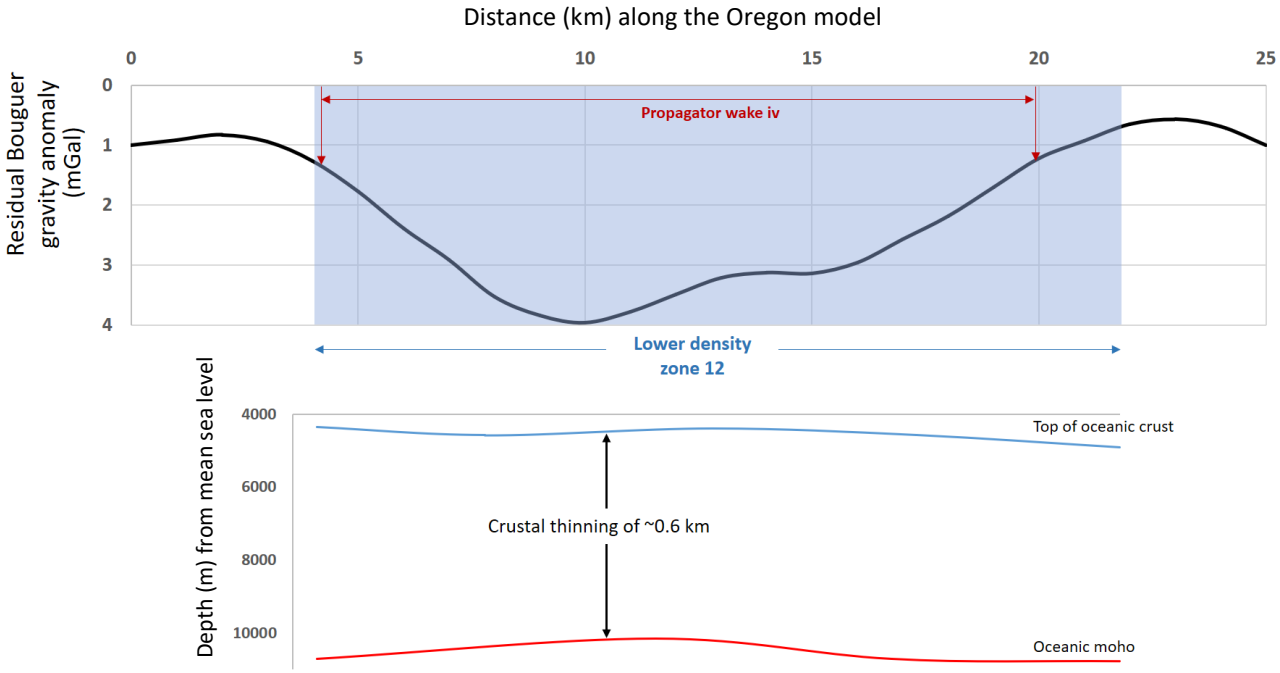

Figure 5.9: Residual Bouguer gravity anomaly graphs of lower density zones from Washington (Fig. 5.1) and Oregon (Fig. 5.2) models with the associated crustal architecture.

5.2.3 Mapping of seamounts

The other key tectonic structures investigated in this study are seamounts. Bathymetric (i.e., evident in bathymetry) seamounts are evident on the Pacific plate, however, a few of them can be observed on JdF, Gorda, and Explorer plates as well (Fig. 1.1). Origin of the large clusters or chains of seamounts (e.g., the Cobb-Eickelberg seamount chain) relates to hotspots on the JdF and Explorer ridge systems (Wessel and Kroenke, 1998). In addition to these bathymetric seamounts, interpretations of seismic reflection images reveal several buried seamounts (Fig. 3.3) over the JdF plate. The objective was to map these buried seamounts from potential field data. Since the strong magnetic reversals conceal the signals from seamounts in the magnetic anomaly data, they are primarily

mapped from filtered Bouguer gravity data (Fig 5.10). At first, a characteristic Bouguer gravity signal has been isolated for known bathymetric seamounts. Peripheries of the bathymetric seamounts show gravity high in the Bouguer anomaly, while the central locations have gravity low (Fig. 5.10). Because seamounts—generated from mantle materials that seep through structurally weak crustal zones—have younger rocks than the surrounding oceanic crust, it is geologically valid to observe Bouguer gravity low associated with the seamounts (Fig. 5.10).

This characteristic gravity signal was then justified with seamounts interpreted from seismic reflection images. Fig. 3.3 shows the seamounts in the seismic reflection image while Fig. 5.10 illustrates the locations of those seamounts in the gravity map. Based on this gravity signal (i.e., gravity high at the outer edge and gravity low in the inner regions), several seamounts have been interpreted from the residual Bouguer gravity anomaly (Fig. 5.10). All these types of seamounts have similar gravity signals which are further illustrated in graphs in Fig. 5.11

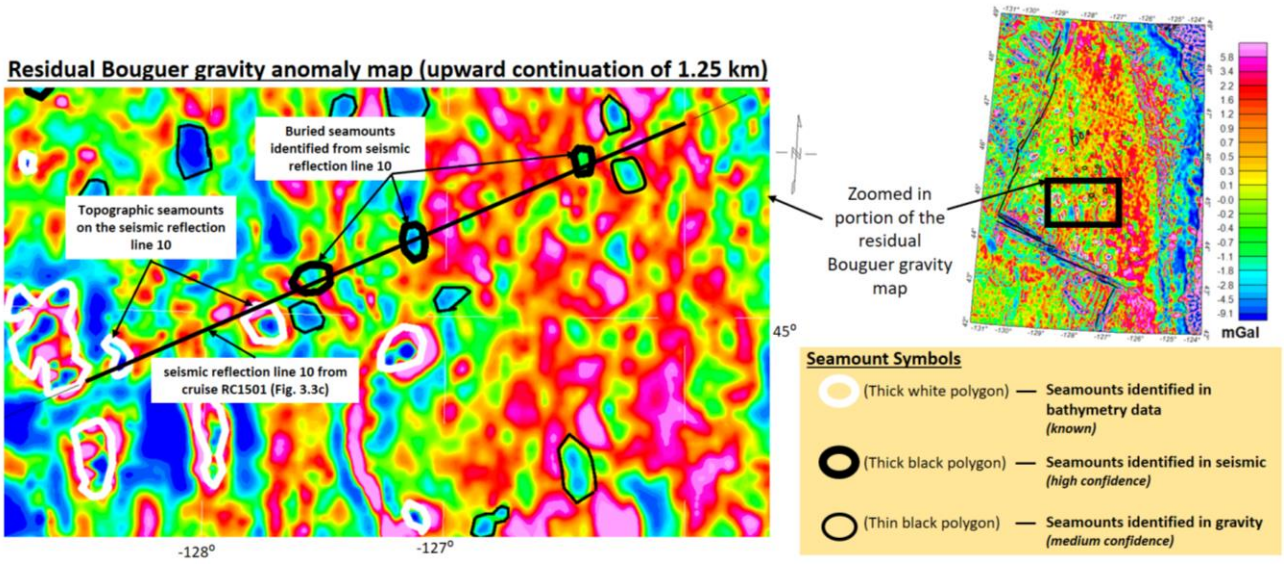

Figure 5.10: Gravity map where the characteristic signals are being isolated (background is residual of Bouguer gravity anomaly)

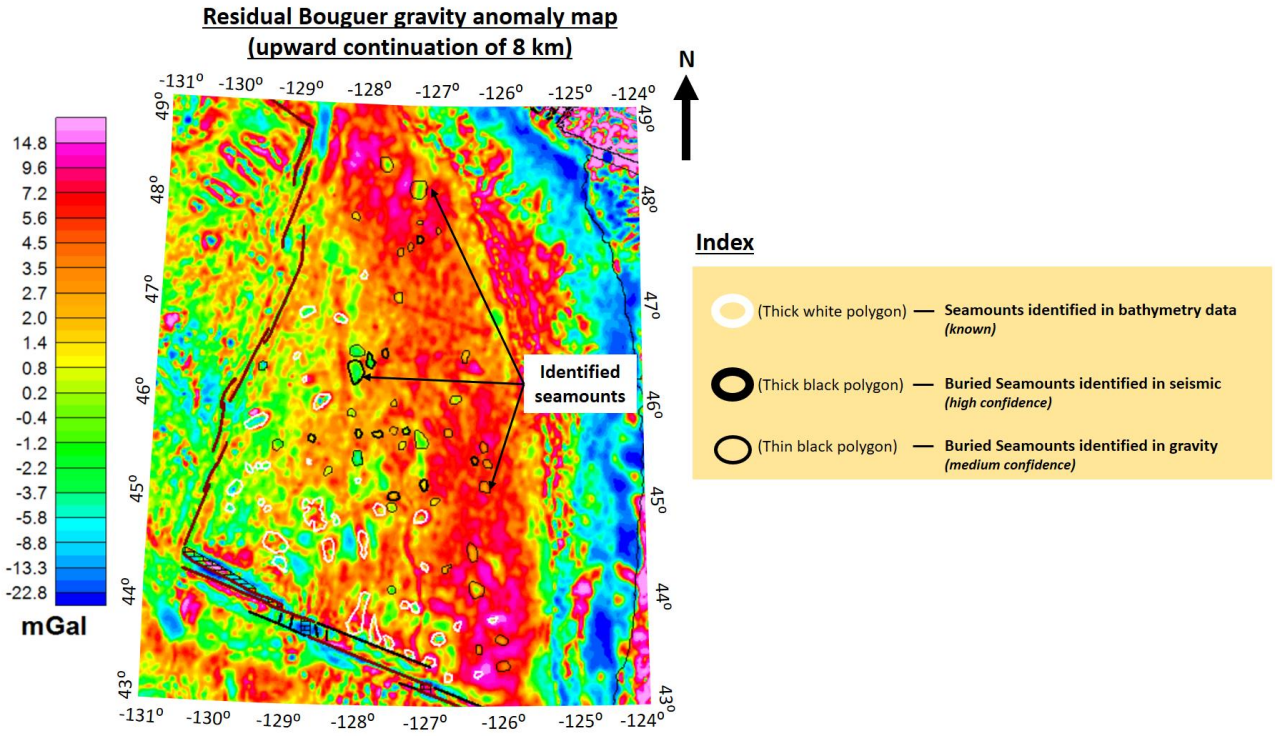

Figure 5.11: Gravity map with all types of seamounts

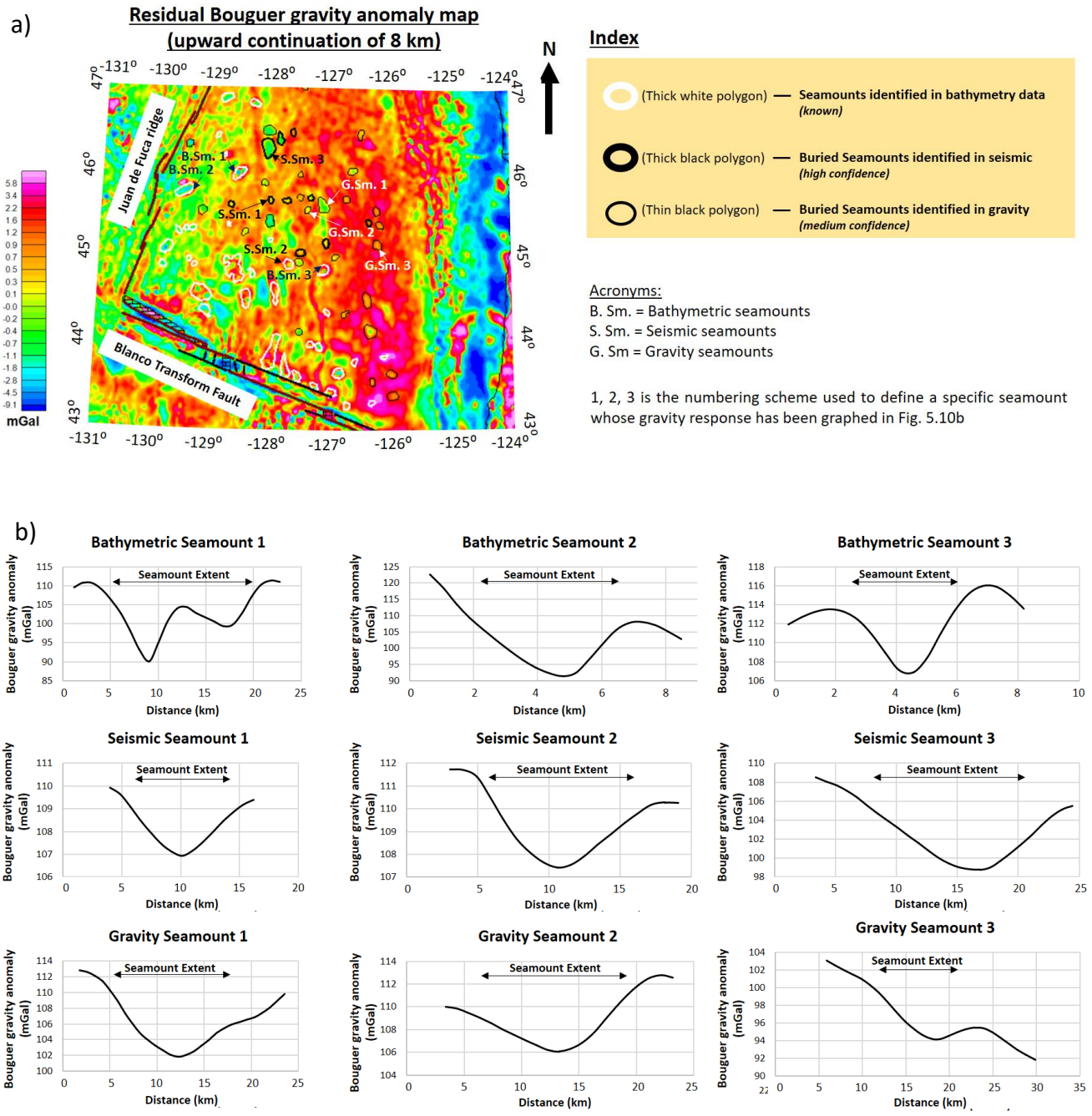

Figure 5.12: Graphs from three different types of seamounts. a) The location of 9 analyzed seamounts. b) Bouguer gravity anomaly along those 9 seamounts.

Chapter 6: Discussions

6.1 Comparison between plate-scale models

The notion behind the 2D modeling is to compare and contrast the physical properties of rocks and crustal architectures between two different models (Fig. 5.1 and 5.2) that go through two different seismicity zones (Fig. 1.1). The difference in crustal architecture and rock properties between the two models is expected to provide clues regarding the seismicity segmentation over the CSZ.

In both developed integrated models (Fig. 5.1 and 5.2), the physical property distribution of subsurface rocks is more geologically valid, detailed and closer to the global average than the other plate scale models (Romanyuk et al., 1998; Blakely et al., 2005). Models of this research also do not require hydration of the upper mantle as it is required in the modeling of Blakely et al. (2005). Since the depths to the subsurface layers of both plate scale models are well constrained with seismic data, the only parameter that can be varied during modeling is density. To test the sensitivity of gravity modeling to density variations, a series of tests were performed for both models. Fig. 6.1 illustrates an example of gravity response to varying density within one of the established lower density zones. In this test, the density of that block is changed sequentially until it reaches the same density as the surrounding crust. The gravity response to each step has been recorded, suggesting that the assigned densities offer the best fit for observed free air gravity anomaly.

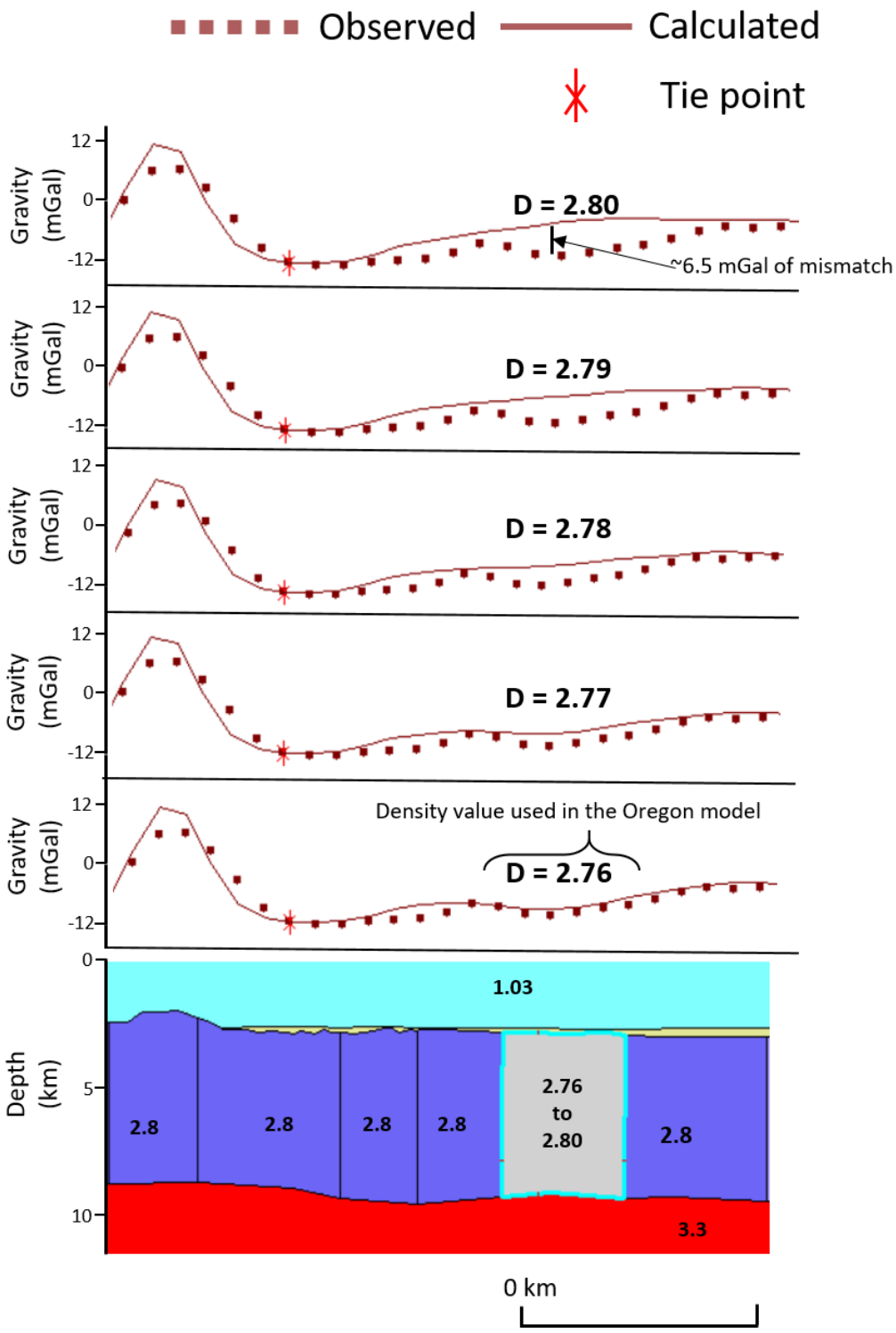

Figure 6.1: Sensitivity test for the modeled density values along the Oregon model (Fig. 5.2). 'D' on the gravity profile represents the assigned density of the block directly underneath. Numbers written on the subsurface model in the bottom panel show the densities of the modeled blocks.

There are a lot of similarities that can be observed between the developed integrated models of this study (Fig. 5.1 and 5.2) that are listed in Tables 6.1 and 6.2; these similarities increase the confidence and geological validity of our models. For example, the thickness and density of the JdF oceanic crust are similar between the Washington (Fig. 5.1) and Oregon models (Fig. 5.2). Our modeling also requires a similar dipping angle of subducting JdF crust between these two regions (i.e., 13° vs 14° beneath the Siletz terrane), which is consistent with the previous studies of JdF slab geometry over the CSZ (McCrory et al., 2012). Also, the similar thickness (32 km), density (3.09 vs 3.085 g/cc), and magnetic susceptibility (5000 μCGS) of Siletz terrane indicate a shared geological origin. All of the other similar parameters are summarized in Table 6.2, whereas, the exact values are listed in Table 6.1.

The discrepancies between Washington and Oregon models (also listed in Tables 6.1 and 6.2) potentially relate to differences in geology or tectonics for two models through different seismicity zones (Fig. 1.1). Requirement of slight lower density (0.005 g/cc) for upwelling magma region in spreading center of the Oregon model indicating the presence of the Cobb hotspot (Karsten and Delaney, 1989; Wessel and Kroenke, 1998; Chadwick et al., 2005) is an example of this. Another example of model discrepancies leading to geological differences is the width of the accretionary prism between Washington and Oregon. In Washington, the accretionary prism is 110 km wider than in Oregon which is resulting from greater continental sediment supply from oblique subduction (Davis and Hyndman, 1989). The contact width of accretionary prism and

Siletz terrane with oceanic crust also varies between two different models. This study documented multiple differences and similarities in the structures between high and low seismicity regions. The number of differences does not immediately allow to identify a single parameter that is responsible for observed seismicity segmentation. It is also possible that all of these factors are combinedly responsible for this observed variation in the number of earthquakes between Oregon and Washington.

Table 6.1: Comparison of physical properties and crustal architectures between two plate-scale models

Feature/ Location	Parameter	Oregon Model	Washington model
Oceanic Spreading center	Density for the zone of upwelling magma (i.e., lower density mantle rocks)	3.23 g/cc	3.235 g/cc
	Density of oceanic crust	2.8 g/cc	2.8 g/cc
	Width of lower density mantle rocks beneath oceanic moho	40 km	13 km
	Thickness of oceanic crust beneath JdF spreading ridge	6.75 km	6.35 km
Non-subducting oceanic crust	Thickness of oceanic crust	5.5 – 6.5 km	6.5– 6.8 km
	Maximum depth of overlying undeformed sediments	~2km	~2 km
	Density of undeformed sediments	2.1 – 2.4 g/cc	2.1– 2.4 g/cc
Lower density zones of oceanic crust	Number of lower density zones	5	7
	Density range of lower density zones	2.76 – 2.82 g/cc	2.76 – 2.86 g/cc
Accretionary prism	Width	105 km	215 km
	Maximum depth	~13 km	~15 km
	Density	2.45 – 2.75 g/cc	2.45 – 2.75 g/cc
	Width of accretionary prism in contact with oceanic crust	51.5 km	133 km
Subducting oceanic crust	Dip angle (beneath accretionary prism)	6^{o}	7^{o}
	Dip angle (beneath Siletz terrane)	13^{o}	14^{o}

Siletz terrane	Width	140 km	192 km
	Thickness	32 km	32 km
	Density	3.085 g/cc	3.09 g/cc
	Magnetic susceptibility	5000 µCGS (upper part) and 2000 µCGS (lower part)	5000 µCGS
	Width of the terrane in contact with subducting oceanic crust	85 km	27 km
Continental sedimentary basin	Max. thickness	~2.5 km	~4.5km
	Density	2.65 g/cc	2.65 g/cc
	Magnetic susceptibility	0 cgs	3000 µCGS
Cascadia Arc	Density	2.96 g/cc	3.00 g/cc
	Magnetic Susceptibility	5000 µCGS	2000 µCGS

Table 6.2: Summary of comparison between two plate-scale models

Feature/Location	**Properties showing similarities between two models**	**Discrepancies between two models**
Spreading center		Density and width of lower density mantle rocks
Oceanic crust	Thickness and density	Number of lower density zones (7 vs 5)
	Dip of subducting part	
Undeformed sediments	Thickness and density	
Accretionary prism	Thickness and density	Width of the entire feature (215 vs 105 km)
		Width of the feature that is in contact with oceanic crust (133 vs 51.5 km)
Siletz terrane	Thickness, density and magnetic susceptibility	Width (192 vs 140 km)
		Width of the feature that is in contact with oceanic crust (27 vs 85 km)
Continental sedimentary basin	Density	Thickness and magnetic susceptibility
Cascadia arc		Density and magnetic susceptibility

One of the most notable findings of the 2D modeling is the presence of lower density regions within the JdF oceanic crust (see section 5.1.1 for details and Fig. 6.2). Geologically, a normal oceanic crust gets denser as it moves away from the spreading center and heads toward the subduction zone (Carlson and Herrick, 1990). Two factors

are responsible for this occurrence. One is the directly proportional relationship between crustal density with age or distance from the spreading center. The other is the crustal hardening caused by increasing exposure time to the significant tectonic force from the subducting oceanic crust. Through the geophysical integrated modeling in this study, several crustal zones have been identified in the JdF plate that deviate from the normal oceanic crustal density; they are numbered from 1 to 12 Figs. 5.1 and 5.2. These zones require lower density than the surrounding crust, as is illustrated in Fig. 6.2. Fig. 6.3 illustrates how the previously identified propagator wakes (Fig. 5.6b) and newly identified PSF lineaments (Fig. 5.6c) correlate with these lower density zones of the JdF plate.

a)

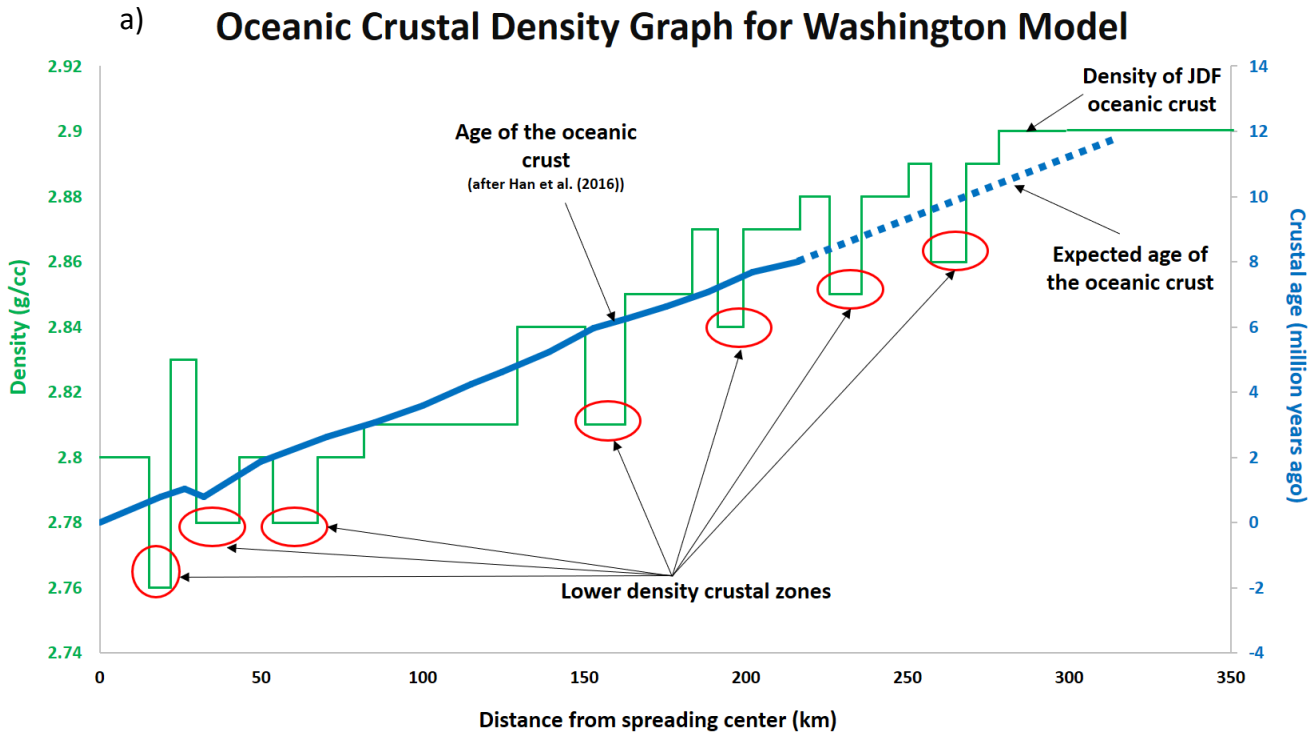

b)

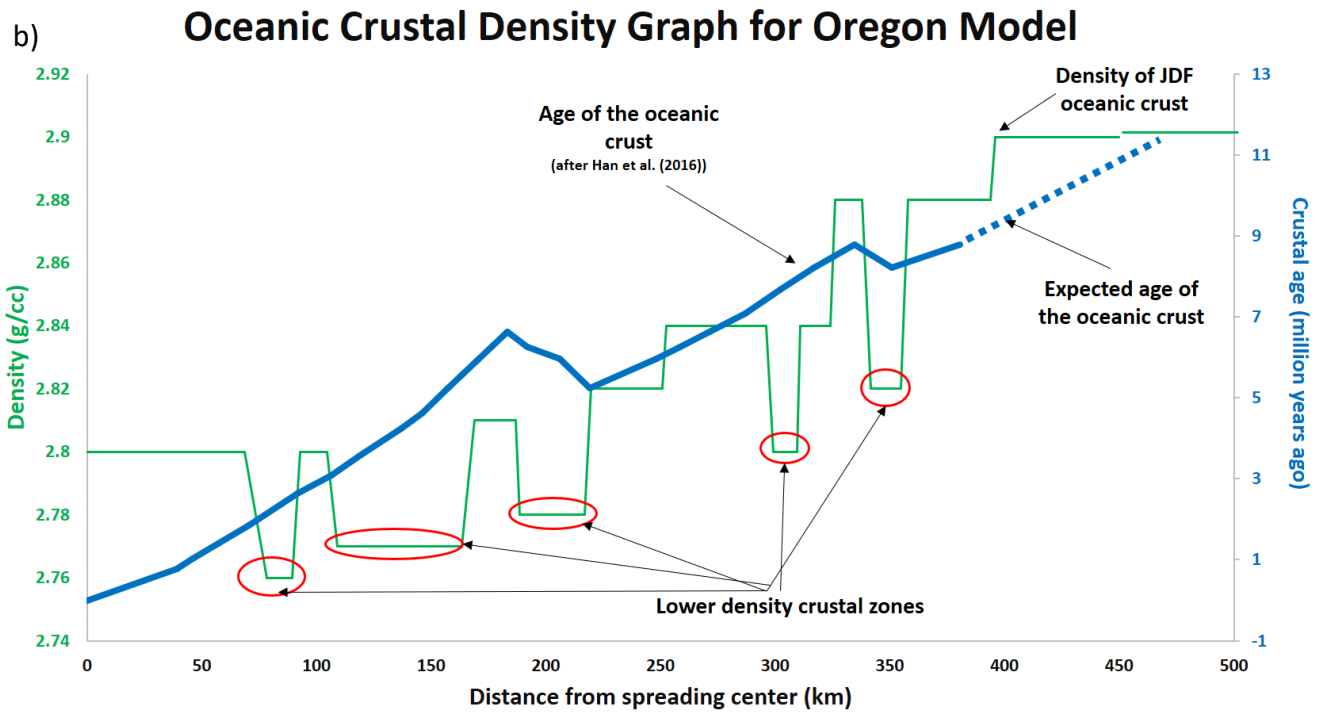

Figure 6.2: Graph-crustal density for Washington model (a) and Oregon model (b)

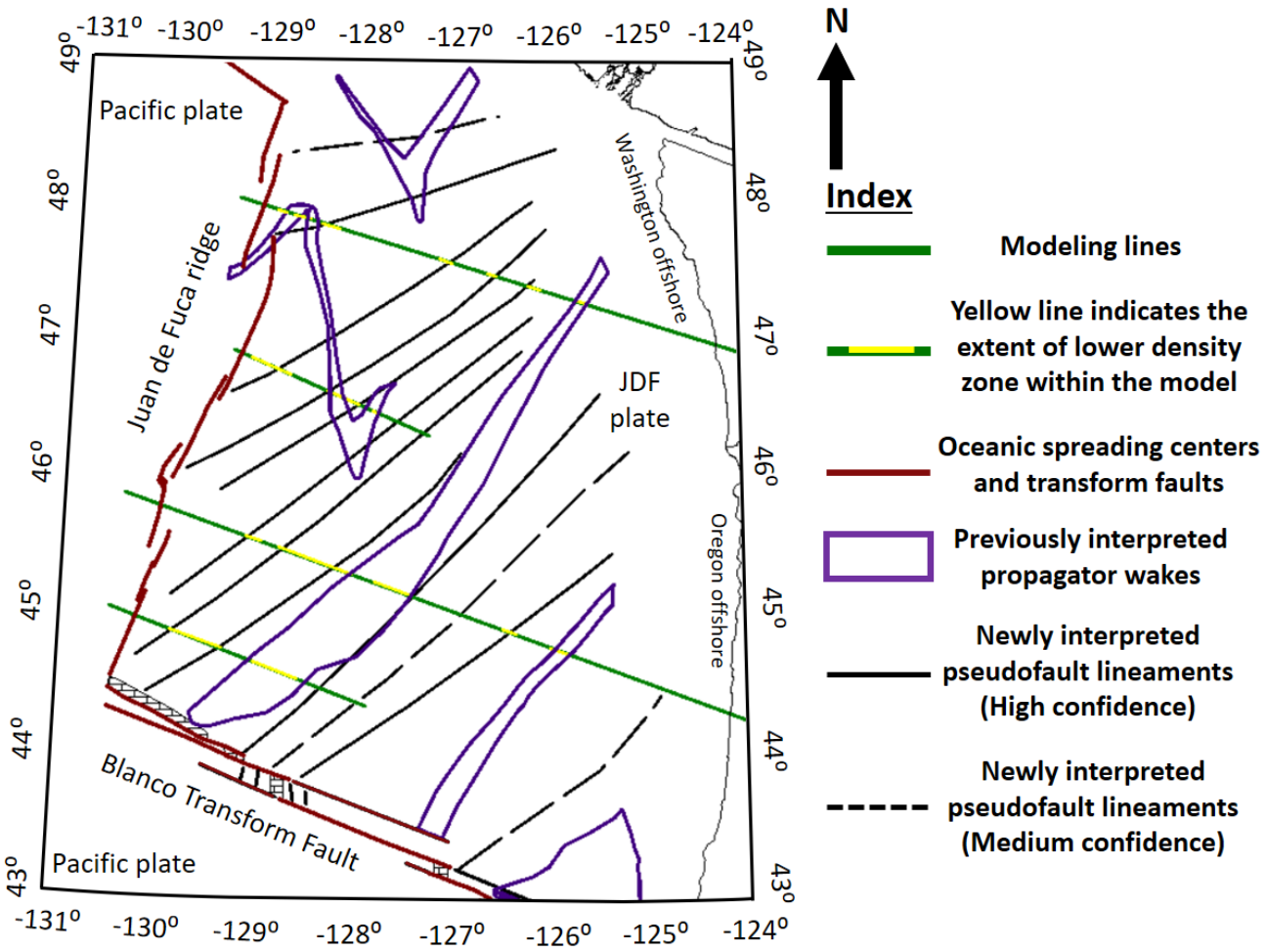

Figure 6.3: Map showing a correlation between the identified PSF lineaments, propagator wakes and lower density zones.

6.2 Association of propagator wakes with lower density crustal zones

As already was mentioned, the conclusion about low-density oceanic crust in the propagator wakes contradicts the gravity modeling of Marjanović et al. (2011) that shows propagator wakes have higher density crust (see section 2.4.3 for details). The supporting evidence toward this study's conclusion are:

- In the gravity modeling of Marjanović et al. (2011), the density distribution of the basaltic layer ranges from 1.7 to 2.4 g/cc. These values do not correlate to the other regions of the world (Carlson and Herrick, 1990). For basaltic layers, these densities should be around 2.65 g/cc (Carlson and Herrick, 1990). Since the basaltic layer is the shallowest portion of the oceanic crust, densities of this layer have a strong influence on the calculated gravity response. In the case of Marjanović et al. (2011), the rock porosities measured from core log data using an empirical equation (Carlson and Herrick, 1990) were utilized to derive bulk densities. However, the drilling program (ODP sites 1025 and 1029) only sampled the topmost portion of the basaltic layer (2 meters of basalt in site 1025 and 3 meters of basalt in site 1029). This topmost basaltic layer has a high probability of being weathered that can eventually result in higher porosity and lower density measurements than the real values.
- The models in Marjanović et al. (2011) were developed based on their calculated residual anomaly. However, this residual anomaly was calculated by subtracting “the mantle Bouguer anomaly” (i.e., computed gravity signature of the Moho boundary) from the free air gravity anomaly. This approach deviates from traditionally-established gravity analysis (i.e., much more confident effect of water-sediment contact (Bouguer correction) is usually removed, not a more ambiguous and less constrained effect of Moho; Telford et al., 1990). This approach can induce significant errors to the resultant gravity anomalies that they are trying to match in their forward modeling. The computation of mantle Bouguer anomaly holds several assumptions which may or may not be accurate. Relying on this calculation to extract gravity signals

for shallow structures (i.e., residual anomaly) may generate erroneous signals and lead to wrong interpretation.

- In Marjanović et al. (2011), one of the gravity models runs from the Northern Symmetric spreading ridge segment (Fig. 1.1 and 2.6b). The model crosses the same propagator wake (i.e., propagator wake 'ii') twice. Marjanović et al., (2011) developed two different models for these two zones, however, these models share a 10 km zone of the same profile (i.e., 90 to 100 km of Northern Symmetric profile in Marjanović et al. (2011) shown in Fig. 2.6b). Although this 10 km extent is shared, they have different densities for two different models. Since the zones are on the ends of the model they may induce unwanted edge effects to the models.
- In order to test the reliability of gravity modeling from Marjanović et al. (2011), the forward gravity modeling along the same profiles was conducted over the JdF plate (see section 5.1.4 for details). Noticeably, their extents of propagator wakes are not matching with the actual distances on the map. Proper extents of the propagator wake zones along the modeling lines are pointed out in Fig 5.1 and 5.2. Propagator wake extents of this study have carefully been drawn by Geosoft software by considering several different types of constraints (i.e., mapped propagator wakes from Wilson (2002), distances from the spreading axis, matching it with gravity models of Marjanović et al. (2011) and correlation of our bathymetric data with Marjanović et al., (2011) models.)
- Interpretations of gravity models from Marjanović et al. (2011) disregard the normal oceanic density distribution which is the gradual increasing pattern of densities away

from the spreading center (Fig. 6.2). Because of this, an oceanic crustal block at the edge of a propagator wake with normal oceanic density may be misinterpreted as a higher density crustal block. In gravity models developed in this study (Fig. 5.4b and 5.5b), normal oceanic density distribution has been taken into account, and regions that show aberrations (i.e., lower density than surrounding crust) from this pattern are designated as lower density zones, that correlate either to known propagator wakes or to newly identified PSF lineaments (Figs. 5.4b and 5.5b).

- Seamounts are the tectonic features that protrude upward from the surrounding oceanic crust. This protruded part of the crust results in a higher free-air gravity anomaly than in the surrounding regions. However, the influences of these seamounts are completely ignored in the gravity modeling of Marjanović et al., (2011). In the Cleft model, the crust on the western edge of the propagator wake 'iii' region requires higher density than the normal density distribution allows. However, this gravity high can be traced to the influence of a nearby bathymetric seamount (Fig 5.3 and 5.4b). For the Northern Symmetric model, a large portion of the western segment of propagator wake 'ii' coincides with a similar gravity high (i.e., orange shaded zone in Fig. 5.5b) which has been used as evidence behind the higher density crusts in Marjanović et al. (2011). However, this apparent gravity high actually results from two nearby seamounts interpreted from the vintage seismic data (Fig. 3.3b and 5.3). Without considering the effects of seamounts, it would have not been possible to assign normal density to this zone.

Considering all the circumstances mentioned above, it can be stated with confidence that propagator wakes and newly interpreted PSF lineaments correspond to the lower density regions within the JdF oceanic crust (Fig. 5.1, 5.2, and 5.7). Furthermore, these lower density zones resulting from observed lows in gravity anomaly do not correspond with any crustal depressions or deepening of Moho (Fig. 5.7). This suggests the lower density zones are consequences either of compositional or structural changes within the oceanic crust.

6.3 Assessing the correlation between pseudofault lineaments and seamounts

Potential correlations between pseudofault lineaments and seamounts were investigated through statistical analysis summarized in Table 6.3. Spatial analysis in this section attempts to show that seamounts are clustered around propagator wakes and PSF lineaments.

Fig. 6.4 shows the northern part of the JdF plate where seamounts are strikingly clustering around PSF lineaments. Moreover, there is a lack of seamounts between PSF lineament B and C. This definite correlation, however, cannot be observed in the most southern part of the JdF plate (Fig. 6.5). For the pseudofault lineament 'L' and propagator wakes 'iv' and 'v', seamounts are observed to exist within the in-between spaces. Nonetheless, it is important to note that the most southern picked up lineament (i.e., pseudofault lineament 'L') is the least confident one. Because of the high deformation in the Northern Gorda plate (Chaytor et al., 2004) and since propagator wakes are only mapped from

disturbances in sea-floor magnetic stripes (Wilson, 2002), it is possible that the mapping of propagator wake 'v' also contains some error.

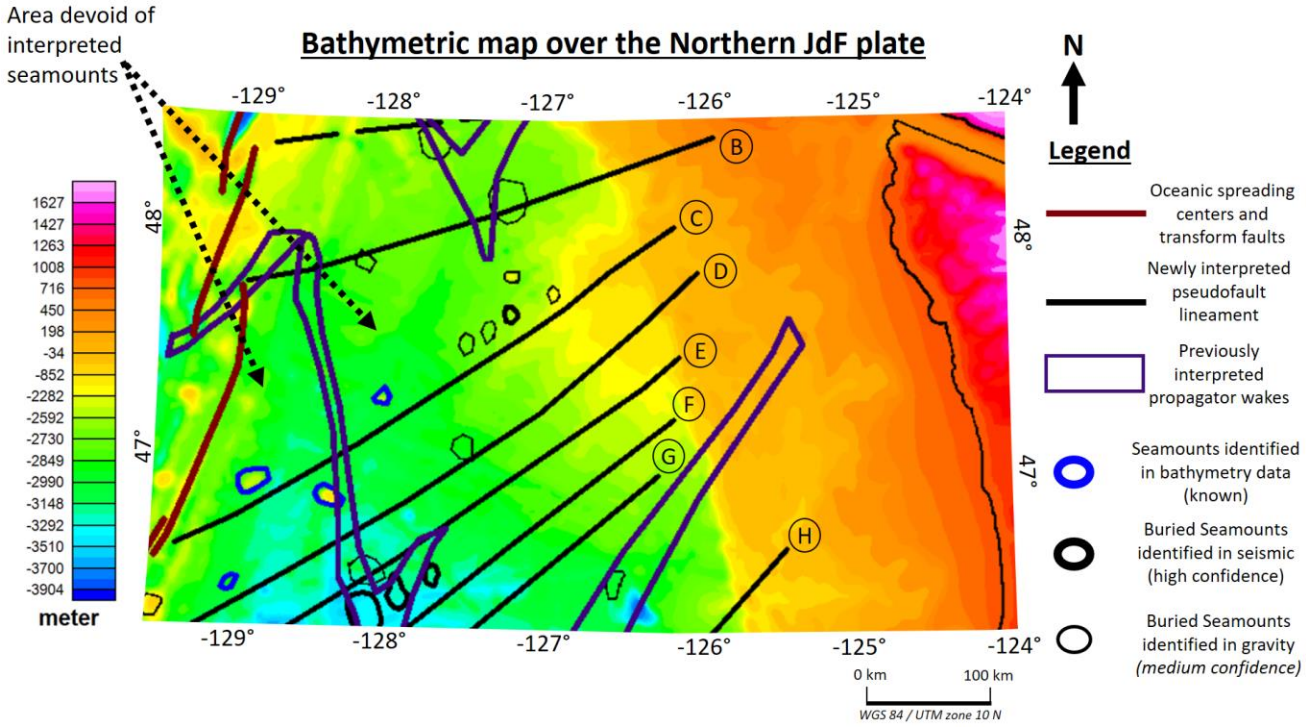

Figure 6.4: Bathymetric map over the northern JdF plate illustrating the spatial correlation between interpreted seamounts and PSF lineaments. Please note the lack of seamounts between lineament B and C as well as clustering seamounts around identified PSF lineaments. The statistical correlation between these structures is addressed in Fig. 6.6 and Table 6.3.

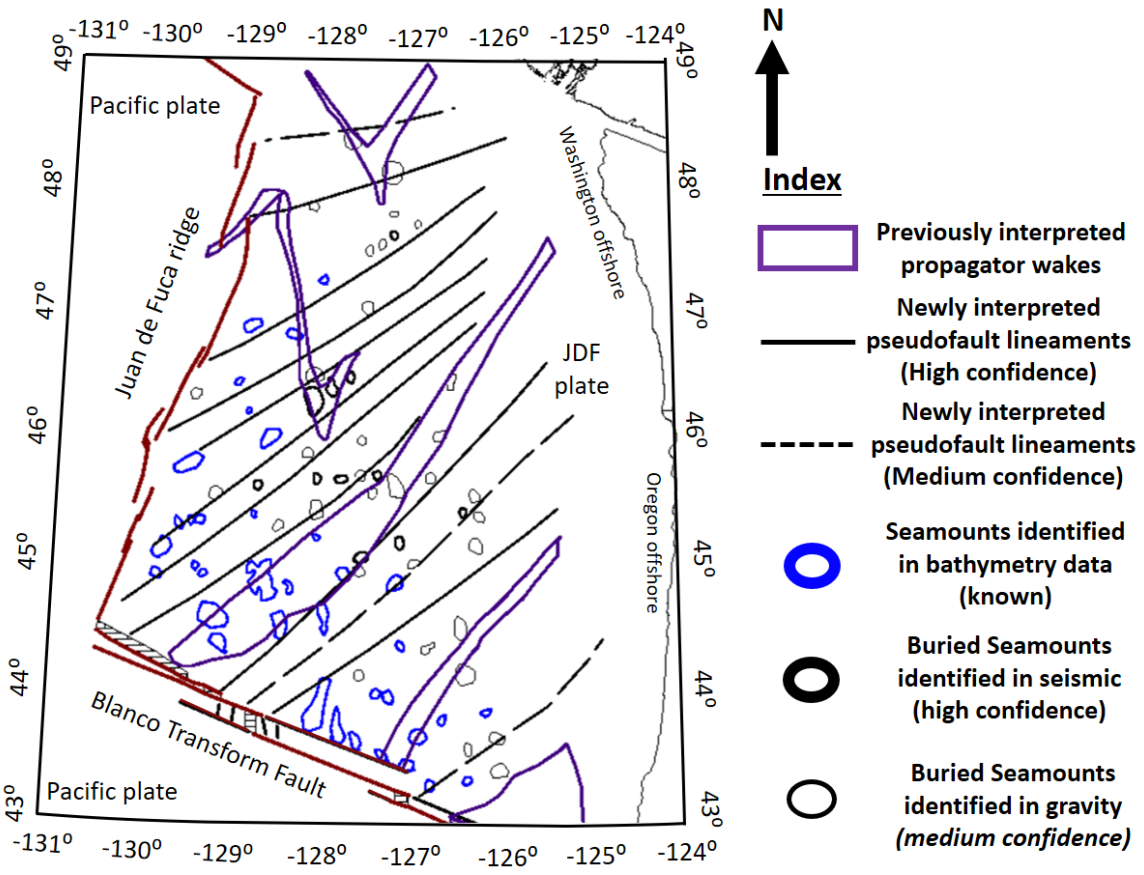

Figure 6.5: Correlation between propagator wakes, PSFs, and seamounts

Considering the distances between pseudofault lineaments (Table 6.3), the seamounts that are within 15 km range of a lineament are considered as spatially correlated. For the propagator wakes, only the seamounts within the zone are counted as spatially correlated. All of these spatially correlated seamounts are shown in the frequency distribution graph (Fig. 6.6a). Out of 85 mapped seamounts over the entire JdF plate, only 6 of the seamounts cannot be spatially correlated to ether known propagator wakes or to the newly interpreted PSF lineaments. These seamounts are termed as independent in the frequency distribution graph (Fig. 6.6a). The shared seamounts on this graph (Fig. 6.6a) are the ones that are within a 15 km zone of more than one pseudofault lineament.

These seamounts are counted twice as spatially correlated seamounts for two different lineaments.

The formation of these seamounts requires zones of structurally weakened crust for magma to rise up. This indicates that lower densities (i.e., an aberration from normal oceanic density) of JdF crust are generating from faulting or fracturing within the oceanic crust. Consequently, these lower density zones represent zones of crustal weakness and seamounts are forming through these zones when the crust is near the spreading center. This is also consistent with the established formation mechanism of propagator wakes where fossil transform faults and extinct ridges dominate the shared or fractured zone (Fig. 2.2b).

Although the propagator wakes and PSF lineaments are representing zones of crustal weakness, they have a clear distinction in terms of crustal architecture (Table 6.1 and 6.2). Propagator wakes have approximately 0.5 km thinner crust than the surroundings (Fig. 5.7). Moreover, each of the newly interpreted PSF lineaments (Fig. 5.6 and 6.5) has its western edge terminating at the offset between spreading ridge segments. Because of this, the PSF lineaments are hypothesized to be triggered by offsets between spreading ridge segments (Fig. 6.7) and consistent compressive tectonic force since its birth is introducing faults or fractures within the zone.

a)

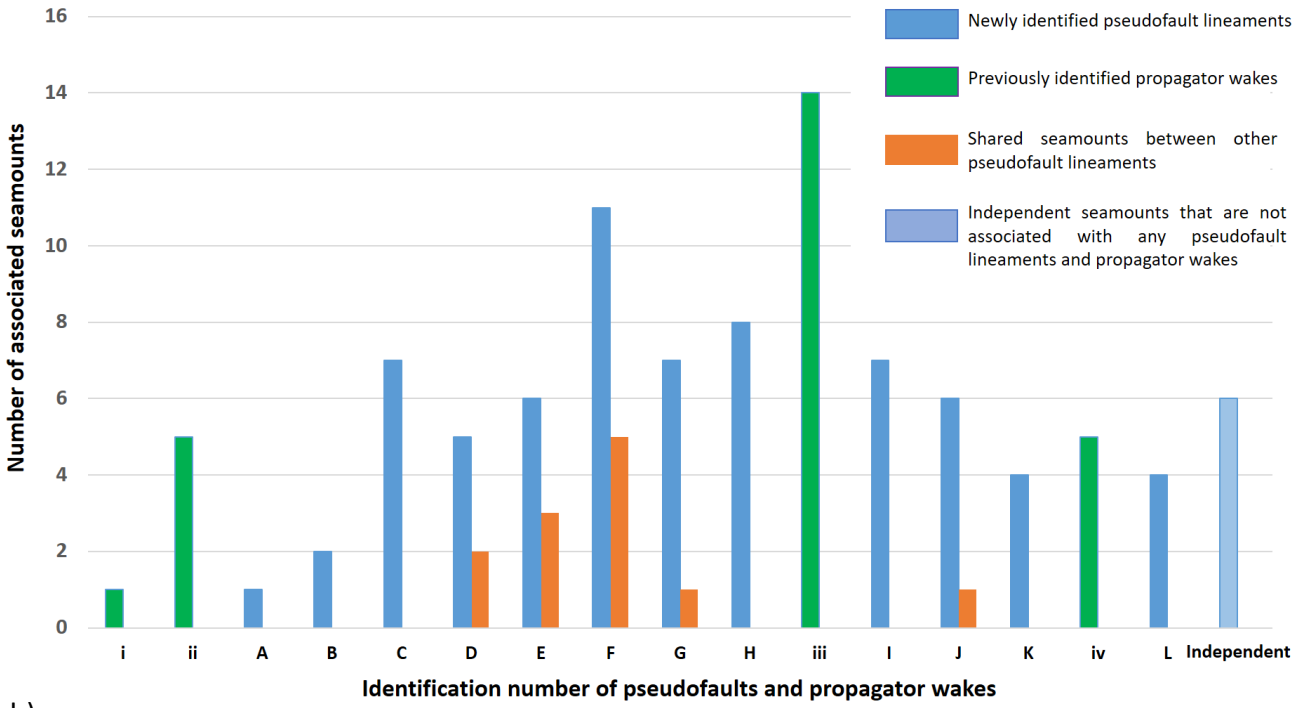

b)

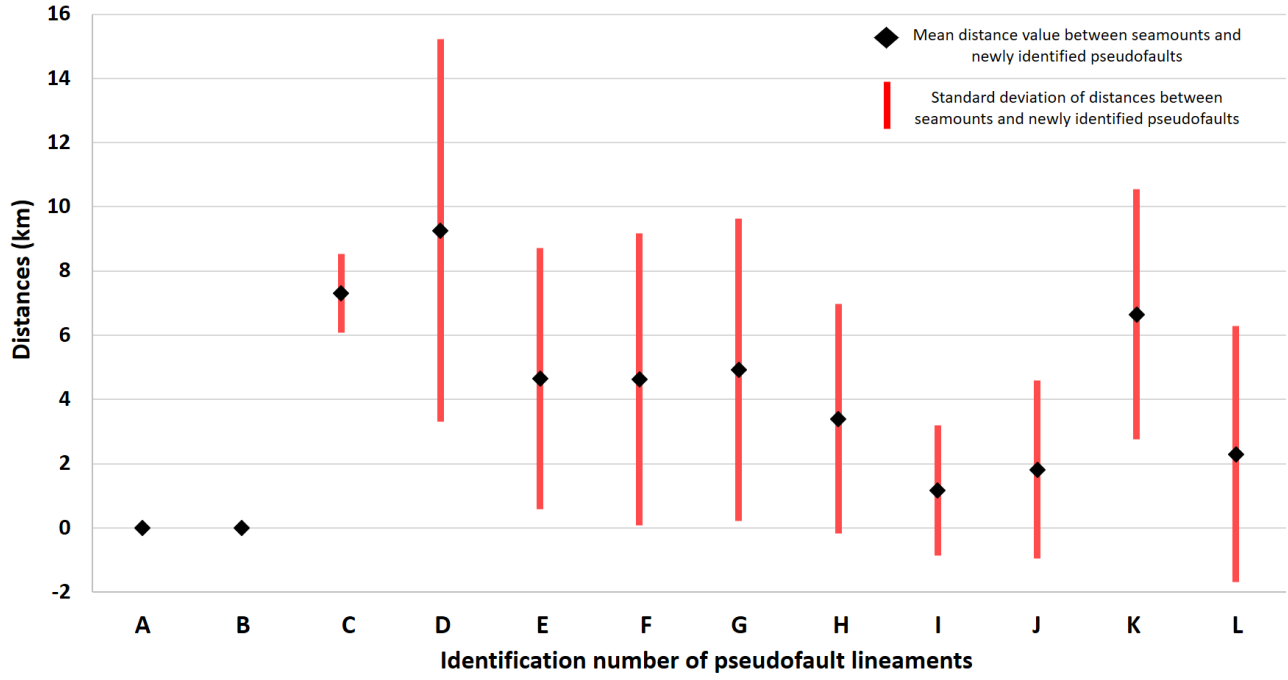

Figure 6.6: Graphs demonstrating a correlation between seamounts, propagator wakes and PSF lineaments. a) Frequency distribution of seamounts that are associated with each PSF lineament or propagator wake. b) Standard deviation for distances between seamounts and PSF lineaments

Table 6.3: Characterization of pseudofault lineaments

PSF related lineaments	corresponding lower density zone number with density value (d) in g/cc	Density value of adjacent block in west	Density value of adjacent block in east	Basement characteristics within the corresponded lower density zone	Amplitude of gravity low (mGal)	Distance from the previous pseudofault lineament in km	Number of associated seamounts within 15 km	Distance to associated seamounts within 15 km	
								Distance from lineament (km)	Average distance from lineament(km) & their standard deviation (km)
A	No corresponding lower density zone	N/A	N/A	Not accessed	N/A-	N/A	1	0	0.00 & 0.00
B	3 (d = 2.78)	2.8	2.8	No crustal thinning or thickening	2.4	48 - 64	2	0, 0	0.00 & 0.00
C	4 (d = 2.81)	2.84	2.85		3.0	35.5 - 95	7	9, 6, 7.5, 7, 8.2, 8.3, 5.3	7.31 & 1.23
D	5 (d = 2.84)	2.87	2.87		0.3	24 - 37.7	5	12, 4.6, 0, 15, 14.7	9.26 & 5.96
E	6 (d = 2.84)	2.88	2.88		5.3	17 - 26	6	0, 4.5, 6, 12, 0, 5.4	4.65 & 4.07

F	8 (d = 2.76)	2.80	2.80		3.0	25 - 44	11	0, 0, 0, 0, 0, 7.5, 12, 9.5, 10, 5, 7	4.63 & 4.55
G	9 (d = 2.77)	2.80	2.80	No crustal thinning or thickening	2.0	17 - 23	7	0, 5, 0, 8.5, 12.5, 0, 8.5	4.93 & 4.71
H	9 (d = 2.77)	2.80	2.80		5.0	32 - 38	8	10, 5.5, 0, 6, 0.4, 0, 5.3, 0	3.40 & 3.57
I	10 (d = 2.78)	2.81	2.82		3.0	48 - 78	7	0, 0, 0, 0, 0, 5.6, 2.6	1.17 & 2.02
J	No corresponding lower density zone	N/A	N/A		N/A	23 - 41	6	7.3, 0, 0, 0, 3.6, 0	1.82 & 2.78
K	11 (d = 2.80)	2.84	2.84		1.75	22 - 44	4	0, 8.4, 8.2, 10	6.65 & 3.90
L	No corresponding lower density zone	N/A	N/A	Not accessed	N/A	130 - 140	4	0, 9.2, 0, 0	2.30 & 3.98

Table 6.4: Characterization of previously interpreted propagator wakes

Propagator wake	corresponding lower density zone number with density value (d) in g/cc	Density value of adjacent block in west	Density value of adjacent block in east	Basement characteristics within the corresponded lower density zone	Amplitude of gravity low (mGal)	Number of associated seamounts that are entirely or partly within the propagator wake
i	Models do not cross the feature	N/A	N/A	N/A	N/A	2
ii	1 (d= 2.76)	2.8	2.83	No crustal thinning or thickening	8	5
	2 (d= 2.78)	2.83	2.8	Crustal thinning of 0.5 km in the middle of the zone	5.5	
iii	7 (d= 2.86)	2.89	2.89	Inadequate seismic data to discern any crustal architecture	11	14
	10 (d= 2.78)	2.81	2.82	Crustal thinning of 0.4 km in the middle of the zone	7	
iv	12 (d = 2.82)	2.88	2.88	Crustal thinning of 0.6 km in the middle of the zone	4	5

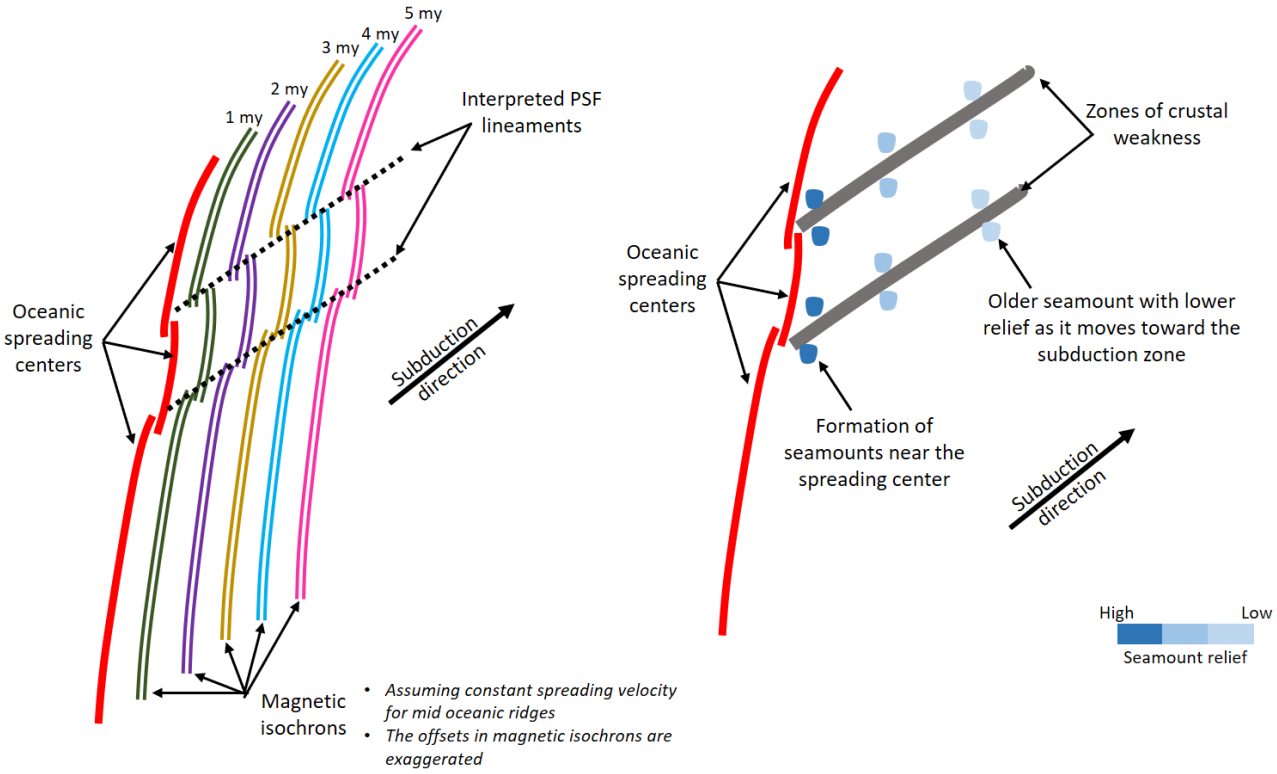

Figure 6.7: Hypothesis showing newly interpreted PSF lineaments are triggered from offsets between spreading ridge segments. Because they are zones of crustal weakness, magmas are using those as pathways which ultimately results in the formation of seamounts.

6.4 Possible effects of identified tectonic structures on subduction mechanism

As seen from the previous section, the interpreted pseudofault lineaments on the JdF plate represent zones of weakened crust. Similarly, the propagator wakes are also interpreted as zones of crustal weakness because of their modeled lower density, which is consistent with the established theory of rift propagation. Even within a continuous propagating rift system (such as the Broad Transform Zone Geometry illustrated in Fig. 2.2b), the propagator wakes should contain smaller scale extinct ridges and fossil transform faults that accommodate shear between propagating and failing rifts (Hey et

al., 1986; Hey, 2020). This indicates a higher amount of active or inactive faulting within the propagator wakes resulting in lower densities as illustrated in Fig. 6.8. When being subducted, this weakened crust is more susceptible to rupture, leading to a higher potential for generating earthquakes. However, to examine this correlation further, a comprehensive 3d modeling of the JdF crust is necessary, which is beyond the scope of this thesis.

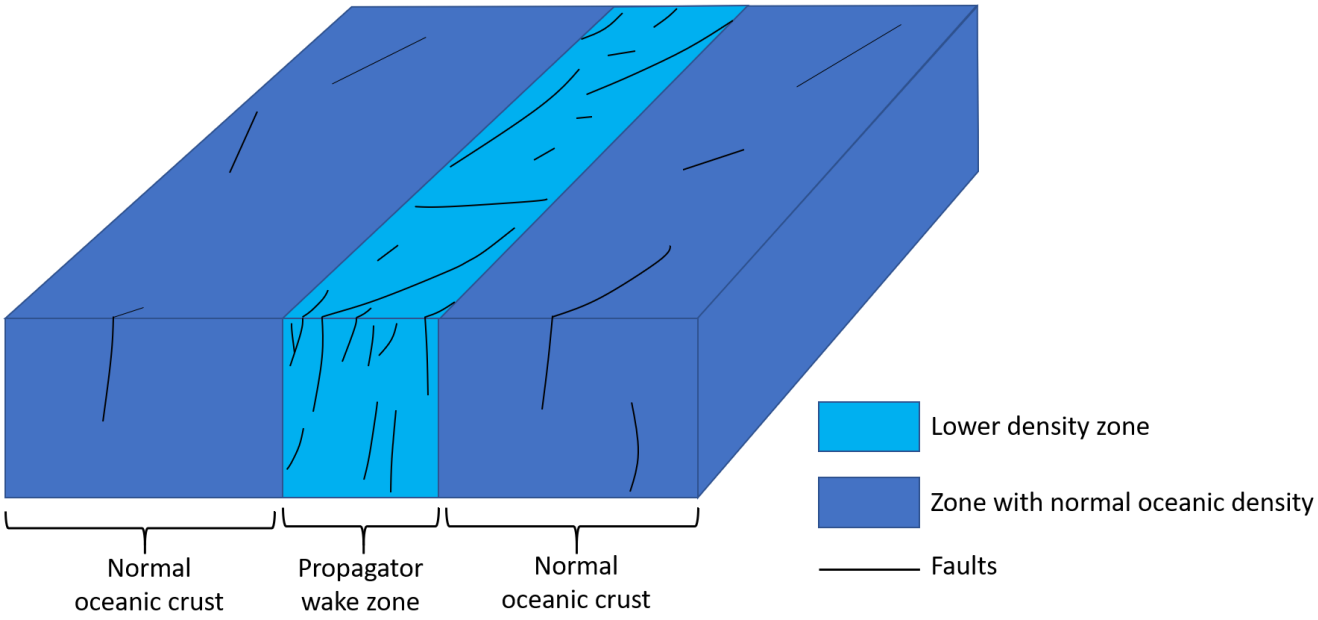

Figure 6.8: Diagram illustrating the higher amount of faults within the zone of propagator wake. This conclusion is consistent with the observation of lower density zones in propagator wakes and the current theoretical understanding of rift propagation.

If we project the positions of tectonic structures with weakened crust (i.e., propagator wakes and PSF lineaments) from the non-subducting part of the JdF plate to the subducting slab, most of these structures should end up beneath continental Washington. As a result, the concentration of subducting zones of crustal weakness

beneath Washington is much higher than in Oregon (Fig. 6.9). Since these weaker crusts are more susceptible to structural failures, they are probably contributing to the generation of a higher amount of seismicity under Washington.

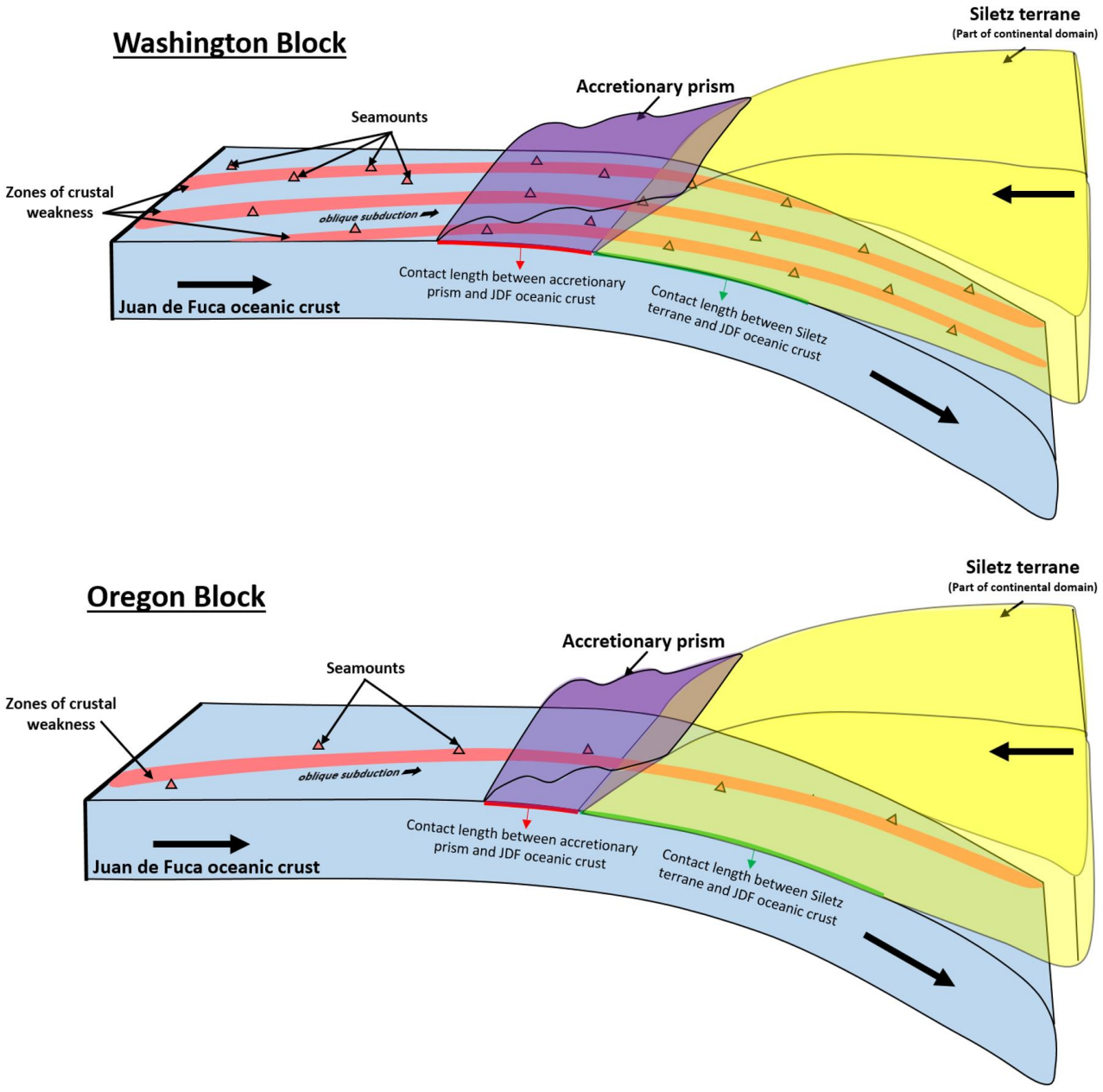

Figure 6.9: Block diagrams showing the lower density zones or weak crustal zones and the associated seamounts are subducting beneath Washington in a higher amount than Oregon.

In order to test this hypothesis, earthquakes from the Wadati-Benioff zone (see section 4.3.1 for the methodology of selecting these earthquakes) over the CSZ were analyzed. First, all of the earthquakes were divided into several clusters keeping the overall orientation of the clusters parallel to the subduction direction. Then least square best fit lines were calculated for each earthquake cluster (shown by pink lines in Fig. 6.10).

These best fit lines through the earthquakes are aligned with the projected direction of PSF lineaments and propagator wakes on the JdF plate (Fig. 6.10). This suggests that identified weak crustal zones (i.e., PSF lineaments and propagator wakes) may be responsible for the earthquakes that are occurring on the subducting JdF oceanic plate. Nonetheless, weak crustal zones of the subducting slab cannot solely cause earthquakes. To generate seismicity, the subducting oceanic crust must interact with another tectonic feature, which, in the case of the CSZ, is the Siletz terrane. Some research postulates that the Siletz terrane is accountable for most of the crustal seismicity—especially in the Washington region (Merrill et al., 2020).

In order to further investigate the relations of the propagator wakes and PSF lineaments as zones of crustal weakness with the observed seismicity, a three-dimensional gravity modeling of the JdF plate is required where a 3D seismic reflection or closely spaced several 2D reflection lines can be used as constraints. Also, 2D integrated models over the propagator wakes of the Pacific plate should be developed to verify the correlation between these structures and lower density crustal regions. Eventually, propagator wakes of other regions of the world have to be inspected with a similar routine as shown in this study. Moreover, comparing the offsets of seafloor magnetic strips with

the offset between spreading ridges (factoring in seafloor spreading velocity of these associated ridges) is necessary to further verify the proposed hypothesis in this study regarding PSF lineament formation.

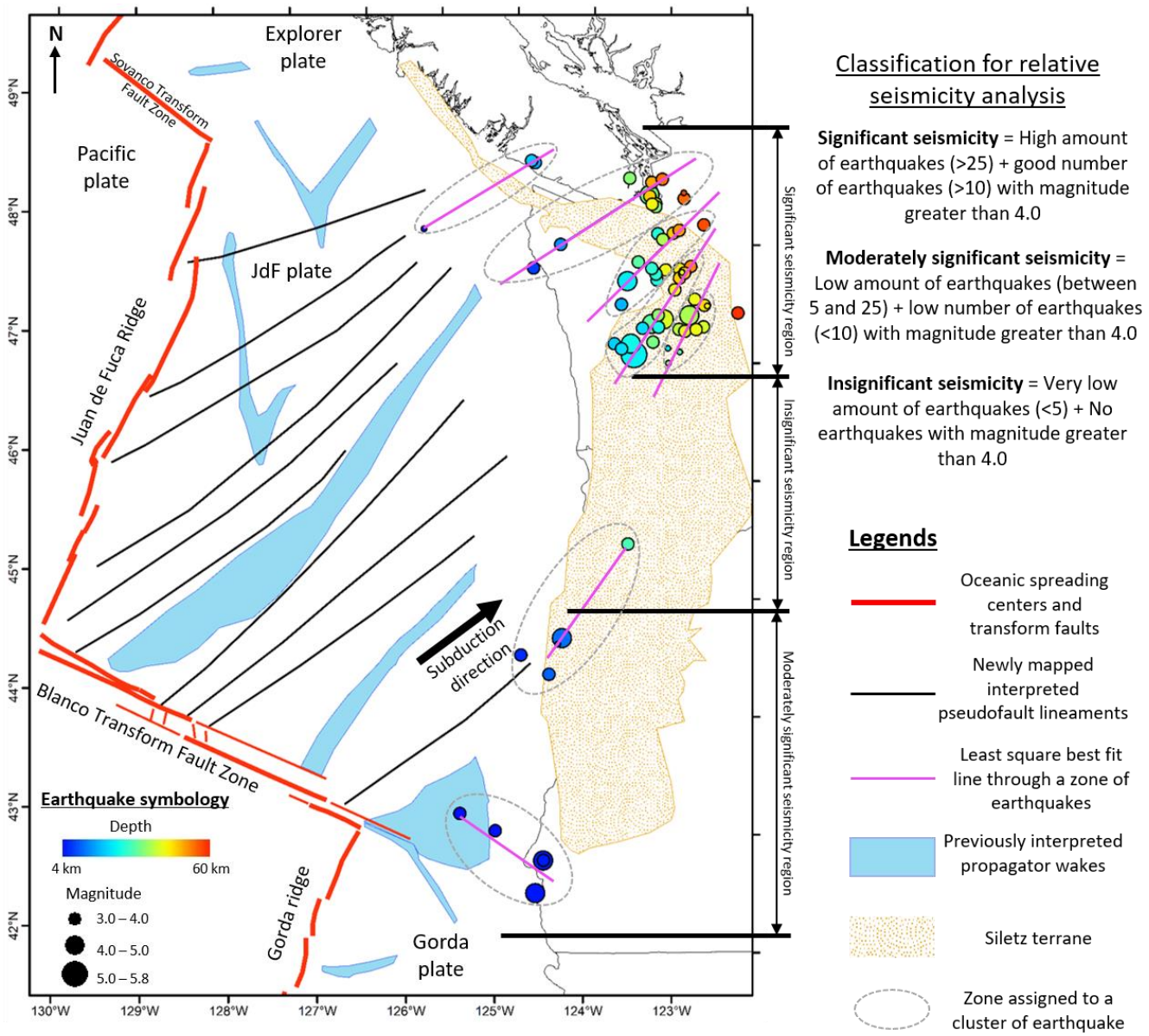

Figure 6.10: Diagram illustrating statistically derived lineaments through clusters of Wadati-Benioff zone earthquakes. Orientations of these lineaments are similar to the direction of subducting PSF lineaments and propagator wakes.

Chapter 7: Conclusions

The CSZ comprises complex geological structures that have intricate tectonic relationships with each other. These structures are seamounts, propagator wakes and newly identified PSF lineaments within the oceanic JdF plate. The complicated tectonic interactions between these structures that have been ignored in most of the previous studies, may be related to seismicity segmentation along the subduction zone. Following are the major conclusions of this study.

- ☐ The developed 2D regional integrated models revealed geological similarities and discrepancies between zones with different seismicity, outlining several potential drivers for the observed seismicity segmentation over the CSZ. Two 2D plate-scale integrated models through both seismicity regions result in more geologically valid physical properties of subsurface rocks over the CSZ. The derived densities agree better with the global average than all other found previous studies.

- ☐ 2D modeling revealed several lower density crustal zones within the JdF plate that correlate with established propagator wakes. This result contradicts the finding of 2D modeling by Marjanović et al. (2011) concluding that the propagator wakes correspond to higher density crustal blocks. To resolve this contention, two 2D gravity models have been developed along the same modeling lines of Marjanović et al. (2011) disproving the conclusion about the denser crust of the propagator wakes for two major reasons. The first one is the positive gravity effects of the nearby

seamounts that were not taken into account in 2D approximation resulting in an artificial increase in crustal density required to explain the observed gravity anomaly. The other one is not accounting for the normal increase in the density of oceanic crust as it moves away from the spreading center.

- The spatial analysis resulted in the mapping of key tectonic structures over the entire JdF plate from several geophysical datasets. Along with the already established propagator wakes, several NE-SW trending PSF lineaments have been identified in this study from filtered residual magnetic anomaly maps. In addition, several buried seamounts were located by isolating a characteristic gravity signature from known seamounts. Moreover, the seamounts appear to be clustered around propagator wakes and PSF lineaments.

- The observed spatial correlation between propagator wakes, PSF lineaments, and seamounts triggered the hypothesis about their tectonic relationships. The newly identified PSF lineaments are aligned with the subduction direction and appear to be triggered by offsets between different segments of the JdF spreading center. Their correlation with lower density zones also indicates that these PSF lineaments (and also the propagator wakes) represent zones of crustal weakness, favorable for the formation of seamounts. Moreover, because of the obliquity in the JdF plate's subduction, most of these weak crustal zones and seamounts are subducting beneath continental Washington. This may be a contributing factor behind higher

observed seismicity in Washington with respect to Oregon. This is further consistent with the linear pattern of the earthquakes from the Wadati-Benioff zone along the CSZ that appear to be aligned with the weak crustal zones of the JdF plate identified in this study. Several follow-up studies both on Pacific and JdF plates are proposed to investigate these structures further.

References

Atwater, B.F., 1987, Evidence for Great Holocene Earthquakes along the Outer Coast of Washington State, Science, New Series, v. 236, no. 4804, p. 942-944

Atwater, B.F. et al., 1995, Summary of Coastal Geologic Evidence for Past Great Earthquakes at the Cascadia Subduction Zone: Earthquake Spectra, v. 11, p. 1–18, doi:10.1193/1.1585800.

Atwater, B., 2005, The orphan tsunami of 1700: Japanese clues to a parent earthquake in North America:, doi:10.2112/1551-5036(2006)22[1015aa:totojc]2.0.co;2.

Atwater, B.F., and Hemphill-haley, E., 1996, Preliminary Estimates of Recurrence Intervals for Great Earthquakes Of the Past 3500 Years at Northeastern Willapa Bay, Washington: Geology, v. 5

Bankey, V. et al., 2002, Digital data grids for the magnetic anomaly map of North America, USGS Open-File Report 02-414.

Bilek, S.L., and Lay, T., 2018, Subduction zone megathrust earthquakes: Geosphere, doi:10.1130/GES01608.1.

Blakely, R.J., Brocher, T.M., and Wells, R.E., 2005, Subduction-zone magnetic anomalies and implications for hydrated forearc mantle: Geology, v. 33, p. 445–448, doi:10.1130/G21447.1.

Carbotte, S.M., Nedimović, M.R., Canales, J.P., Kent, G.M., Harding, A.J., and Marjanović,

M., 2008, Variable crustal structure along the Juan de Fuca Ridge: Influence of on-axis hot spots and absolute plate motions: Geochemistry, Geophysics, Geosystems, v. 9, doi:10.1029/2007GC001922.

Carlson, R.L., and Herrick, C.N., 1990, Densities and porosities in the oceanic crust and their variations with depth and age: Journal of Geophysical Research, v. 95, p. 9153–9170, doi:10.1029/JB095iB06p09153.

Chadwick, J., Perfit, M., Ridley, I., Jonasson, I., Kamenov, G., Chadwick, W., Embley, R., le Roux, P., and Smith, M., 2005, Magmatic effects of the Cobb hot spot on the Juan de Fuca Ridge: Journal of Geophysical Research: Solid Earth, v. 110, p. 1–16, doi:10.1029/2003JB002767.

Clague, J.J., 1997, Evidence for large earthquakes at the Cascadia subduction zone: Reviews of Geophysics, doi:10.1029/97RG00222.

Crenna, P.A., Yeats, R.S., and Levi, Shaul, 1994, Late Cenozoic tectonics and paleogeography of the Salem Metropolitan area, central Willamette Valley, Oregon: Oregon Geology, v. 56, p. 129–136.

Davis, E.E., and Hyndman, R.D., 1989, Accretion and recent deformation of sediments along the northern Cascadia subduction zone: Geological Society of America Bulletin, v. 101, p. 1465–1480, doi:10.1130/0016-7606(1989)101<1465:AARDOS>2.3.CO;2.

Desonie, D. L., and Duncan, R. A., 1990, The Cobb-Eickelberg Seamount Chain: Hotspot

volcanism with mid-ocean ridge basalt affinity: Journal of Geophysical Research: Solid Earth, 95(B8), p. 12697-12711, doi: 10.1029/JB095ib08P12697

DeMets, C., Gordon, R.G., and Argus, D.F., 2010, Geologically current plate motions: Geophysical Journal International, doi:10.1111/j.1365-246X.2009.04491.x.

DeMets, C., Gordon, R.G., Argus, D.F., and Stein, S., 1990, Current plate motions: Geophysical Journal International, doi:10.1111/j.1365-246X.1990.tb06579.x.

Duncan, R. A., 1982. A captured island chain in the coast range of Oregon and Washington: Journal of Geophysical Research., 87, p. 10827-10837.

Elvers, D., Srivastava, S. P., Potter, K., Morley, J., and Seidel, D., 1973, Asymmetric spreading across the Juan de Fuca and Gorda Rises as obtained from a detailed magnetic survey: Earth Planetary Science Letters, v. 20, p. 211-219.

Gao, H., Humphreys, E. D., Yao, H., and van der Hilst, R. D., 2011. Crust and lithosphere structure of the northwestern US with ambient noise tomography: Terrane accretion and Cascade arc development: Earth and Planetary Science Letters, 304, no. 1, p. 202-211.

Gee, J., and Kent, D. V., 1998, Magnetic telechemistry and magmatic segmentation on the Southern East Pacific Rise: Earth and Planetary Science Letters, v. 164, p. 379–385, doi:10.1016/S0012-821X(98)00231-3.

Gannett M.W., and Caldwell, R.C., 1998, Geologic framework of the Willamette lowland

aquifer system, Oregon and Washington: U.S. Geological Survey Professional Paper 1424–A, 32 p.

Goldfinger, C. et al., 2012, Turbidite Event History—Methods and Implications for Holocene Paleoseismicity of the Cascadia Subduction Zone: U.S. Geological Survey Professional Paper 1661-F: Earthquake Hazards of the Pacific Northwest Coastal and Marine Regions, p. 170.

Goldfinger, C., Galer, S., Beeson, J., Hamilton, T., Black, B., Romsos, C., Patton, J., Nelson, C.H., Hausmann, R., and Morey, A., 2017, The importance of site selection, sediment supply, and hydrodynamics: A case study of submarine paleoseismology on the northern Cascadia margin, Washington USA: Marine Geology, doi:10.1016/j.margeo.2016.06.008.

Haeussler, P., Clark, J., and Kenneth, P., 2000. Geologic map of the Wildcat Lake 7.5' Quadrangle Kitsap and Mason counties, Washington.

Han, S., Bangs, N.L., Carbotte, S.M., Saffer, D.M., and Gibson, J.C., 2017, Links between sediment consolidation and Cascadia megathrust slip behaviour: Nature Geoscience, v. 10, p. 954–959, doi:10.1038/s41561-017-0007-2.

Han, S., Carbotte, S.M., Canales, J.P., Nedimovic, M.R., Carton, H., Gibson, J.C., and Horning, G.W., 2016, Seismic reflection imaging of the Juan de Fuca plate from ridge to trench: New constraints on the distribution of faulting and evolution of the crust prior to subduction: Journal of Geophysical Research: Solid Earth, doi:10.1002/2015JB012416.

Harper, H., Tozer, B., Sandwell, D.T., and Hey, R.N., 2021, Marine Vertical Gravity Gradients Reveal the Global Distribution and Tectonic Significance of “Seesaw” Ridge Propagation: Journal of Geophysical Research: Solid Earth, v. 126, doi:10.1029/2020JB020017.

Hasselgren, E., Clowes, R.M. and Calvert, A.J., 1992, Propagating rift pseudofaults-Zones of crustal underplating imaged by multichannel seismic reflection data: Geophysical research letters, v. 19(5), p. 485-488.

Heaton, T.H., and Hartzell, S.H., 1987, Earthquake hazards on the Cascadia subduction zone: Science, doi:10.1126/science.236.4798.162.

Hey, R., 1977a, A new class of “pseudofaults” and their bearing on plate tectonics: A propagating rift model: Earth and Planetary Science Letters, v. 37, p. 321–325, doi:10.1016/0012-821X(77)90177-7.

Hey, R., 1977b, A new class of “pseudofaults” and their bearing on plate tectonics: A propagating rift model: Earth and Planetary Science Letters, doi:10.1016/0012-821X(77)90177-7.

Hey, R., 2020, Propagating Rifts and Microplates at Mid-Ocean Ridges: Elsevier Inc., 1–12 p., doi:10.1016/b978-0-12-409548-9.03027-x.

Hey, R.N., Kleinrock, M.C., Miller, S.P., Atwater, T.M., and Searle, R.C., 1986, Sea Beam/Deep-Tow Investigation of an active oceanic propagating rift system, Galapagos 95.5°W: Journal of Geophysical Research: Solid Earth,

doi:10.1029/jb091ib03p03369.

Hirsch, D. M., and Babcock, R. S., 2009. Spatially heterogeneous burial and high-P/T metamorphism in the Crescent Formation, Olympic Peninsula, Washington: American Mineralogist, 94, no. 8-9, p. 1103-1110.

Hyndman, R.D., 1988, Dipping seismic reflectors, electrically conductive zones, and trapped water in the crust over a subducting plate: Journal of Geophysical Research, v. 93, doi:10.1029/jb093ib11p13391.

Hyndman, R., Yorath, C., Clowes, R., and Davis, E., 1990. The northern Cascadia subduction zone at Vancouver Island: Seismic structure and tectonic history: Canadian Journal of Earth Sciences, 27, no. 3, p. 313-329.

Johnson, H.P. and Embley, R.W., 1990, Axial Seamount: An active ridge axis volcano on the central Juan de Fuca Ridge: Journal of Geophysical Research, Vol. 95, No. B8, p. 12689-12696, doi:0148-0227/90/90JB-01037502.00

Johnson, H.P., Karsten, J.L., Delaney, J.R., Davis, E.E., Currie, R.G. and Chase, R.L., 1983, A detailed study of the Cobb offset of the Juan de Fuca Ridge: Evolution of a propagating rift: *Journal of Geophysical Research: Solid Earth*, *88*(B3), pp.2297-2315, doi:10.1029/JB088iB03p02297

Karsten, J.L., and Delaney, J.R., 1989, Hot spot-ridge crest convergence in the northeast Pacific: Journal of Geophysical Research, doi:10.1029/JB094iB01p00700.

Kleinrock, M.C., Tucholke, B.E., Lin, J., and Tivey, M.A., 1997, Fast rift propagation at a slow-spreading ridge: Geology, doi:10.1130/0091-

7613(1997)025<0639:FRPAAS>2.3.CO;2.

Kopp, H., 2013, Invited review paper: The control of subduction zone structural complexity and geometry on margin segmentation and seismicity: Tectonophysics, doi:10.1016/j.tecto.2012.12.037.

Lewis, T.J., Bentkowski, W.H., Davis, E.E., Hyndman, R.D., Souther, J.G., and Wright, J.A., 1988, Subduction of the Juan de Fuca plate: thermal consequences: Journal of Geophysical Research, v. 93, p. 207–225, doi:10.1029/jb093ib12p15207.

Ludwin, R.S., Dennis, R., Carver, D., McMillan, A.D., Losey, R., Clague, J., Jonientz-Trisler, C., Bowechop, J., Wray, J., and James, K., 2005, Dating the 1700 Cascadia earthquake: Great coastal earthquakes in native stories: Seismological Research Letters, doi:10.1785/gssrl.76.2.140.

Marjanović, M., Carbotte, S.M., Nedimovi, M.R., and Canales, J.P., 2011, Gravity and seismic study of crustal structure along the Juan de Fuca Ridge axis and across pseudofaults on the ridge flanks: Geochemistry, Geophysics, Geosystems, doi:10.1029/2010GC003439.

Mason, R. G., 1958, A magnetic survey off the west coast of the United States between latitudes 32 ° and 26°N and longitudes 121 ° and 128°W: Geophysics Journal p. 320-329.

Mason, R. G., and Raff, A. D., 1961, Magnetic survey off the west coast of North America, 32°N latitude to 42°N latitude, Geological Society of America Bulletin, v. 72, p. 1259-1266.

Massey, N. W. D., 1986. Metchosin Igneous Complex, southern Vancouver Island - ophiolite stratigraphy developed in an emergent island setting: Geology, 14, no. 7, p. 602-605.

McCrory, P.A., Blair, J.L., Waldhauser, F., and Oppenheimer, D.H., 2012, Juan de Fuca slab geometry and its relation to Wadati-Benioff zone seismicity: Journal of Geophysical Research: Solid Earth, v. 117, p. 1–23, doi:10.1029/2012JB009407.

McCrory, P. A., and Wilson, D. S., 2013. A kinematic model for the formation of the Siletz-Crescent forearc terrane by capture of coherent fragments of the Farallon and Resurrection plates: Tectonics, 32, no. 3, p. 718-736.

Merrill, R., Bostock, M.G., Peacock, S.M., Calvert, A.J., and Christensen, N.I., 2020, A Double Difference Tomography Study of the Washington Forearc: Does Siletzia Control Crustal Seismicity? Journal of Geophysical Research: Solid Earth, v. 125, p. 1–18, doi:10.1029/2020JB019750.

Miller, M.M., Melbourne, T., Johnson, D.J., and Sumner, W.Q., 2002, Periodic slow earthquakes from the Cascadia subduction zone: Science, v. 295, p. 2423, doi:10.1126/science.1071193.

Müller, R.D., Sdrolias, M., Gaina, C., and Roest, W.R., 2008, Age, spreading rates, and spreading asymmetry of the world's ocean crust: Geochemistry, Geophysics,

Geosystems, v. 9, p. 1–19, doi:10.1029/2007GC001743.

Nedimović, M.R., Bohnenstiehl, D.W.R., Carbotte, S.M., Pablo Canales, J., and Dziak, R.P., 2009, Faulting and hydration of the Juan de Fuca plate system: Earth and Planetary Science Letters, v. 284, p. 94–102, doi:10.1016/j.epsl.2009.04.013.

Nedimović, M.R., Carbotte, S.M., Harding, A.J., Detrick, R.S., Canales, J.P., Diebold, J.B., Kent, G.M., Tischer, M., and Babcock, J.M., 2005, Frozen magma lenses below the oceanic crust: Nature, v. 436, p. 1149–1152, doi:10.1038/nature03944.

Nedimović, M.R., Hyndman, R.D., Ramachandran, K., and Spence, G.D., 2003, Reflection signature of seismic and aseismic slip on the northern Cascadia subduction interface: Nature, doi:10.1038/nature01840.

Parsons, T. et al., 2006, Crustal Structure of Cascadia Fore Arc of Washington: Earthquake Hazards of the Pacific Northwest Coastal and Marine Regions / Robert Kayen, ed. ; Bd. D = Professional Paper / U.S. Geological Survey, 1661-D . US Geological Survey Information Services, Denver, Colorado, USA, 40 pp.,.

Parsons, T., Trehu, A.M., Luetgert, J.H., Miller, K., Kilbride, F., Wells, R.E., Fisher, M.A., Flueh, E., Ten Brink, U.S., and Christensen, N.I., 1998, A new view into the Cascadia subduction zone and volcanic arc: Implications for earthquake hazards along the Washington margin: Geology, v. 26, p. 199–202, doi:10.1130/0091-7613(1998)026<0199:ANVITC>2.3.CO;2.

Parsons, T., Wells, R.E., Fisher, M.A., Flueh, E., and Ten Brink, U.S., 1999, Three-

dimensional velocity structure of Siletzia and other accreted terranes in the Cascadia forearc of Washington: Journal of Geophysical Research: Solid Earth, v. 104, p. 18015–18039, doi:10.1029/1999jb900106.

Phillips, B.A., Kerr, A.C., Mullen, E.K., and Weis, D., 2017, Oceanic mafic magmatism in the Siletz terrane, NW North America: Fragments of an Eocene oceanic plateau? Lithos, v. 274–275, p. 291–303, doi:10.1016/j.lithos.2017.01.005.

Raft, A. D., and Mason, R. G., 1961, Magnetic survey off the west coast of North America, 40°N latitude to 52°N latitude: Geological Society of America Bulletin, v. 72 p. 1267-1270.

Romanyuk, T. V., Blakely, R., and Mooney, W.D., 1998, The Cascadia Subduction Zone: two contrasting models of lithospheric structure: Physics and Chemistry of the Earth, v. 23, p. 297–301, doi:10.1016/S0079-1946(98)00028-7.

Sandwell, D.T., Müller, R.D., Smith, W.H.F., Garcia, E., and Francis, R., 2014, New global marine gravity model from CryoSat-2 and Jason-1 reveals buried tectonic structure: Science, doi:10.1126/science.1258213.

Satake, K., Shimazaki, K., Tsuji, Y., and Ueda, K., 1996, Time and size of a giant earthquake in Cascadia inferred from Japanese tsunami records of January 1700: Nature, v. 379, p. 246–249, doi:10.1038/379246a0.

Schmalzle, G.M., McCaffrey, R., and Creager, K.C., 2014, Central Cascadia subduction zone creep: Geochemistry, Geophysics, Geosystems, v. 15, p. 1515–1532, doi:10.1002/2013GC005172.

Sherrod, D. R., and Pickthorn, L. G., 1989, Some notes on the Neogene structural evolution of the Cascade Range in Oregon, in, Muffler, L.J.P., Weaver, C.S., and Blackwell, D.D., Geological, geophysical, and tectonic setting of the Cascade Range: U.S. Geological Survey Open-File Report 89–178, p. 351–368.

Silver, E. A., 1971, Small plate tectonics in the northeastern Pacific: Geological Society of America Bulletin, v. 82, p. 3491-3496.

Smith, W.H.F., and Sandwell, D.T., 1997, Global sea floor topography from satellite altimetry and ship depth soundings: Science, doi:10.1126/science.277.5334.1956.

Snavely, P. D., MacLeod, N. S., and Wagner, H. C., 1968. Tholeiitic and alkalic basalts of the Eocene Siletz River volcanics, Oregon coast range: American Journal of Science, 266, no. 6, p. 454-481.

Sreejith, K.M., Chaubey, A.K., Mishra, A., Kumar, S., and Rajawat, A.S., 2016, Pseudofaults and associated seamounts in the conjugate Arabian and Eastern Somali basins, NW Indian Ocean – New constraints from high-resolution satellite-derived gravity data: Journal of Asian Earth Sciences, v. 131, p. 1–11, doi:10.1016/j.jseaes.2016.09.002.

Telford, W.M., Geldart, L.P., and Sheriff, R.E., 1990, Applied geophysics. 2nd edition: Applied geophysics. 2nd edition,.

Trehu, A.M., Asudeh, I., Brocher, T.M., Luetgert, J.H., Mooney, W.D., Nabelek, J.L., and Nakamura, Y., 1994, Crustal architecture of the cascadia forearc: Science, v. 266, p. 237–243, doi:10.1126/science.266.5183.237.

Tréhu, A.M., Blakely, R.J., and Williams, M.C., 2012, Subducted seamounts and recent earthquakes beneath the central cascadia forearc: Geology, doi:10.1130/G32460.1.

Vine, F. J., 1968, Magnetic anomalies associated with mid-ocean ridges, in: The History of the Earth's Crust, R.A. Phinney, ed., p. 73-89.

Wang, K., and Tréhu, A.M., 2016, Invited review paper: Some outstanding issues in the study of great megathrust earthquakes—The Cascadia example: Journal of Geodynamics, v. 98, p. 1–18, doi:10.1016/j.jog.2016.03.010.

Wells, R.E., 1998, Fore-arc migration in Cascadia and its neotectonic significance: Geology, doi:10.1130/0091-7613(1998)026<0759:FAMICA>2.3.CO;2.

Wells, R. E., and Sawlan, M. G., 2014. Preliminary geologic map of the eastern Willapa Hills, Cowlitz, Lewis, and Wahkiakum Counties, Washington: US Geological Survey, 2331-1258.

Wessel, P., and Kroenke, L.W., 1998, The geometric relationship between hot spots and seamounts: implications for Pacific hot spots: Earth and Planetary Science Letters, v. 158, p. 1–18, doi:10.1016/S0012-821X(98)00043-0.

Wheat, C.G., Jannasch, H.W., Kastner, M., Plant, J.N., DeCarlo, E.H., and Lebon, G., 2004, Venting formation fluids from deep-sea boreholes in a ridge flank setting: ODP Sites

1025 and 1026: Geochemistry, Geophysics, Geosystems, v. 5, doi:10.1029/2004GC000710.

Wilson, D.S., 1993, Confidence intervals for motion and deformation of the Juan de Fuca Plate: Journal of Geophysical Research, v. 98, doi:10.1029/93jb01227.

Wilson, S., 1988, Tectonic History of the Juan de Fuca Ridge ii ’ i ’ ’ ii ’ ii i [i ’ lililiiii ’ l i ’ ia , iilliili ’ li iil ii: v. 93.

Wilson, D.S., Hey, R.N., and Nishimura, C., 1984, Propagation as a mechanism of reorientation of the Juan de Fuca ridge.: Journal of Geophysical Research, v. 89, p. 9215–9225, doi:10.1029/JB089iB11p09215.

Wilson, D.S. and Kirby, S., 2002, The Juan de Fuca plate and slab: Isochron structure and Cenozoic plate motions: The Cascadia subduction zone and related subduction systems, 4350, p. 9-12

Witter, R.C., Zhang, Y., Wang, K., Goldfinger, C., Priest, G.R., and Allan, J.C., 2012, Coseismic slip on the southern Cascadia megathrust implied by tsunami deposits in an Oregon lake and earthquake-triggered marine turbidites: Journal of Geophysical Research: Solid Earth, doi:10.1029/2012JB009404.

Yeats, R.S., Graven, E.P., Werner, K.S., Goldfinger, Chris, and Popowski, T.S., 1996, Tectonics of the Willamette Valley, Oregon, in Rogers, A.M. and others, eds., Assessing earthquake hazards and reducing risk in the Pacific Northwest—Volume 1: U.S. Geological Survey Professional Paper 1560, p. 183–222.

Appendix-A

Table of earthquakes occurred within the Wadati-Benioff zone.

Latitude	Longitude	Depth (km)	Magnitude	Horizontal location error	Depth error	Magnitude error	Filtering status
48.707	-124.788	34.9	3.1	0	0	0	Accepted
48.69	-124.74	32	3.9	0	0	0	Accepted
48.57	-123.53	44	3.3	0	0	0	Accepted
48.563	-123.115	51.711	3.63	0.4	0.58	0.177	Accepted
48.5365	-123.248167	48.794	3.7	1.825	2.5	0.05	Accepted
48.446833	-122.840333	56.933	3	0.595	0.67	0.04	Accepted
48.428333	-123.277	43.751	4.1	3.283	3.06	0.06	Accepted
48.418167	-123.272667	47.415	3.5	0.022	0.01	0.05	Accepted
48.397667	-122.836833	52.16	3.45	0.43	0.88	0.142	Accepted
48.354667	-123.195333	45.453	3.6	0.893	1.05	0.04	Accepted
48.350333	-123.243667	45.874	3.1	0.707	1.19	0.04	Accepted
48.329833	-123.196833	43.728	3.37	0.32	0.53	0.14	Accepted
48.175	-122.587667	54.195	3.4	0.949	2.18	0.08	Accepted
48.129167	-122.900167	49.608	3.8	0.679	1.06	0.07	Accepted
48.106333	-122.974333	47.683	4	1.188	2.05	0.06	Accepted
48.100333	-123.169333	40.71	3.35	0.32	0.49	0.148	Accepted
48.1	-126.128	10	3	0	0	0	Accepted
48.052	-123.107833	44.3	3.03	0.33	0.63	0.194725	Accepted
48.0025	-124.396167	29.664	3.1	1.827	1.82	0.07	Accepted
47.860167	-123.415333	42.534	3.9	1.109	0.89	0.07	Accepted
47.823333	-122.755	50.027	3.7	0.827	1.03	0.06	Accepted
47.806167	-123.244667	41.084	3.1	0.843	1.38	0.07	Accepted
47.803333	-122.898167	46.305	3.7	0.747	1.14	0.07	Accepted
47.797167	-124.731667	23.057	3.04	1.26	1.6	0.146	Accepted
47.793833	-123.071667	45.775	3.7	0.595	0.97	0.06	Accepted
47.773833	-122.8645	45.275	3	0.419	0.81	0.09	Accepted
47.7675	-122.833833	48.11	3.1	1.125	1.74	0.07	Accepted
47.758833	-123.193	40.802	3.23	0.5	0.79	0.18	Accepted
47.725667	-122.896667	47.317	3.1	0.841	1.15	0.07	Accepted
47.707833	-123.178167	40.554	3.85	0.32	0.45	0.182	Accepted
47.698	-123.551667	39.32	4.07	0.35	0.38	0.174372	Accepted
47.6245	-122.955833	45.755	3.2	0.975	1.64	0.07	Accepted
47.545	-122.707167	45.615	3.3	0.906	1.74	0.07	Accepted
47.499667	-123.623833	33.49	3.42	0.37	0.77	0.182598	Accepted
47.492667	-122.586	46.683	3.7	0.807	1.34	0.05	Accepted

47.487333	-122.55	46.057	3	0.46	0.81	0.08	Accepted
47.425667	-122.168667	59.618	3.28	1.8	1.33	0.241	Accepted
47.409833	-123.162833	44.034	4	0.785	1.98	0.03	Accepted
47.409667	-122.775833	44.251	4.4	0.751	1.09	0.03	Accepted
47.375	-123.0935	45.264	4.5	1.295	2.17	0.07	Accepted
47.336833	-123.2425	42.7	4.3	0.934	1.32	0.03	Accepted
47.310833	-122.600167	45.217	3.6	0.7	1.19	0.06	Accepted
47.307667	-123.158667	40.28	3.4	0.768	0.54	0.09	Accepted
47.299667	-123.359	36.707	3.8	1.091	2	0.05	Accepted
47.290833	-122.905167	44.53	3.3	1.112	1.78	0.08	Accepted
47.288	-122.690667	45.616	3.1	0.468	0.84	0.04	Accepted
47.273667	-122.8315	45.61	3.2	0.651	1.23	0.04	Accepted
47.182	-123.227833	43.556	3.4	0.318	0.44	0.02	Accepted
47.1675	-123.5025	40.245	5	0.489	0.39	0.03	Accepted
47.166833	-123.708333	35.24	3.5	0.32	0.66	0.144	Accepted
47.129167	-123.042167	39.067	3	1.784	0.89	0.07	Accepted
47.123333	-123.6175	38.025	3.4	0.05	0.05	0.02	Accepted
47.098	-122.8945	43.043	3	1.165	2.06	0.06	Accepted
47.074	-123.463667	40.014	5.8	0.085	0.06	0.05	Accepted
47.003167	-123.0355	44.014	3	0.582	0.97	0.05	Accepted
45.468833	-123.521833	42.133	3.14	1.3	1.35	0.351	Accepted
44.6645	-124.300333	27.274	4.7	1.284	0.75	0.04	Accepted
44.613	-124.3475	25.41	3	0.41	0.53	0.242	Accepted
44.5155	-124.782167	21.037	3.6	1.804	1.29	0.07	Accepted
44.355833	-124.4455	25.76	3.12	1.29	0.75	0.1	Accepted
43.159	-125.449	10	3.2	0	0	0	Accepted
43.020833	-125.035	9.954	3.13	10.24	31.61	0.21	Accepted
42.7775	-124.4725	16.13	3.54	0.39	0.85	0.150742	Accepted
42.776	-124.476667	16.65	4.53	0.4	0.79	0.12488	Accepted
42.498	-124.56	15	4.5	0	0	0	Accepted
45.931333	-126.057667	4.54	3.03	99	31.61	0.336	Rejected

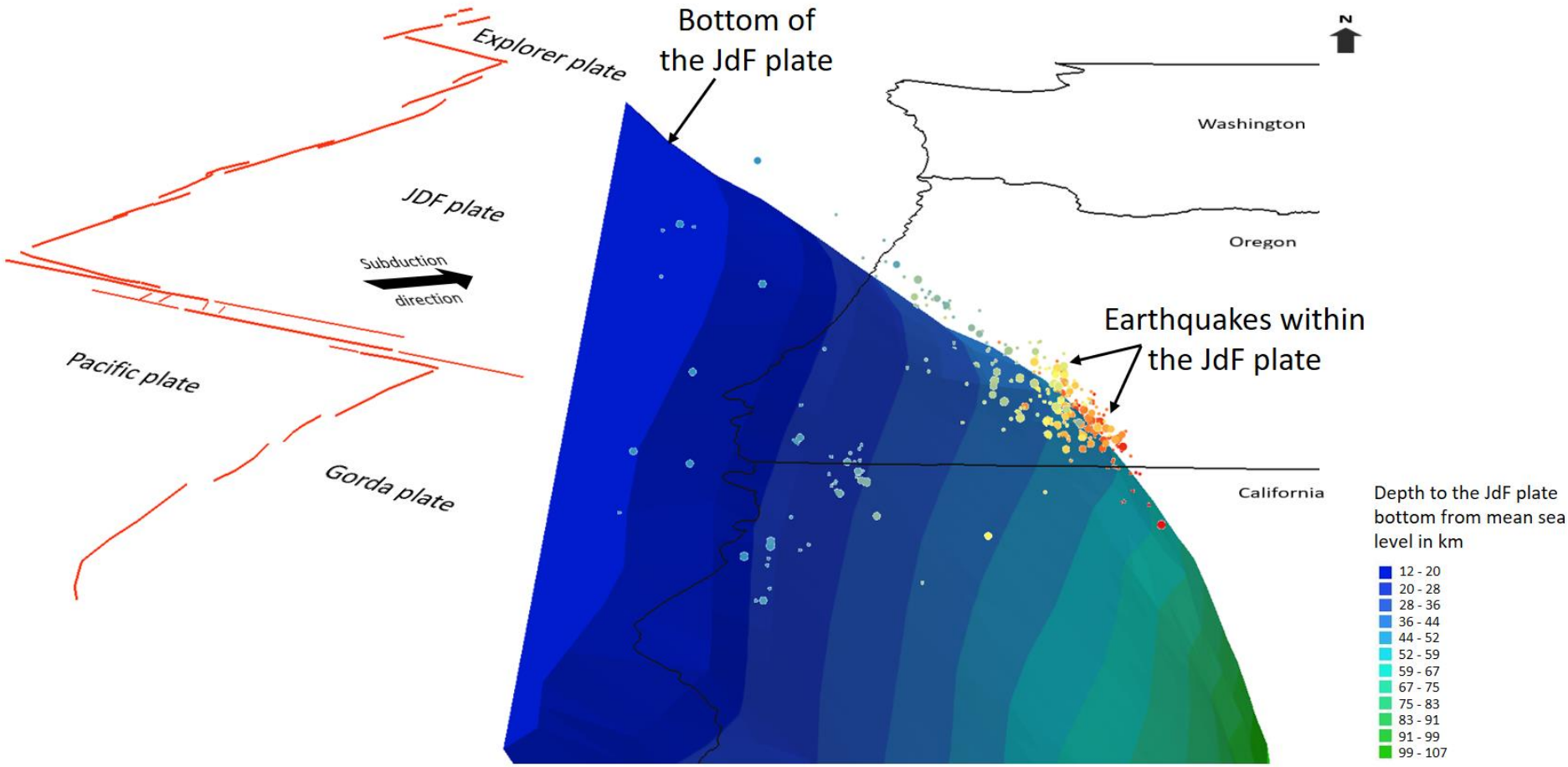

Figure illustrates earthquake selection process in a 3D environment of ArcGIS to isolate seismicity within the subduction oceanic crust.